Measuring the 7Li(a ; g)11B reaction rate at temperatures relevant for the n-process

Gwenaelle Gilardy

université de BORDEAUX

Thesis submitted in partial fulfillment for the
degree of Doctor of Philosophy of
The University of Bordeaux

Graduate School of Physical Sciences and Engineering
Specialty Nuclear Physics

Measuring the $^{7}Li(\alpha,\gamma)^{11}B$ reaction rate at temperatures relevant for the ν-process

by

Gwenaëlle Gilardy

under the supervision of Bertram BLANK

Defended on: December 18^{th} 2018

Committee members:

M. **TSEKANOVICH** Igor	Professeur CENBG	**Chair**
Mme. **HAMMACHE** Fairouz	Chargé de recherche IPN Orsay	**Rapporteure**
M. **COC** Alain	Directeur de recherche CSNSM Orsay	**Rapporteur**
M. **COUDER** Manoël	Assistant professeur Notre Dame	**Examinateur**
M. **BLANK** Bertram	Directeur de recherche CENBG	**Directeur**

Titre : Mesure du taux de réaction de $^{7}Li(\alpha,\gamma)^{11}B$ aux températures pertinentes pour le ν-process

Résumé Le ν-process semble être à l'origine d'une partie de la présence du ^{11}B dans l'univers. Ce processus, qui a lieu dans les supernovae dont le cœur s'effondre à des températures entre 1 GK et 5 GK, est la conséquence de l'effondrement du cœur d'une étoile. La chaîne de réaction principalement responsable de la production du ^{11}B se termine par la réaction $^{7}Li(\alpha,\gamma)^{11}B$. Cette réaction a seulement été mesurée par Paul et al. [1] aux énergies correspondantes aux températures mentionnées. Néanmoins, cette mesure a souffert du bruit de fond empêchant la détection de rayons gamma autre que ceux dus à la transition entre la capture directe et l'état fondamental du ^{11}B et ce, via une résonance ou non. Dans ce travail, nous nous sommes penchés à nouveau sur cette réaction. Notre objectif était de fournir une mesure additionnelle de cette section efficace avec la possibilité de détecter des cascades de rayons gamma ainsi que de mettre à jour le taux de réaction. Nous avons mesuré les rayons gamma provenant de la réaction $^{7}Li(\alpha,\gamma)^{11}B$ entre E_{cm}= 1 MeV et E_{cm}= 1.8 MeV en utilisant l'accélérateur Sta. Ana à l'université Notre Dame pour produire un faisceau d'hélium, envoyé ensuite sur une cible de LiOH. Les rayons gamma produits par cette réaction ont été perçus avec un détecteur germanium orienté à 45°. La section efficace différentielle obtenue a été analysées à l'aide de la théprie de la matrice **R** et du logiciel *Azure*. Nous avons décelé des incohérences entre les différentes mesures de la réaction $^{7}Li(\alpha,\gamma)^{11}B$. Deux taux de réaction ont été calculés séparément : l'un consisdérant la mesure que nous avons réalisée à 45° ; la seconde en utilisant la mesure de Paul et al. [1]. Ces deux taux de réaction sont différents des taux de réaction calculés précédemment et recommandés par NACRE [2] et NACRE II [3].

Mots clés: Supernovae à effondrement de cœur, ^{11}B, ν-process, section efficace, $^{7}Li(\alpha,\gamma)^{11}B$

Title : Measuring the $^{7}Li(\alpha,\gamma)^{11}B$ reaction rate at temperatures relevant for the ν-process

Abstract Part of the universal abundance of ^{11}B is believed to come from the ν-process which takes place in core collapse supernovae at temperature between 1 GK and 5 GK. The main reaction chain responsible for the production of ^{11}B is ending with the reaction $^{7}Li(\alpha,\gamma)^{11}B$. At the energies corresponding to the temperature range above, this reaction has only been measured by Paul et al. [1]. Their measurement was suffering from background preventing the detection of any transition other than the transition corresponding to the direct capture of alpha, via resonance or not, to the ground state of ^{11}B. Our goal was to provide an additional measurement with the possibility to observe a γ cascade and to update the stellar reaction rate accordingly. We measured γ-rays coming from the $^{7}Li(\alpha,\gamma)^{11}B$ reaction between E_{cm} = 1.0 MeV and E_{cm} = 1.8 MeV using the Sta. Ana accelerator at the University of Notre Dame to produce the helium beam that was sent on a LiOH target. The γ-rays were detected with a germanium detector at 45°. An R-matrix analysis of the differential cross section obtained was performed using the software *Azure*. We found inconsistencies between the different measurements of the $^{7}Li + \alpha$ reaction. Two reaction rates were calculated using the measurement at 45° and the measurement of Paul et al. [1]. These two reaction rates are increased compared to the previous reaction rate recommended by NACRE [2] and NACRE II [3].

Keywords: Core-collapse supernovae, ^{11}B, ν-process, cross section, $^{7}Li(\alpha,\gamma)^{11}B$

Unité de recherche

CENBG, UMR 5797, 19 Chemin du Solarium, CS 10120, F-33175 Gradignan Cedex

To my Mom

Résumé - Français

Cette thèse commence par une introduction générale à l'astrophysique nucléaire qui s'intéresse plus particulièrement aux étoiles massives qui terminent leur cycle de vie par l'effondrement de leur cœur et une supernova (CCSN). Ces évènements sont le berceau du *ν-process*. Ce dernier, par l'intermédiaire de réaction avec des neutrinos, donne lieu à la réaction $^{7}Li(\alpha,\gamma)^{11}B$ qui participe à l'abondance de ^{11}B dans le système solaire. Ce travail a été effectué au laboratoire de science nucléaire (NSL) de l'université de Notre Dame, IN. Dans ce travail, le taux de réaction de $^{7}Li(\alpha,\gamma)^{11}B$ a été évalué aux températures pendant le *ν-process* via la mesure de sa section efficace aux énergies correspondantes.

Cette thèse se décompose ensuite en trois parties : La première s'intéresse à ce qui est connu de l'isotope ^{11}B et des différents canaux de la réaction $^{7}Li + \alpha$; La seconde partie décrit et étudie le setup expérimental ; La dernière partie présente l'analyse des données expérimentales menant aux calculs du taux de réaction.

Le chapitre consacré à l'isotope de ^{11}B et à la réaction $^{7}Li + \alpha$ commence par introduire la fenêtre de Gamow qui lie la température de site astrophysique aux énergies disponibles pour une réaction donnée. Pour la réaction d'intérêt ici, la fenêtre de Gamow est entre 0.25 MeV et 2.6 MeV dans le centre de masse. Ensuite sont présentées les données connues en ce qui concerne les énergies des niveaux excités de ^{11}B ainsi que les assignations de spin et parité.

Le chapitre continue en présentant les mesures expérimentales de $^{7}Li + \alpha$. Les diffusions élastiques et inélastiques sont d'abord présentées. Les mesures expérimentales de la capture radiative d'hélium sont ensuite discutées en commençant par les résonances à basse énergie, E_{cm} = 256 keV, 519 keV et 607 keV, qui ont beaucoup été étudiées et dont les forces de résonance sont connues. Les deux mesures faites à plus hautes énergies sont ensuite décrites. La première mesure par Heydenburg and Temmer [4] ne rapporte aucune résonance après celle à 607 keV. La seconde mesure par Paul et al. [1] rapporte une section efficace différentielle à 90° qui est normalisée avec la force de résonance de la résonance à 607 keV connue au moment de la publication, i.e. 3 eV, la force de résonance de cette résonance a depuis été mesurée par Hardie et al. [5] à 1.72 $\pm$ 0.17 eV soit environ la moitié. La section efficace différentielle rapporté par [1] est donc surestimée. Aucune autre transition que celle de la capture directe ou de la résonance vers l'état fondamental n'est observée. En utilisant les forces de transition établies par Weisskopf, on montre que d'autres transitions sont possibles. Pour finir ce chapitre, on s'intéresse aux efforts théoriques de calcul du facteur astrophysique S.

Le troisième chapitre de cette thèse est dédié à la description et à la caractérisation du setup expérimental. Tout d'abord, le laboratoire NSL est présenté avec ses trois accélérateurs

électrostatiques et leurs principales lignes de faisceau avec une emphase sur Sta. Ana qui atteint 5 MV et qui a été utilisé pour la mesure de la réaction. Une brève description de son fonctionnement est suivie d'une description de la ligne de faisceau utilisée : "Solid Target". Au bout de la ligne de faisceau se trouve la cible et un détecteur germanium orienté à 45°, utilisé pour détecter les rayons γ. Le fonctionnement du germanium est brièvement décrit. Un blindage est présent entre la cible et le détecteur pour bloquer les rayons γ à 478 keV provenant de la diffusion inélastique de l'hélium sur le lithium qui a une section efficace d'environ trois ordres de grandeur plus large.

Les sections suivantes s'intéressent aux cibles qui ont été utilisées. Pour les étudier, la courbe d'excitation de la résonance à $E_{cm} = 607$ keV a été exploitée suivant deux méthodes, La première méthode (1) est d'extraire la largeur à mi-hauteur qui est directement liée à l'épaisseur de la cible en termes d'énergie perdue ; la seconde méthode (2) consiste à intégrer cette courbe. Le résultat de cette intégration est directement liée au nombre d'atomes de lithium dans la cible. Le choix de cible et le choix du support pour la cible sont expliqués : la stabilité du LiOH est comparée à celle du LiF, deux supports sont comparés - tantallum et molybdenum - en terme de diffusion du lithium dans le support. Ce phénomène est quantifié, permettant de choisir un support.

Le chapitre se poursuit avec une description détaillée de la façon dont l'évolution du contenu en lithium a été suivie au cours du temps pendant l'expérience en utilisant les courbes d'excitation pour une mesure précise de l'épaisseur de la cible. Cette métode a pu être comparée pour trois rayons gamma différent provenant de la résonance à $E_{cm} = 607$ keV. Les épaisseurs calculées pour chacun de ces rayons gamma sont en accord. Le taux de rayon γ provenant de $^7Li(\alpha, \alpha')$ (rayon gamma de 478 keV) a également été utilisé entre chaque run, toujours à la même énergie dans le but d'avoir une information plus précise. Pendant les runs, le rayon gamma à 478 keV était également suivi de façon qualitative. L'information provenant de la diffusion inélastique démontre que nous pouvons traiter la dégradation des cibles de façon linéaire au cours du temps. L'épaisseur de chaque cible est rapportée et les méthodes (1) et (2) comparées procurent le même résultat.

Les méthodes et résultats de calibration du détecteur et de l'aimant d'analyse font l'objet des deux sections suivantes. Suite à la calibration du détecteur, son efficacité est déterminée pour les photo-pics entre 600 keV et 11000 keV ainsi que pour les pics dus à une simple échappée (511 keV plus petit que le photo pick). On utilise l'efficacité relative pour calculer les efficacités supérieur à 1.4 MeV. Pour terminer ce chapitre, le facteur de somme est présenté avec la méthode utilisée pour le calculer.

Le dernier chapitre de cette thèse rapporte l'analyse des données expérimentales de la mesure de la section efficace différentielle de $^7Li(\alpha, \gamma)^{11}B$.

Dans un premier temps, les caractéristiques générales des spectres γ obtenus sont présentées. La présence de bruit de fond est également discutée, particulièrement la présence d'un rayon γ avec une énergie similaire à celle d'un rayon γ associé à une transition de l'isotope ^{11}B. Il est estimé que ce rayon γ provient principalement de la réaction $^{9}Be(\alpha, n\gamma)^{12}C$. En effet, la largeur de ce pic ne nous permet pas de conclure qu'il ne provient pas de $^{7}Li(\alpha, \gamma)^{11}B$. Les conséquences de la diffusion du lithium dans le support de la cible sont évaluées entre les énergies $E_{cm} = 1.2$ MeV et $E_{cm} = 1.8$ MeV. Ces effets sont considérées négligeables.

Dans un second temps, les méthodes pour calculer les sections efficaces différentielles des transitions observées lors de nos mesures sont présentées et les deux contributions à la section efficace différentielle, celle due à la cascade depuis la résonance à travers le niveau à 5.02 MeV et celle due à la transition directe de la résonance ou capture vers l'état fondamental, sont calculées. Une autre transition au travers de létat excité à 4.445 MeV peut être observée pour les runs dont l'énergie du faisceau est inférieur à $E_{cm} = 1.15$ MeV, la section efficace différentielle pour cette transition est aussi calculée.

Malgré le manque de données expérimentales de distribution angulaire pour la réaction $^{7}Li(\alpha, \gamma)^{11}B$, la théorie de la matrice R est présentée puisque la théorie de la matrice A est utilisée pour obtenir la section efficace totale. La théorie de la matrice A, qui est un sous ensemble de la matrice R, est brièvement présentée.

Une première analyse montre que les données actuelement disponible pour les réactions $^{7}Li + \alpha$ ne sont pas conciliable. Ceci est également vrai pour $^{7}Li(\alpha, \gamma)^{11}B$, en effet, la section efficace différentielle calculée dans cette thèse et celle calculée par Paul et al. [1] sont incompatibles. Par conséquent, deux ajustements utilisant la matrice A sont réalisés: le premier avec les données mesurées dans cette thèse ainsi que l'une des mesure de $^{7}Li(\alpha, \alpha')$, le second avec les données rapportées par Paul et al. [1] corrigées et la même mesure de $^{7}Li(\alpha, \alpha')$. Les largeurs, $\Gamma_{\alpha}\Gamma_{alpha'}$ et Γ_{γ}, paramètres de la matrice A, sont extraits. Les forces de résonance des résonances à $E_{cm} = 1.2$ MeV, $E_{cm} = 1.59$ MeV, $E_{cm} = 1.66$ MeV et $E_{cm} = 1.94$ MeV sont calculées.

Deux sections efficaces totales sont extraites des ajustements faits avec la matrice A. Ces deux sections efficaces, celle de ce travail et celle du travail de Paul et al. [1] corrigé, sont en désaccord. Les raisons de ce désaccord sont explorées, cependant elles sont inconclusives. Ensuite, le facteur astrophysique S est calculé, avec les données expérimentales recueillies pour cette thèse, et présenté.

Dans un premier temps, les taux de réaction sont calculés séparément pour les résonances étroites et les résonances larges. Pour les résonances étroites, la force de résonance a été utilisée pour calculer le taux de réaction. Pour les résonances larges, l'intégration de la section efficace convoluée avec la distribution de Maxwell-Boltzmann est nécessaire, donnant également accès aux contributions non-résonnantes à ces énergies. Ensuite, Le taux de

réaction est calculé : c'est la somme des différentes contributions calculées précédemment. L'incertitude sur les taux de réaction est présenté séparement pour les taux de réaction liés aux différentes contributions, puis évalué pour le taux de réaction totale à partir des contributions.

Pour finir, les taux de réaction déduits des sections efficaces sont comparés l'un à l'autre ainsi qu'à ceux des compilations NACRE [2] et NACRE II [3]. Les deux taux de réaction calculés sont en accord entre eux ainsi qu'avec NACRE [2]. Le taux de réaction calculés avec les données de ce travail sont également en accord avec le taux de réaction calculé par NACRE II, ce n'est pas le cas du taux de réaction calculé en utilisant les données mesurées par Paul et al. [1]. Le taux de réaction calculé avec la mesure corrigée de Paul et al. [1] étant supérieur aux taux de réaction rappotés par NACRE [2], on explore des pistes pour comprendre d'oú vient le désaccord puisque les mesures récentes des différentes énergies des niveaux excités ou dans la mesure des masses ne sont pas suffisantes pour expliquer ce désaccord. Ceci est aussi vrai pour NACRE II [3] et on tente également d'expliquer le désaccord avec NACRE II [3].

Pour comprendre d'où vient le désaccord entre ce travail est le travail de Paul et al. [1] corrigé, on étudie les différences entre les contributions résonantes entre $E_{cm} = 1.2$ MeV and $E_{cm} = 1.95$ MeV. Pour cela, on utilise les formules de Breit-Wigner avec les paramêtres calculés avec la matrice A. On montre que la résonance à $E_{cm} = 1.59$ MeV a des contributions différentes dans les deux mesures expérimentales étudiées dans ce chapitre et ceci nous indique que c'est proche de cette énergie qu'il serait intéressant de mesurer de nouveau la réaction $^{7}Li(\alpha,\gamma)^{11}B$.

Mot-clés: Supernovæ à effondrement de cœur, ^{11}B, ν-process, section efficace, $^{7}Li(\alpha,\gamma)^{11}B$

Acknowledgements

This is a difficult exercise because I actually want to pour my heart out but there is no word to express how thankful I am to some of the amazing people in my life. So, here it goes...

I would like to start by thanking Fairouz Hammache and Alain Coc who agreed to make this thesis a better one in a short amount of time.

I would like to thank Michael Wiescher for having me in his lab for the past 4 year and Bertram Blank for making all of this possible: asking around for internships for me and later on taking me on as a Ph.D. student.

Thank you Manoel for your guidance and support in this work all the time, thank you for laughing at my drama and sometimes worrying about it. Thank you for being so funny, smart and kind. Thank you for letting me pop-up in your office any time I had something to say or did not understand a thing.

Joachim Görres, thank you for your guidance over the years and letting pick a little bit of your tremendous knowledge of gamma-ray spectroscopy. Thank you for your funny and kind self.

Thank you James DeBoer for all your help on the R-matrix analysis, for taking the time to answer all my questions and checking that it was all making sense.

I also would like to thank Ed Stech, Dan Robertson and Anna Simon for their help and support when my heart was set on graduating. I also would like to thank Janet Weikel for her help and support all the time throughout my time at Notre Dame.

Thank you to my office-mates, Michael, Tyler and Ed L. as well as my group-mates Luis, Mike, Zach and Shane for all the crazy conversation, the drama, the laughter and the science discussion. I will miss it.

I would like to thank Angela for her friendship and for trying to keep me in touch with the world. I also would like to thank Audrey, my sister, and her family, Julia, Hugo and Erwan, thank you for being there all the time. Thank you to my brother and my dad for their presence.

I would like to thank Marion and Pauline for getting me through the last months and the interviews laughing, thank you for rocking my world.

I also would like to thank my friends in France who, despite what life threw at them, were always present to send me a copy of Pride and Prejudice or letting my sleep on their sofa: Mathilde, Cecile, Jean, Anne-Laure, Flavie, Aurore, Sophie and Lea.

Last but not least, I would like to thank you, Chris, for your support, your help at times, for always saying what is needed, for your love.

Contents

List of Figures

List of Tables

Chapter 1

Introduction

Stars live and die. Events in their life are determined by their initial mass and environment. Their environment influences the elements present at their formation. Throughout their life, depending on their mass and composition, stars go through different numbers of burning stages which are carried on by nuclear fusion reactions.

Stars are formed in nebulae in which gas and dust gather to form denser regions and eventually something large enough to form a protostar. The initial material is mostly constituted of hydrogen and helium, the most abundant element in the universe. Beside hydrogen, the rest of the initial composition of the star depends on the origin of the material that formed it. For instance, did it experience prior stellar nucleosynthesis, or from what type of stellar events did it originate?

As the forming star contracts, its interior temperature increases. Eventually, the temperature is high enough for fusion reactions to be possible. The energy released by these reactions provides a radiation pressure opposing the gravitational contraction. The star reaches equilibrium between gravitational pressure and radiation pressure.

Being the most abundant element, and because of its low Z, hydrogen is the first element to experience fusion reactions. The first burning stage to provide the radiation pressure is therefore hydrogen burning; it is the first burning and, hence, every star experiences it. It is also the slowest burning. The fusion of four hydrogen into a helium can occur in two different ways: the proton-proton chain (pp-chain), Eq.1.1, or the CNO cycle, Eq.1.2.

$$
\begin{aligned}
{}^1H +^1 H &\rightarrow \nu_e + e^+ + D \\
D +^1 H &\rightarrow^3 He + \gamma \\
{}^3He +^3 He &\rightarrow^1 H +^1 H +^4 He
\end{aligned}
\tag{1.1}
$$

$$
\begin{aligned}
{}^{12}C +^1 H &\rightarrow^{13} N + \gamma \\
{}^{13}N &\rightarrow^{13} C + \nu_e + e^+ \\
{}^{13}C +^1 H &\rightarrow^{14} N + \gamma \\
{}^{14}N +^1 H &\rightarrow^{15} O + \gamma \\
{}^{15}O &\rightarrow^{15} N + \nu_e + e^+ \\
{}^{15}N +^1 H &\rightarrow^{12} C +^4 He
\end{aligned}
\tag{1.2}
$$

They are both slow processes with the pp-chain being slower than the CNO cycle (in Eq. 1.2, the last reaction, $^{15}N(\alpha,\gamma)^{12}C$ closes the cycle). The pp-chain is slower because the first reaction of the pp-chain fusing two protons into a deuterium happens via the weak interaction. In low mass stars, the pp-chain dominates, while in stars with mass higher than 1.3 $M_\odot$ (where $M_\odot$ is the solar mass), which are hotter environments, the CNO cycle is the dominant source of energy. This is assuming that the stars here are not from the first generation of stars (very few elements aside from hydrogen and helium exist at the time). Both of these processes convert four protons into helium.

As the fuel is consumed, the current burning will slow down and eventually the reactions of this burning will not release enough energy to sustain the star. Then, the star contracts increasing the density and temperature in the core. The increase allows for the next burning phase to take place, usually, involving heavier nuclei, it also allows to overcome the Coulomb barrier between heavier nuclei. The former fuel is pushed out on a shell surrounding the core. The new fuel, ashes of the previous burning, is now burned in the star core.

The different core burning stages are the following, in order of occurrence: hydrogen burning, helium burning, carbon burning, neon burning, oxygen burning and, finally, silicon burning.

Stars with mass between 8 $M_\odot$ and 100 $M_\odot$ will likely go through all these burning stages and reach silicon burning during which iron group nuclei -from ^{52}Cr to ^{64}Ni- are produced via alpha capture on the ashes of Oxygen burning.

The last burning, silicon burning, only last a few days, the temperature is at its highest, reaching $T_9 \sim 3.5$ at the beginning, where T_9 means temperature in GK. Table 1.1 represents the different evolutionary stages of a typical 15 $M_\odot$ star displaying for each fuel, what the ashes are, the density and temperature of the stars. It also displays the time scale of each burning stage. In Fig. 1.1, panel a), is a simple view of the shell and core burning in the star during the silicon core burning.

Stage	Timescale	Fuel	Ash	Temperature (10^9 K)	Density ($g.cm^{-3}$)
Hydrogen	11 Myr	H	He	0.035	5.8
Helium	2.0 Myr	He	C, O	0.18	1.39×10^3
Carbon	2000 yr	C	Ne, Mg	0.81	2.8×10^5
Neon	0.7 yr	Ne	O, Mg	1.6	1.2×10^7
Oxygen	2.6 Myr	O, Mg	Si, S, Ar, Ca	1.9	8.8×10^6
Silicon	18 d	Si, S, Ar, Ca	Fe, Ni, Cr, Ti	3.3	4.8×10^7
Iron core collapse	$\sim$ 10 s	Fe, Ni, Cr, Ti	Neutron star	> 7.1	$> 7.3 \times 10^9$

TABLE 1.1: Evolution of a typical 15 solar mass star [6]. This will vary depending on the mass of each star as well as on the environment they evolve in.

After silicon burning, iron burning does not occur. If it were to occur, it would accelerate the star contraction. After silicon burning, the star is likely to go through a Core-Collapse Supernovae (CCSN) explosion: the core is going to collapse and eject all matter surrounding the nascent neutron star into the interstellar medium (ISM). Along with matter, a tremendous amount of neutrinos are ejected from the core. These neutrinos are the source of the ν-process. In this chapter, we will explain how we get from silicon burning to the ν-process and specifically to the production of ^{11}B.

1.1 End of Silicon burning and electron degeneracy pressure

During silicon core burning, the fusion of ^{28}Si with ^4He nuclei (created by photodisintegration), which are due to the photodisintegration of heavy nuclei, will give rise to iron group nuclei. The ^{28}Si fuses with one ^4He at a time to go up to $A = 56$, where A is the mass number of a given nucleus. Just as in every other burning stage, when the fuel reaches exhaustion, the core contracts. Unlike every other burning stage, the iron nuclei do not ignite to start a new core burning. Indeed, iron has the largest binding energy per nucleon and it takes energy to fuse them with another nuclei.

While the core contracts, the electrons reach the Fermi level. The electron degeneracy pressure, which is the expression of the Pauli exclusion principle in stellar environments, stops the contraction.

The electron degeneracy pressure is overcome when the Chandrasekhar mass limit is reached [7]:

$$M_{ch} \sim 1.44(\frac{Y_e}{0.5})^2[1 + (\frac{s_e}{\pi Y_e})^2 M_\odot] \tag{1.3}$$

where Y_e is the electron fraction, s_e is the entropy of the electrons, and $M_\odot$ is the mass of the sun.

Eq. 1.3 allows the estimation of the maximum mass the core can reach, depending on the electron fraction and electron entropy. M_{ch} is usually between 1.4 $M_\odot$ and 1.7 $M_\odot$.

When the Chandrasekhar mass is reached, the electron degeneracy pressure is overpowered; gravity takes over and the core starts its collapse.

1.2 Core-Collapse Supernovae

As the core collapses, electrons capture onto heavy nuclei (and the few free protons available) via the weak interaction reaction. Electron captures are responsible for the neutronization of the core:

$$p + e^- \rightarrow n + \nu_e \tag{1.4}$$

Electron captures are also responsible for the presence of neutrinos in the core while beta decay of neutron rich nuclei, also due to the weak interaction, are the source of anti-neutrinos during the collapse:

$$^A_Z X \rightarrow ^A_{Z-1} X + \bar{\nu_e} + e^- \tag{1.5}$$

The infalling matter accumulates faster on the edge of the inner core, Fig. 1.1, panel b. The speed of the infalling matter decreases steeply as the distance from the inner core increases. The different shells surrounding the iron core experience a much slower collapse and, on the timescale of the collapse, are barely disturbed by it.

As the core collapses, its density, initially $\sim 10^8 g.cm^{-3}$, and temperature, ~ 9 GK, increase dramatically. The collapse is accelerated by the electron capture on heavy nuclei, taking

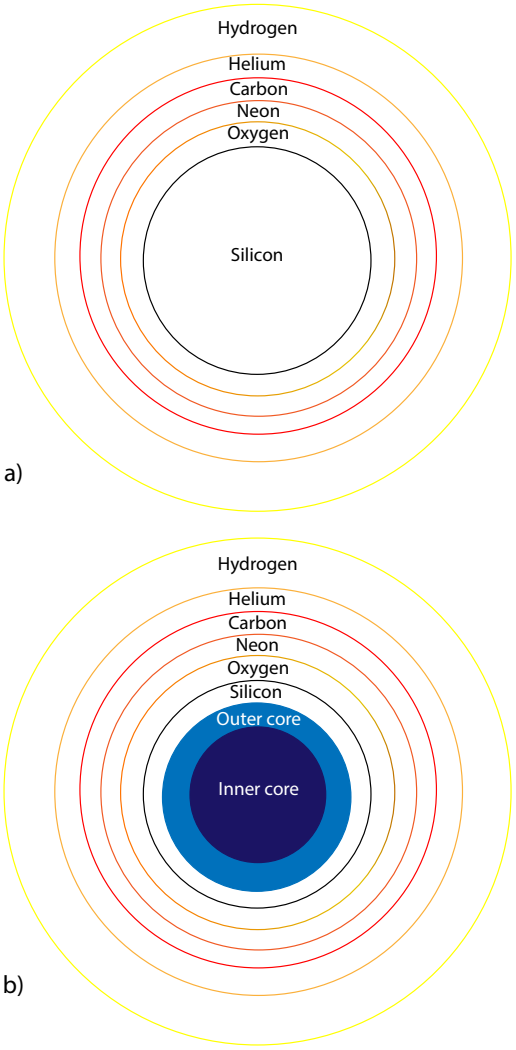

FIGURE 1.1: Schematic (not to scale) of the onion-like structure of a star, during silicon burning (a) and during the first part of the collapse (b).

away from the radiation pressure, free nucleons and the subsequent escape of low energy electron neutrinos.

The mean free path of the neutrinos at $4 \times 10^{11} g.cm^{-3}$ is about 0.5 km for a 20 MeV neutrino [8] and the radius of the core is about 200 km. When the inner core reaches this density most of the neutrinos are trapped.

1.2.1 The first shock wave

At this time, the inner core's infalling speed is about 30% of the speed of light. The electrons are still being captured on nucleons, which are mostly free in the inner core. Because of

the Pauli exculsion principle, the nucleons produce neutrinos with increasing energy. The temperature in the inner core increases up to 100 GK [9].

When the inner core density reaches nuclear matter density, $\rho \sim 2 \times 10^{14} g.cm^{-3}$, the strong force, which was an attractive force so far, becomes repulsive. The collapse of the inner core, the nascent proto-neutron star (PNS), abruptly stops. This induces a shock wave travelling outward.

Behind the shock, propagating in the outer core, the production of electron neutrinos through electron capture keeps on going. A great part of what stalls the first shock wave is the energy loss in photodissociating the layer around the PNS and the subsequent loss of neutrinos.

The first shock wave is stalled at a radius of $\sim$ 150 km [9], well before reaching the first outer shell (i.e. silicon shell).

1.2.2 The second shock wave

The emergence of the second shock wave leading to the supernovae explosion is a long standing puzzle in the field. Very few simulations lead to the CCSN explosion observed. In 3 dimensions (x,y,z), only one simulation had lead to an explosion [10]. In 2D and 1D, the energy released is far from reality because many parameters are left out such as turbulence or non spherical 3D convections. Below, two models are presented, the original model and the model thought more promising by experts in the field.

1.2.2.1 The prompt shock mechanism

The prompt shock was one of the theories intensely investigated in the 1980's because it is the simplest. The idea is to consider that the first shock is not stalled and will lead to the supernovae explosion. The inner core reaching nuclear density, the core bounce would be powerful enough to lead to the explosion. This requires cores that are much larger than the Chandrasekhar mass. The more precise the physics in simulation is, the less this hypothesis seems to be a possible explanation [7].

1.2.2.2 ν heating mechanism

The neutrino heating mechanism was proposed by Bethe and Wilson [11]. They consider that after the first bounce, the core keeps collapsing getting bigger, denser and producing neutrinos with energies higher than a few MeV.

After the first shock wave, the temperature drops outside the PNS, with a dependence of r^{-1}, because of the first shock wave which has allowed neutrinos to escape. The temperature also drops inside the PNS with the emission of neutrinos. These neutrinos can escape because, with the decrease in temperature, the density decreased as well. The neutrinos also have on average lower energies due to diffusion in the PNS to reach out. These cooling neutrinos escape the gain layer. The gain layer corresponds to what is being accreted at high speed and will become, with the PNS, the neutron star. On the account of an intense neutrino flux leaving the nascent PNS and excited nuclei, the material contained in the layer surrounding the gain layer is being photodissociated. The photodissociations leave free nucleons in the layer surrounding the gain layer.

The photodissociation of the layer around the gain layer is crucial to the explosion. The gain layer accretes on the PNS while the neutrinos dissociate the layer above. Similarly to what induces the first shock, when the density in the nascent neutron star reaches nuclear matter density, the accretion abruptly stops. The second shock wave arises. The layer surrounding what will be the neutron star is already dissociated. This second shock wave is, then, successful in exploding the star because the shock wave does not lose a lot of energy to photodissociation. The outburst of neutrinos takes apart the layers of the star; this is the supernovae explosion.

During the outburst, the neutrino interacting with the atoms leaves them in either atomic or nuclear excited states. The X-rays emitted are the source of the visible explosion and can outshine the host galaxy of the supernovae.

The neutrino heating mechanism simulations do not always successfully lead to the supernovae explosion, but seems to be the more promising scenario as to how does the supernovae explode [9].

1.2.2.3 Nomenclature

Supernovae are classified depending on the features in their spectra. In this paragraph, the different type of supernovae which are CCSN are layed out.

Two types of supernovae exist: the supernovae Type I, identified by the absence of hydrogen in its spectra, and the supernovae Type II, which present these hydrogen lines. The Supernovae type I can be separated in, at least, 2 sub types: type Ib and Type Ic supernovae, which present different feature of the helium line in their spectra. All the supernovae Type II are CCSN.

There are many more sub types of supernovae Type I, but these are not CCSN.

1.3 Nucleosynthesis with neutrinos

The explosion of the supernovae 1987A (SN1987A) in the Large Magellanic Cloud in 1987 was an important event because it took place at a close distance from Earth. It was the first time neutrinos from a supernovae were ever measured (Kamiokande II 12 events [12], IMB 6 events [13] and another 6 events in the detectors of the Baksan experiment).

Observing as many as 24 events during the explosion of SN1987A made it clear that an enormous amount of neutrinos were emitted from the newly formed neutron star through the different layer of the star.

Despite low neutrino-nucleus interaction cross sections, neutrinos are responsible for two types of nucleosynthesis processes. The νp-process, which is the capture of $\bar{\nu_e}$ on protons creating a neutron and a positron followed by (n,p) reactions on proton-rich matter producing p nuclei for $64 < A < 100$. The second one, the ν-process participates to the nucleosynthesis of some light elements and some odd-odd nuclei, this will be discussed in more details below.

1.3.1 Neutrino interaction

Interactions with neutrinos are governed by the weak interaction. Neutrinos have 2 ways of interacting with particles:

- The interaction is carried by a boson Z^0, these interactions are called neutral current reactions which do not involve electrons, muons or taus such as $\nu_e\bar{\nu_e} \rightarrow \nu_\mu\bar{\nu_\mu}$ or ${}^AX(\nu,\nu'){}^AX^*$.
- The interaction is carried by the W^+ or the W^- boson. These interactions are called charged current reactions and these reactions do involve electrons, muons or taus such as ${}^A_ZX(\nu_e,e^+){}^A_{Z-1}X^*$.

The electron neutrinos produced during a CCSN are mostly produced by a charged current interaction: electron capture on heavy nuclei, Eq. 1.4, and β decay of neutron-rich nuclei, Eq. 1.5. The two other neutrino flavors will arise from neutrino oscillations or from reactions between electronic neutrinos and anti-neutrinos [14]:

$$\begin{aligned} \nu_{e^-}\bar{\nu_{e^-}} &\rightarrow \nu_\tau\bar{\nu_\tau} \\ \nu_{e^-}\bar{\nu_{e^-}} &\rightarrow \nu_\mu\bar{\nu_\mu} \end{aligned} \tag{1.6}$$

In the conditions of a supernovae, the muonic and tauic neutrinos and anti-neutrinos quasi exclusively interact via neutral current with the surrounding matter because creating a muon or a tau requires a lot of energy in comparison to creating an electron. It is energetically more convenient to create electrons. Consequently, the charged current reactions only occur with electrons and electronic neutrinos.

The neutral current reaction can happen with any neutrino available. The neutrino-nucleus interaction cross section increases with energy, and the mean free path of a neutrino is proportional to the inverse of the neutrino-nucleus interaction cross section.

The following approach provides an idea of how many neutrinos are available:

- the energy released through neutrinos by a supernovae is $E_\nu^{total} \sim 10^{53}$ erg [15]
- the average energy of a neutrino is 10 MeV which correspond to $\sim 1.6 \times 10^{-5}$ erg.

Using these numbers, we estimate $\sim 6 \times 10^{57}$ neutrinos emitted by the supernovae and available to react!

The neutrino-nucleus cross sections are small. In Ref. [15], they calculate charged current reactions, (ν_e, e^-), neutrino-nucleus cross sections for the light nuclei produced via the ν-process and find cross sections of the order of $10^{-42}\ cm^2 \equiv 10^{-18}\ barn$. Cross sections of

neutral current reactions, (ν, ν') are smaller, as can be seen on Fig. 1.2, however, they are more likely to occur.

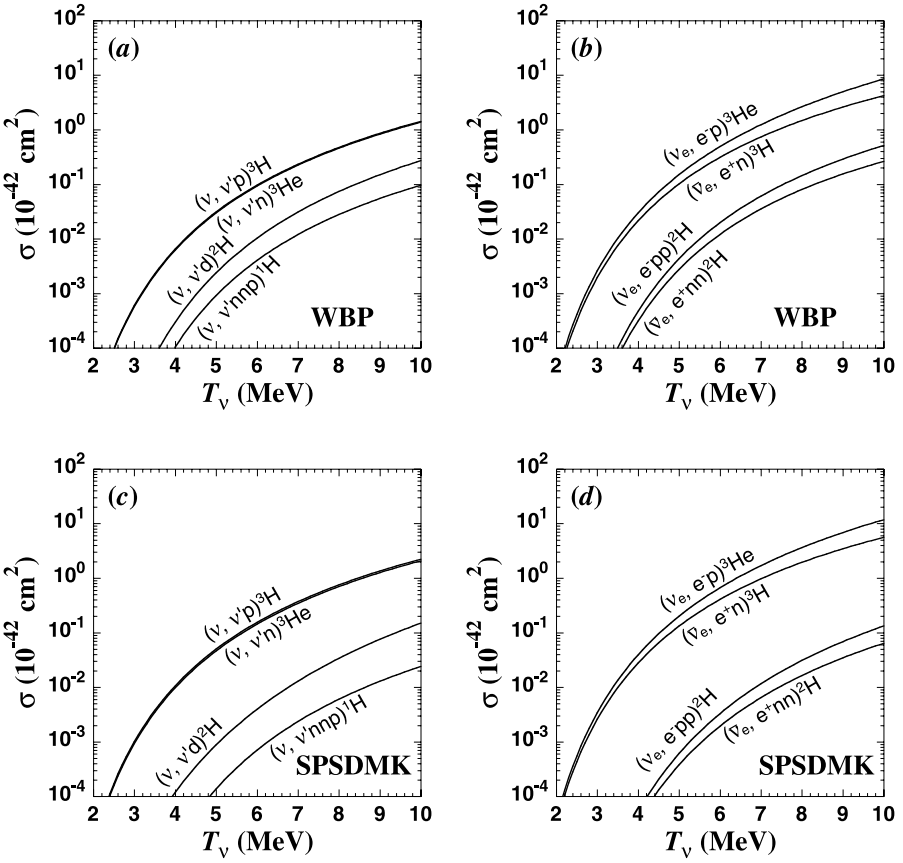

FIGURE 1.2: Figure from [15]. Neutrino and anti-neutrino reaction with ^4He. Two different hamiltonians are used (WBP and SPSDMK). The neutral current reactions are on panels a and c. Charged current reactions are on panel b and d.

Fig. 1.2 shows only the reaction on helium nuclei, but Yoshida et al. [15] and Heger and Woosley [16] calculate other cross sections of interactions between neutrinos and nuclei and do show that they have the same order of magnitude as the one shown here.

1.3.2 The ν-process

The first ν-process simulation was done by Woosley in 1990 [17] after the observation of 1987A. In this paper, the impact of the ν-process is detailed going through each shell of a typical 20 $M_\odot$ star undergoing a supernovae explosion. They identify five stable nuclei sensitive to the ν-process: ^7Li, ^{11}B, ^{19}F, ^{138}La and ^{180}Ta.

The production of ^{138}La and ^{180}Ta does not happen during the burning stages of the stellar evolution. The isotopes ^{11}B and ^{19}F, if produced during stellar evolution, are subsequently destroyed [18, 19]. The measured abundance of ^7Li is not fully understood

[20]. For these reasons the galactic abundances of ^{7}Li,^{11}B,^{19}F are smaller than the ones of other light stable nuclei and much smaller than the nuclei around them, i.e. helium, carbon, oxygen and neon. ^{138}La,^{180}Ta are only made in explosive nucleosynthesis, being too heavy for production through the burning stages in stellar evolution. These 5 nuclei were identified as being made in CCSN through the ν-process: when calculating their abundance, there is a large difference in their abundance calculated with and without neutrinos. This demonstrated that the ν-process contributes to their galactic abundance. In the case of ^{11}B, adding the abundance coming from the ν-process calculation to the abundances from galactic cosmic ray spallation (GCRS) got its galactic abundance closer to the measured value [17]. The ν-process contribute up to 15% to the galactic abundance of ^{11}B [21].

Pre-solar silicon carbide grains from primitive meteorites are formed in winds of evolved stars and ejecta of stellar explosions (novae, supernovae). They allow us to get information about the abundances in the medium characteristic to these environments and, eventually, to constraint nucleosynthesis. A study of 12 pre-solar grains coming from CCSN in 2011 [22] had quantities of $^{7}Li/^{6}Li = 11.83 \pm 0.29$ and $^{11}B/^{10}B = 4.68 \pm 0.31$. The solar abundances of ^{7}Li and ^{11}B are mostly due to GCRS [23], however Fujiya et al. [22] argue it to be very unlikely for the grains to have been contaminated by GCRS, and therefore, the previously mentioned ratio represents only the ratio from the CCSN.

1.4 Boron production during core collapse supernovae

During the supernovae explosion ^{11}B is produced, via the ν-process, in every shell of the stellar envelope in different quantities [24]. It is in the helium layer that ^{11}B is most likely to be produced via the following chain of reactions [24, 25, 26]:

$$^{4}He(\nu_e, \nu'_e p)^{3}H(\alpha,\gamma)^{7}Li(\alpha,\gamma)^{11}B \tag{1.7}$$

This chain of reactions is responsible for most of the ^{11}B produced in a CCSN. This makes sense in the light of the neutrino-nucleus cross sections discussed in section 1.3.1: ^{4}He is much more abundant in the star envelope than ^{12}C and neutral current reactions are more likely to occur.

A study by Yoshida et al. [15] of 5 different ν-process calculations with varying neutrino energies in type II supernovae conditions found that $\sim 60\%$ of ^{11}B was made in the He/C

layer where most of it was created through the reaction chain in Eq. 1.7. There are, however, other ways to create ^{11}B through the ν-process such as $^{12}C(\nu,\nu'p)^{11}B$, $^{12}C(\nu_e,e^+p)^{11}B$ and $^{12}C(\bar{\nu_e},e^+n)^{11}B$ which can contribute up to 16% to the production of ^{11}B during the ν-process [27].

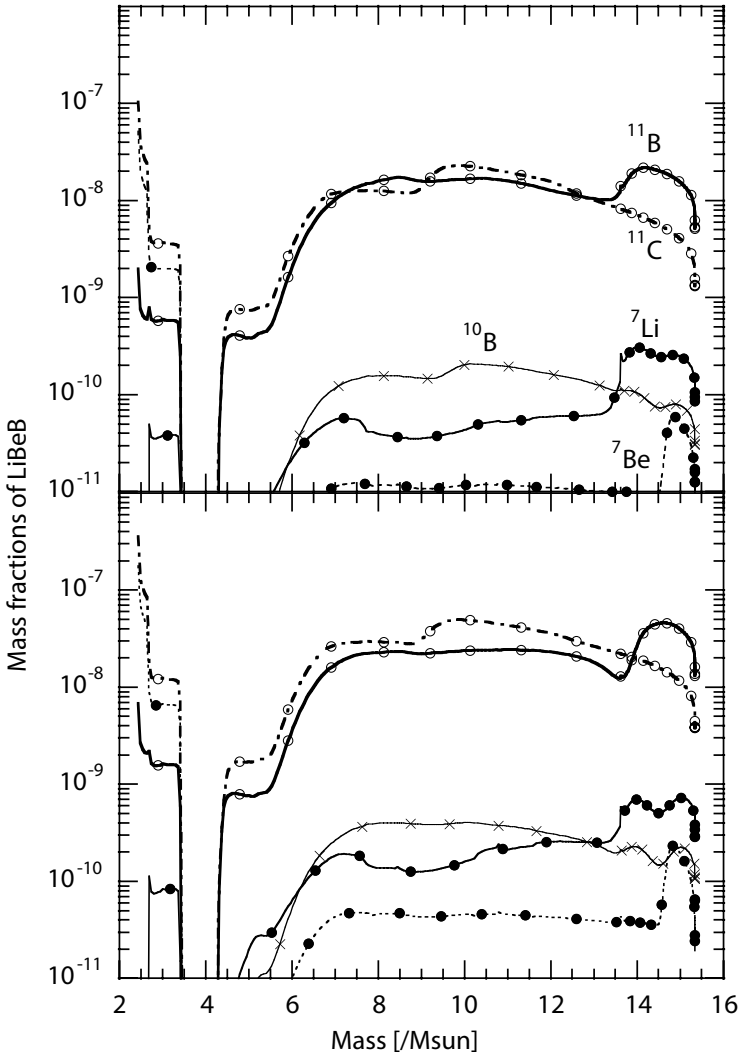

FIGURE 1.3: Evolution of the mass fraction of Li, Be, B throughout a $15M_\odot$ star based on a Type Ic supernovae simulation, from [28]. The top panel display results for $T_{\nu_{\mu\tau}} = 6$ MeV. The bottom panel displays result for $T_{\nu_{\mu\tau}} = 8$ MeV

In Fig.1.3 the mass fraction of light elements produced by the ν-process, 75 second after core bounce, versus the enclosed mass of a 15 $M_\odot$ star for a Type Ic supernova simulated by Nakamura et al. [28] is shown. The mass fraction corresponds to the abundance of element X compared to the abundance of all element produced. The bottom and top panel display two simulations with neutrinos of different temperatures (distribution of speed). The top panel shows results for $T_{\nu_e} = 3.2$ MeV, $T_{\bar{\nu_e}} = 5$ MeV and $T_{\nu_{\mu\tau}} = 6$ MeV and the bottom panel shows results for $T_{\nu_e} = 3.2$ MeV, $T_{\bar{\nu_e}} = 5$ MeV and $T_{\nu_{\mu\tau}} = 8$ MeV where $< E_\nu > \propto T_\nu$ [29].The difference between the top panel and bottom panel lies in the energy

given to the different neutrino species, on the bottom panel, $T_{\nu_{\mu\tau}}$ has higher energy than on the top panel. On the left side of Fig.1.3, we see the abundance of light elements in the layer close to the neutron star ($M_r < 4\ M_\odot$) and then moving to the right in more outward layers ($M_r > 4\ M_\odot$). We can see that ^{11}B is produced across the material surrounding the neutron star. On the right side of Fig.1.3, is the last layer (helium layer) of the simulated star.

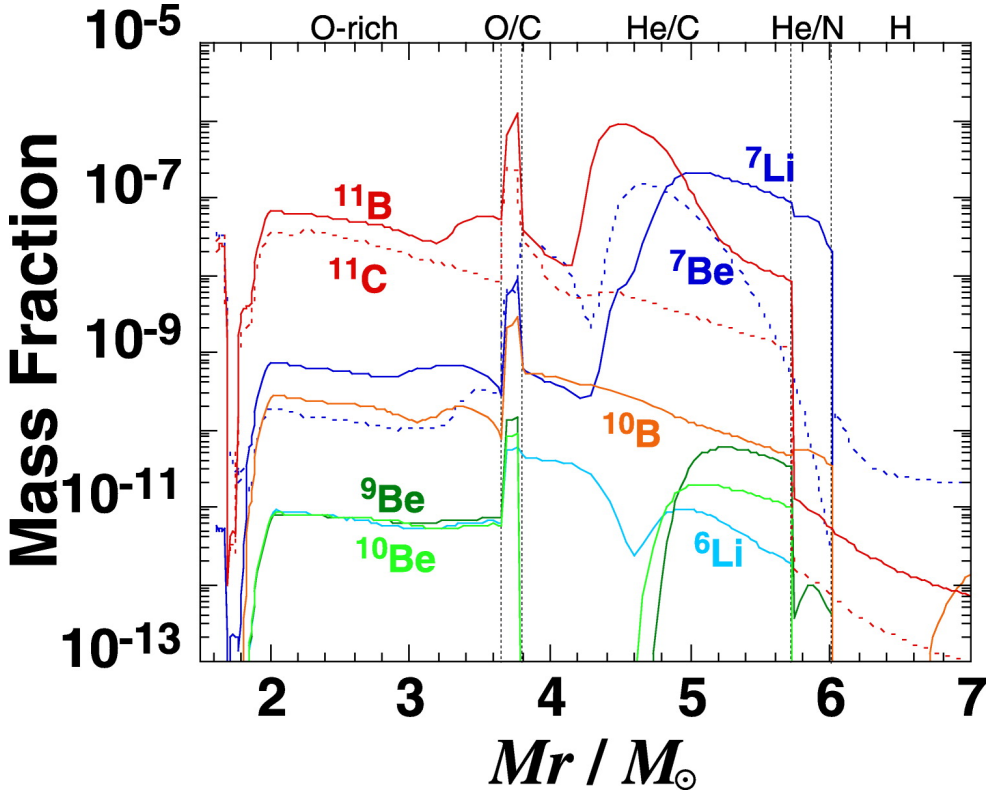

FIGURE 1.4: Evolution of Li, Be, B for a 16 $M_\odot$ star based on a Type II supernovae simulation, from [15]. This simulation was done with $T_{\nu_e} = 3.2$ MeV, $T_{\bar{\nu_e}} = 5$ MeV and $T_{\nu_{\mu\tau}} = 6$ MeV. The different colors represent the different contributions to the abundance of a given element.

In Fig. 1.4, the mass fraction of light elements produced by the ν-process, 1000 s after core bounce, versus the enclosed mass of a 16.2 $M_\odot$ star for a Type II supernova simulated by Yoshida et al. [15] is shown for neutrino temperature of $T_{\nu_e} = 3.2$ MeV, $T_{\bar{\nu_e}} = 5$ MeV and $T_{\nu_{\mu\tau}} = 6$ MeV. In this particular simulation, part of the external layers of the star have already been blown away. The isotope of ^{11}B is produced across the material surrounding the neutron star, as we could observe for a Type Ic supernovae model in Fig. 1.3.

At first, it seems like Type Ic supernovae would be the main contribution to the abundance of boron in the universe. The largest ^{11}B abundance in this model is in the outer layer naturally facilitating the ejection of ^{11}B in the ISM. In Type II supernovae there is a layer of hydrogen around the helium layer which could affect the ability of ^{11}B to be ejected from

the helium layer. As can be observed in Fig. 1.4, ^{11}B is produced in the He/C layer with a higher probability compared to its production in Type Ic supernovae models, see top panel of Fig. 1.3. Despite the hydrogen layer to cross, Type II supernovae contribute more to the abundance of ^{11}B in the universe than Type Ic supernovae [28].

The ^{11}B galactic abundance is calculated based on theoretical calculations of $^{7}Li(\alpha,\gamma)^{11}B$. An experimental determination of the reaction rate is critical to validate models that conclude that $^{7}Li(\alpha,\gamma)^{11}B$ contributes significantly to the universal abundance of ^{11}B through the ν-process in CCSN. It would also constrain neutrino energies. A recent paper by Sieverding et al. [29] shows that a change of neutrino energies of $\sim$ 2 MeV can change the ^{11}B yield by an order of magnitude for several stars with different initial masses (see Fig. 2 in [29]).

1.5 $^{7}Li(\alpha,\gamma)^{11}B$ and the neutrino mass hierarchy

Aside from the contribution of the reaction rate of $^{7}Li(\alpha,\gamma)^{11}B$ to the universal abundance of ^{11}B in CCSN, this reaction also constrains the relative abundance of ^{7}Li and ^{11}B. Several papers [15, 27, 30] have suggested that this relative abundance ratio could better constrain the neutrino mass hierarchy.

The neutrino flavors (e, μ, τ) and mass eigenstates (1, 2, 3) are related via a unitary matrix U such as:

$$\begin{pmatrix} \nu_e \\ \nu_\mu \\ \nu_\tau \end{pmatrix} = U \begin{pmatrix} \nu_1 \\ \nu_2 \\ \nu_3 \end{pmatrix} \tag{1.8}$$

The unitary matrix U expression is:

$$\begin{aligned} U = & \begin{pmatrix} 1 & 0 & 0 \\ 0 & cos(\theta_{23}) & sin(\theta_{23}) \\ 0 & -sin(\theta_{23}) & cos(\theta_{23}) \end{pmatrix} \times \\ & \begin{pmatrix} cos(\theta_{13}) & 0 & sin(\theta_{13})e^{-i\delta} \\ 0 & 1 & 0 \\ -sin(\theta_{13})e^{-i\delta} & 0 & cos(\theta_{13}) \end{pmatrix} \times \begin{pmatrix} cos(\theta_{12}) & sin(\theta_{12}) & 0 \\ -sin(\theta_{12}) & cos(\theta_{12}) & 0 \\ 0 & 0 & 1 \end{pmatrix} \end{aligned} \tag{1.9}$$

where θ_{12}, θ_{23} and θ_{13} are the mixing angles and δ is the CP violating phase (charge and parity symmetry violation). They are the parameters used to describe the neutrino mixing.

Studies show that the abundance ratio of $^{7}Li/^{11}B$ could discriminate whether the mass hierarchy is normal, $m_1 < m_2 < m_3$, or inverted, $m_3 < m_1 < m_2$ [15, 27, 30]. This is important as the neutrino oscillation probability is a function of the mass differences ($m_1^2 - m_2^2$, $m_3^2 - m_2^2$, $m_1^2 - m_3^2$) and the mixing angles (θ_{12}, θ_{23}, θ_{13}), an example can be found in Qian and Vogel [31]. The probability of interacting presents different resonances if the mass hierarchy is inverted or normal.

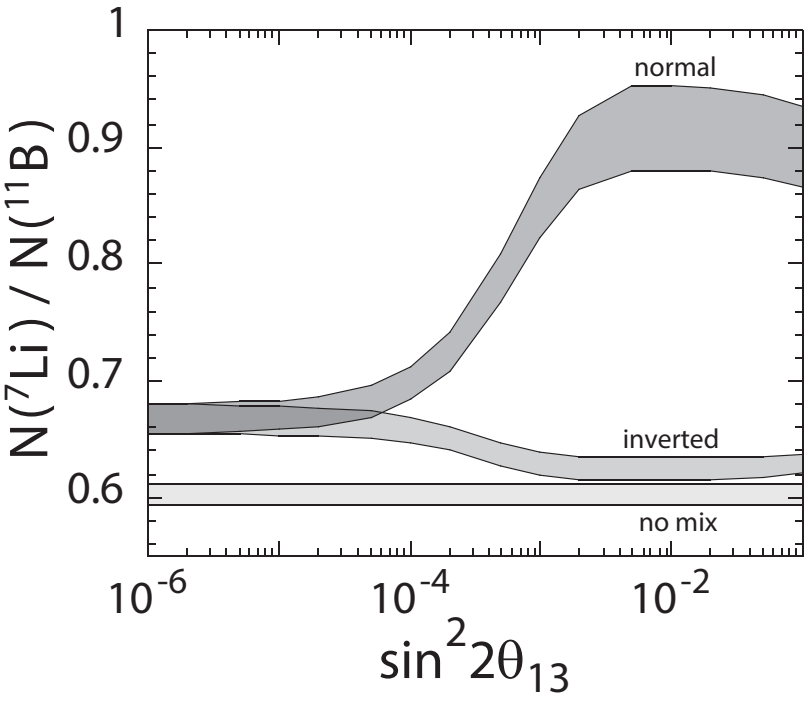

FIGURE 1.5: Impact of $sin^2(2\theta_{13})$ on the $^{7}Li/^{11}B$ ratio. The dark shaded region corresponds to the normal mass hierarchy, the medium shaded region corresponds to inverted mass hierarchy and the light shaded region corresponds to the absence of neutrino oscillation, figure from [15].

The result of a sensitivity study by Yoshida et al. [15] looking at the impact of the neutrino mass hierarchy on the relative abundance ratio of ^{7}Li to ^{11}B is shown in Fig. 1.5. In that study, the reaction rate of $^{7}Li(\alpha,\gamma)^{11}B$ was kept constant. The author concludes that knowing the abundance ratio of $^{7}Li/^{11}B$ with greater precision would contribute to probing the neutrino mass hierarchy. Constraining the models to understand exactly how ^{11}B and ^{7}Li are brought to our galaxy is part of that knowledge.

Studying $^{7}Li(\alpha,\gamma)^{11}B$ at the energies relevant to the ν-process will help constrain the $^{7}Li/^{11}B$ abundance ratio.

1.6 $^{7}Li(\alpha,\gamma)^{11}B$ reaction in other contexts

There are a few additional reasons to study the $^{7}Li(\alpha,\gamma)^{11}B$ reaction, below are some examples.

A source of background in laboratory experiment:

Nuclear reactions with very small cross sections are difficult to study due to natural background radiation. They are studied in underground laboratories such as LUNA [32] or CASPAR [33]. The natural shielding provided by the ground decreases the background contribution from cosmic rays induced γ-rays and neutrons. These underground laboratory can get rid of most of the background that we see on the surface and especially the high energy background. Due to this, the largest contribution in these laboratories will come from beam induced background.

While at its origin the main goals of the LUNA laboratory was to study proton induced reactions [34], the LUNA-MV upgrade and CASPAR plan to study alpha induced reactions. To understand the potential background from beam induced background, it is important to know the dominating reaction involved.

As ^{7}Li is a contaminant to most metals, the (α,γ) reaction on ^{7}Li will contribute to the expected background.

The mirror reaction:

$^{7}Be(\alpha,\gamma)^{11}C$ is of relevance for the νp-process because it is the breakout from the pp-chain that will affect the proton to seed ratio for the νp-process [35].

Plasma physics:

It is not uncommon in plasma physics to contaminate a plasma in order to have access to some of its characteristic. $^{7}Li(\alpha,\gamma)^{11}B$ presents resonances at low energy which are convenient to assess the temperature of a plasma [36, 37].

The cosmological ^{7}Li problem:

The cosmological Li problem arises from the fact that the abundance of Li after the Big Bang and the most reliable parameter free model of Big Bang nucleosynthesis do not agree. The Big Bang Nucleosynthesis (BBN) model, which relies on reaction rates, is able to reproduce exactly the abundance of deuterium and almost exactly the one of helium. But

the result of the BBN model is a factor 3 higher than the abundance of ^7Li estimated from measurement when it comes to the primordial abundance of ^7Li.

The primordial abundance of ^7Li is estimated from the Spite plateau [38]. By measuring ^7Li in old stars, these authors realized that the abundance of ^7Li was not changing above a certain temperature (older stars are warmer). Besides, ^7Li is produced and destroyed with a proton in the pp-chains to produce two ^4He. They, thus, concluded that if there was a constant amount of ^7Li, it was most likely from the Big Bang.

Spite and Spite [38] do compare the abundance they infer from the Spite Plateau and find it to match with the model they compare the measured abundance with. As the measurements and model became more precise, the Li cosmological problem arose.

It was believed that a change in reaction rate of one of the reactions in the BBN model network could resolve the cosmological ^7Li problem [39]. Recently, according to Coc [40] and Cyburt et al. [41], it seems that the nuclear solution will not resolve the discrepancy.

Chapter 2

The $^7Li + \alpha$ reaction and its compound nucleus

This chapter will focus on the $^7Li + \alpha$ reaction and its compound nucleus ^{11}B. The production of ^{11}B is studied in the context of the ν-process. The core of a collapsing star can reach a temperature of up to 10 GK. In the helium layer, in which most of the ^{11}B is produced as an outcome of the ν-process, the temperature ranges between 1 GK and 5 GK, see section 1.4. The energy distribution of particles in a gas is described by the Maxwell-Boltzman distribution. Depending on their energies ($\propto speed^2$), the two nuclei colliding have a certain probability to tunnel through the Coulomb barrier between them. The Maxwell-Boltzman distribution is maximum at $E = \frac{5T}{2}$. At low energy the probability to penetrate the Coulomb barrier drops dramatically.

The convolution of the Maxwell-Boltzman distribution and the probability to tunnel through the Coulomb barrier of the nuclei gives access to an energy range at which a given reaction is most likely to happen depending on the temperature of the astrophysical site. Assuming there is no resonance, this range of energy is called the Gamow window. The Gamow window is centered on the Gamow energy, E_0, with a certain width, Δ (Eq. 2.1 and Eq. 2.2, resp.).

$$E_0 = \left[\left(\frac{\pi}{\hbar} \right)^2 (Z_0 Z_1 e^2)^2 \left(\frac{m_0 m_1}{2(m_0 + m_1)} \right) (kT)^2 \right]^{1/3} \tag{2.1}$$

$$\Delta = \frac{4}{\sqrt{3}} \sqrt{E_0 kT} \tag{2.2}$$

where Z_0 is the nuclear charge number of the projectile, Z_1 the nuclear charge number of the target, $m_{0,1}$ are their masses, k is the Boltzmann constant, and T the temperature of the plasma. The Gamow Window is then $[E_0 - \frac{\Delta}{2}, E_0 + \frac{\Delta}{2}]$ in the center of mass.

At the temperatures available during the production of ^{11}B through the ν-process, the Gamow window for the reaction $^7Li + \alpha$ is between 0.4 MeV and 2.6 MeV in the center of mass frame, which corresponds to the energy window of both extreme temperatures considered, i.e. 5 GK when the ν-process starts in the helium layer and 1 GK when it reaches an end.

As will be presented below, the $^7Li(\alpha,\gamma)^{11}B$ cross section has several resonances in the energy range mentioned above. Narrow resonances in the Gamow window contribute significantly to the stellar reaction rate.

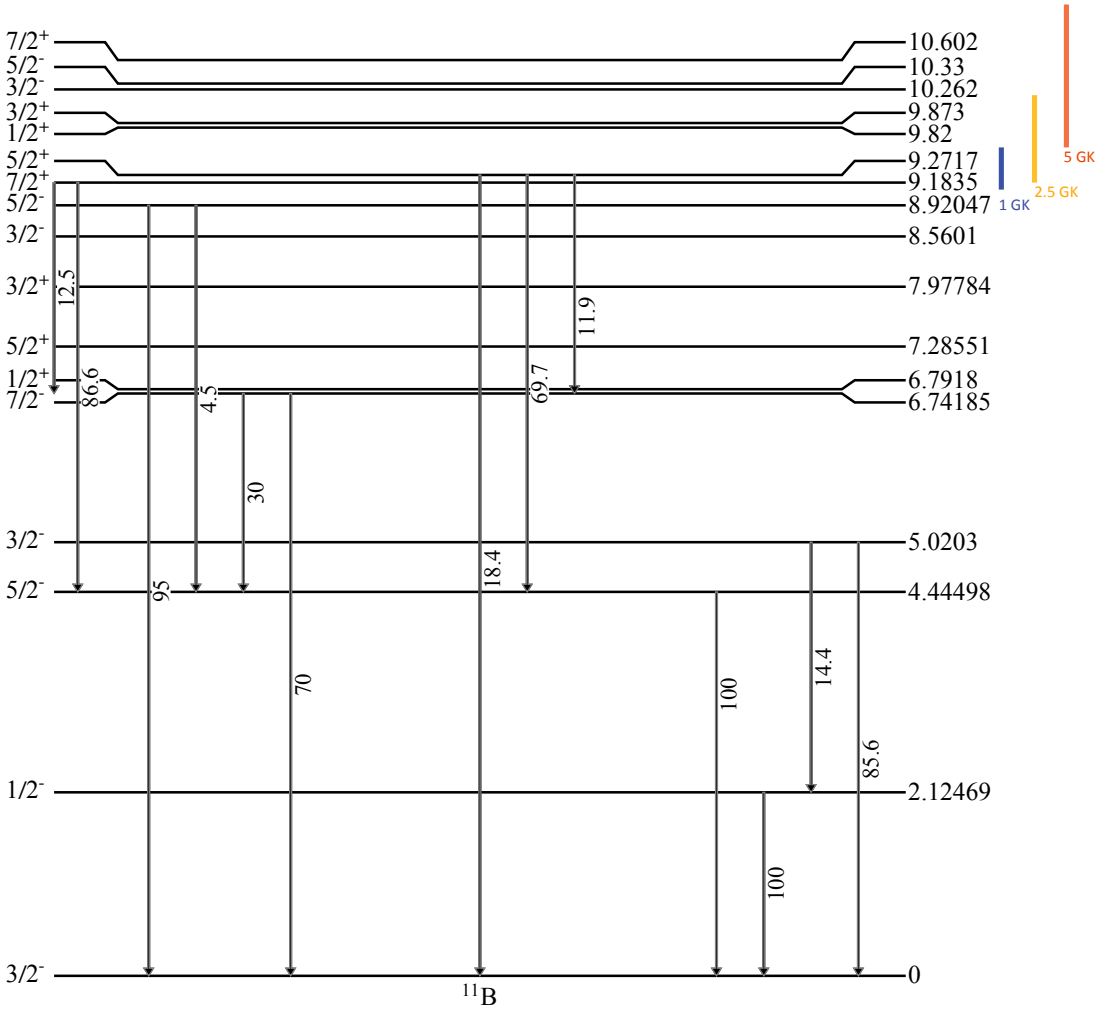

FIGURE 2.1: Level scheme of ^{11}B based on [42], the arrows represent the transitions between levels that have been measured. If known, the branching ratio is indicated. The colored lines on the side represent the Gamow windows at 1 GK in blue, 2.5 GK in orange, 5 GK in red.

In this chapter, the known properties of ^{11}B and the reaction $^{7}Li + \alpha$ at energies relevant to the ν-process are presented. The first section presents characteristics of ^{11}B up to $E_{ex} =$ 10.6 MeV. The second section will discuss what is known about the $^{7}Li + \alpha$ reaction.

2.1 Excited states in ^{11}B

The excited states in ^{11}B up to $E_{ex} = 10.6$ MeV, which is the upper end of the Gamow window, are presented in Fig. 2.1. The Gamow windows at 1 GK, 2.5 GK and 5 GK are depicted on the right side in blue, in orange and in red, respectively. The structure of ^{11}B has been studied through seven reactions, the breakup of ^{11}B [43], $^{10}B(d,p)^{11}B$ [44, 45, 46, 47], $^{12}C(e^-, e^- p)^{11}B$ [48], $^{11}B(p,p')^{11}B$ [47], $^{9}Be(^{3}He, p)^{11}B$ [49, 50] and its inverse, $^{11}B(p,^{3}He)^{9}Be$, [51]. The decay of ^{11}Be also gives access to states in ^{11}B [52]. The results of these studies, compiled in [42], provide a picture of ^{11}B. The energy of excited states, their spin and parity along with the total width of the state, if they are known, are presented below.

2.1.1 Excited state energies

The excited state energies of ^{11}B measured in the aforementioned articles and compiled in [42] are shown in Table 2.1 along with the beam energy in the laboratory frame and the center of mass frame for the states above the (α, γ) threshold. The reader is encouraged to use Table 2.1 to easily have access to the conversion between these quantities.

2.1.2 Spin and parity assignments

The spin and parity assignments that were studied in [1, 48, 49, 50, 52, 54, 55, 56] are presented in Table 2.2 and in Fig. 2.1 as they were used in the compilation [42]. All the assignments are in agreement.

The assignments by [49] were inferred from a distorted wave Born approximation (DWBA) analysis of their angular distribution measurement. The angular distribution measured for the different states between 9 MeV and 11 MeV are mostly in agreement with the DWBA calculation they performed. This allowed them to assign spin and parity, see Table 2.2.

E_{ex} (keV)	E^{lab}_{beam} (keV)	E_{cm} (keV)
10602	3043.1	1937.7
10330	2615.9	1665.7
10262	2509.2	1597.7
9873	1909.2	1215.7
9820	1815.0	1155.7
9271.7	953.9	607.4
9183.5	815.4	519.2
8920.47	402.3	256.1
8560.1		
7977.84		
7285.51		
6791.80		
6741.85		
5020.30		
4444.98		
2124.693		

TABLE 2.1: Table of energies of excited states in ^{11}B, from [42], with the beam energy required to reach them via $^{7}Li(\alpha,\gamma)^{11}B$ if they are above the threshold at 8664.31 keV (double line) in the laboratory frame and the center of mass frame based on the masses of [53].

2.2 The $^{7}Li + \alpha$ reaction

The known information about the $^{7}Li + \alpha$ exit channels below a beam energy of 3.1 MeV corresponding to an excitation energy of $E_{ex} = 10.63$ MeV in ^{11}B (Fig. 2.2) will be presented in this section. Measurements of the cross section of the $^{7}Li(\alpha,\gamma)^{11}B$ reaction [1, 4, 5, 36, 54, 56, 57, 58, 59] as well as the cross section of the (α,α) and (α,α') reactions [1, 55, 60, 61] will be discussed.

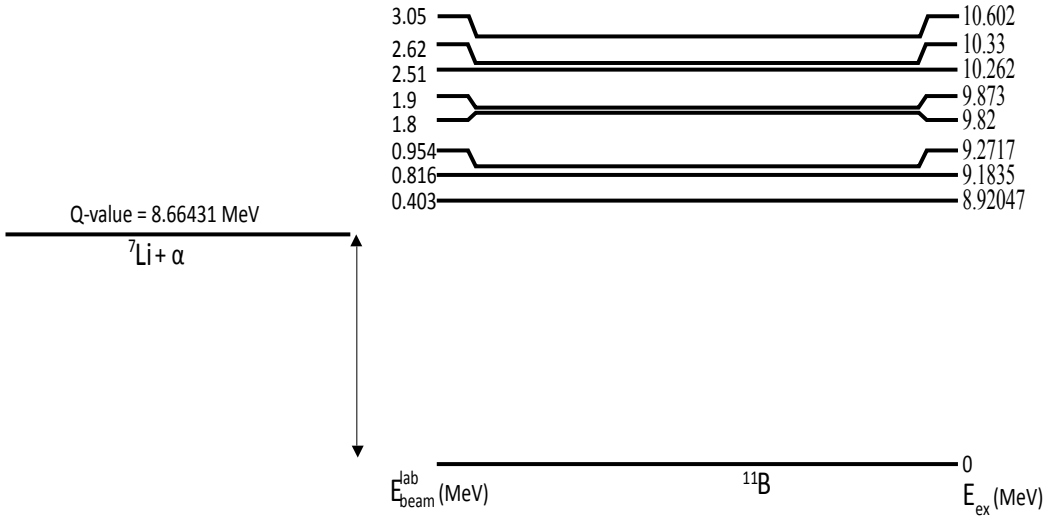

FIGURE 2.2: Scheme of $^{7}Li + \alpha$ in its relation to the nucleus of ^{11}B.

E_{ex} (keV)	Van Der Steenhoven[48]	Hinds[50]	Millener[52]	Green[54]
2124.693			$\frac{1}{2}^-$	
4444.82	$\frac{5}{2}^-$	$(\frac{1}{2}$ to $\frac{5}{2})^-$	$\frac{5}{2}^-$	$\frac{5}{2}^-$
5020.45		$(\frac{1}{2}$ to $\frac{5}{2})^-$	$\frac{3}{2}^-$	
6743.06	$\frac{7}{2}^-$	$(\frac{1}{2}$ to $\frac{9}{2})^-$		$\frac{7}{2}^-$
6791.87	$\frac{1}{2}^+$	$(\frac{1}{2}$ to $\frac{7}{2})^+$		
7285.55	$\frac{5}{2}^+$	$(\frac{1}{2}$ to $\frac{7}{2})^+$		
7977.87	$\frac{3}{2}^+$	$(\frac{1}{2}$ to $\frac{7}{2})^+$		
8560.07	$\frac{3}{2}^-$	$(\frac{1}{2}$ to $\frac{5}{2})^-$		
9820	$\frac{1}{2}^+$			

E_{ex} (keV)	Cusson[55]	Zwieglinski[49]	Paul[1]	Green[54]
8919.74		$\frac{5}{2}^-$		$\frac{5}{2}^-$
9185.68		$\frac{7}{2}^+$		$\frac{7}{2}^+$
9274.37		$\frac{5}{2}^+$		$\frac{5}{2}^+$
9873	$\frac{3}{2}^-$	$\frac{3}{2}^-$	$\frac{3}{2}^-$	
10263	$\frac{1}{2}^\pm$ or $\frac{3}{2}^\pm$	$\frac{3}{2}^-$	$\frac{1}{2}^\pm$ or $\frac{3}{2}^\pm$	
10332	$\frac{5}{2}^-$ or $\frac{7}{2}^-$	$\frac{5}{2}^-$	$\frac{5}{2}^-$ or $\frac{7}{2}^-$	
10604.27	$\frac{5}{2}^+$ or $\frac{7}{2}^+$	$\frac{7}{2}^+$		

TABLE 2.2: Table of the spin and parity assignments of excited states in ^{11}B.

2.2.1 (α, α) and (α, α')

Li and Sherr [61] measured the cross section of the (α, α') reaction and found 3 resonances by measuring the γ-rays coming from the first excited states of ^7Li at $E_{ex} = 478$ keV with a NaI scintillator. They found a cross section of 0.11± 0.02 barn at 1.21 MeV and a cross section of 0.08 ±0.015 barn at 1.59 MeV (affected by constructive interaction with the resonance at 1.21 MeV).

Bichsel and Bonner [60] studied the (α, α') reaction measuring the γ-rays coming from the first excited state of ^7Li with a NaI scintillator. They found resonances at $E_{cm} = 1.21$ MeV, 1.59 MeV and 1.95 MeV in agreement with Li and Sherr [61].

Cusson [55] measured the cross section of the (α, α) and the (α, α') reactions at the same energies, the cross sections are scaled on the measurement of Li and Sherr [61]. They also measured the angular distribution. They used the R-matrix theory to extract the resonance parameters, including the spins and parities and the total widths. They report the following excited state energies (found with masses available in 1966) $E_{ex} = 9.88 \pm 0.02$ MeV, $E_{ex} = 10.25 \pm 0.035$ MeV, $E_{ex} = 10.34 \pm 0.02$ MeV, $E_{ex} = 10.60 \pm 0.006$ MeV each associated with the total widths of 0.13 ± 0.03 MeV, 0.15 ± 0.04 MeV, 0.080 ± 0.03 MeV and 0.70 ± 0.01 MeV, respectively.

Table 2.3 shows the total widths of the states measured by Zwiegliński et al. [49] and Cusson [55] at E_{ex} = 9873 keV, E_{ex} = 10262 keV, E_{ex} = 10330 keV and E_{ex} = 10602 keV. Their measurements are used to determine the total widths of the three first excited states where the measurements of [49] and [55] agree within uncertainties.

However, the total width of the state at E_{ex} = 10602 keV as measured by Zwiegliński et al. [49] and Cusson [55] are in disagreement. The discrepancy might come from the poor energy resolution on both measurements (40 keV for Cusson and 80 keV for Zwieglinski). They both had issues with their target (carbon build up for [49] and stability for [55]).

E_{ex} (keV)	Γ (keV) [55]	Γ (keV) [49]	Γ (keV) [1]
9873	130 ± 30	104 ± 15	290
10263	150 ± 40	168 ± 25	433
10330	80 ± 30	123 ± 20	100
10602	70 ± 10	122 ± 20	90

TABLE 2.3: Excited state energies and total widths of states between 9.88 and 10.6 MeV. From Paul et al. [1], Zwiegliński et al. [49] and Cusson [55].

Paul et al. [1] also studied the (α, α') reaction along with the (α, γ) reaction and found the same resonances, as found by other measurements. Like Cusson [55], they scaled their cross sections on Li and Sherr [61]. The R-matrix analysis performed by Paul et al. [1] and Cusson [55] are in disagreement. It is puzzling that the results of [1] and [55] do not seem to agree since they both scaled their (α, α') measurement on the work of Li and Sherr [61]. Part of the disagreement here is probably due to the (α, γ) measurement of Paul et al. [1] which is overestimated, see section 2.2.2.2.

A measurement in inverse kinematics was performed by Yamaguchi et al. [59] between E_{ex} = 10.24 MeV and E_{ex} = 13.3 MeV. They used an extended gas target and detected charged particles with a silicon detector and γ-rays with an array of 6 NaI(Tl) detectors. They measured the (α, α) and (α, α') reactions. They found levels at E_{ex} = 10262 ± 8 keV, E_{ex} = 10330 ± 8 keV, E_{ex} = 10602 ± 4 keV (no error specified), E_{ex} = 10960 ± 50 keV, E_{ex} = 11272 ± 14 keV, E_{ex} = 12554 ± 13 keV and E_{ex} = 13137 ± 40 keV.

Yamaguchi et al. [59] used the R-matrix theory to deduce Γ_α for the excited states at E_{ex} = 10262 ± 8 keV and E_{ex} = 10330 ± 8 keV of 4 keV and 19 ± 4 keV respectively. Yamaguchi et al. [59] also extracted the reduced width, γ_α^2, see section 4.2.3.1. Their reduced width γ_α^2 of 0.089 MeV can be compared with γ_α^2 = 0.227 MeV found by Paul et al. [1]. This discrepancy most likely also comes from the (α, γ) measurement of Paul et al. being overestimated.

2.2.2 $^7Li(\alpha,\gamma)^{11}B$

The $^7Li(\alpha,\gamma)^{11}B$ reaction has been extensively studied at low energy in the past. The Q-value of this reaction is Q= 8664.31 ± 0.38 keV, using the masses from [53]. The low lying resonances which are well known will be presented. After that, two measurements at higher energy will be discussed.

2.2.2.1 Low lying resonances

The (α,γ) reaction provides access to three low-lying resonances of ^{11}B which were studied numerous times [5, 36, 54, 56, 57, 58]. These resonances correspond to beam energies of E_{cm} = 0.26 MeV, E_{cm} = 0.52 MeV and E_{cm} = 0.61 MeV. The resonance strength of the highest of these three resonances was used in our experiment to measure the target thickness and to characterize the detector at energies relevant to our measurement.

Resonance at E_{cm} = 0.61 MeV

The resonance strength of the E_{cm} = 0.61 MeV resonance was measured by Green et al. [54], Jones et al. [56] and Hardie et al. [5] with values of 4.5 eV, 3.4 eV and 1.72 ± 0.17 eV, respectively. We adopt the value of Hardie et al. [5] of $\omega\gamma = 1.72 \pm 0.17$ eV because both [54] and [56] used NaI detectors while [5] used a Ge detector which makes it preferable due to the higher energy resolution inherent to a Ge detector. Furthermore a common contaminant, ^9Be, was seen in Green and Jones experiments; the (α,n) channel on ^9Be typically emits a γ-ray at 4438.91± 0.31 keV which can be easily confused with the strongest line, at 4444.98 ± 0.07 keV, in the resonance at E_{cm} = 0.61 MeV if the energy resolution is poor, see section 4.1.4.1.

Hardie et al. found the same channel width as Jones et al. of $\Gamma_\alpha = 4$ keV and a γ width of $\Gamma_\gamma = 1.15 \pm 0.16$ eV. Hardie et al. also measured the transition strength of the different transitions associated with this resonance. The transition strength for the resonance at E_{cm} = 0.61 MeV to the ground state (g.s.) is 0.73×10^{-3} W.u. and the transition strength to states at E_{ex} = 4445 keV and E_{ex} = 6741 keV are 22×10^{-3} W.u. and 23×10^{-3} W.u., respectively.

Resonance at E_{cm} = 0.52 MeV and E_{cm} = 0.26 MeV

Hardie et al. [5] give the strength of the two other low-lying resonances to be $8.8 \times 10^{-3} \pm 1.4 \times 10^{-3}$ eV for the resonance at E_{cm} = 0.26 MeV and 0.31 ± 0.05 eV for the one at

$E_{cm} = 0.52$ MeV. A measurement of the strength of the resonance at 0.52 MeV was also made by Gyürky et al. [58]. Their measurement agrees with Hardie et al. [5]. Gyürky et al. [58] measured $\omega\gamma = 0.3 \pm 0.032$ eV which, using a weighted average, yields a strength for the resonance at $E_{cm} = 0.52$ MeV of 0.303 ± 0.026 eV.

Hardie et al. [5], Green et al. [54] and Jones et al. [56] also give branching ratios for the transition in these resonances, see Table 2.4. The branching ratios from these three measurements are in a good agreement.

The transition strength of the $E_{cm} = 0.52$ MeV resonance was calculated by Hardie et al. [5]. The transition strength for this resonance to the states at $E_{ex} = 6741$ keV, at $E_{ex} = 4444.98$ and to the ground state are, respectively, 2.8×10^{-3} W.u., 4.2×10^{-3} W.u. and 0.17 W.u.

Transition	Jones et al. [56] (%)	Green et al. [54] (%)	Hardie et al. [5] (%)	Paul et al. [1](%)
$8930 \rightarrow g.s$	95	93 ± 5		
$\rightarrow 4.5$	5	2.3 ± 1		
$\rightarrow 6.7$	5	4.6 ± 2		
$9185 \rightarrow g.s$	0	0.9 ± 0.3	<1	
$\rightarrow 4.5$	91	82.8 ± 2	89.3	
$\rightarrow 6.7$	9	12.8 ± 0.4	8.2	
$9271 \rightarrow g.s$	16	19.7 ± 1	17.1	20
$\rightarrow 4.5$	70	67.5 ± 2	71.7	67
$\rightarrow 6.7$	14	12.8 ± 0.7	11.2	13

TABLE 2.4: Branching ratios in the low-lying resonances.

The branching ratios of the resonances are reported in Table 2.4 and can be seen in Fig. 2.1, using the compilation [42]. No branching ratio above 9271 keV is known.

2.2.2.2 Measurement of the (α, γ) cross section

The $^7Li(\alpha,\gamma)^{11}B$ cross section was measured twice between $E_{cm} = 0.64$ MeV and $E_{cm} = 1.91$ MeV by Paul, Puttaswamy, and Kohler [1], and by Heydenburg and Temmer [4].

Heydenburg and Temmer [4] measured the $^7Li(\alpha,\gamma)^{11}B$ cross section looking specifically for γ-rays of energies above 4 MeV with a NaI scintillator. They report not detecting any resonances after the one at $E_{ex} = 9271.7$ keV.

Paul et al. [1] studied $^7Li + \alpha$ and measured the differential cross section for 2 channels between beam energies of 0.83 MeV and 2.04 MeV in the center of mass. They measured the γ-rays with a NaI(Tl) detector. They were not able to measure any γ energies between 2 MeV and 7 MeV due to (α, n) reactions on target contaminants, mainly carbon and

oxygen. In order to find the characteristics of each state, they performed an R-matrix fit with several free parameters (resonance energy, γ width, the reduced particle width for each angular momentum and each level).

According to Paul et al. [1], the only spin that gives a good fit for the resonance at $E_{cm} = 1.21$ MeV is $J^\pi = \frac{3}{2}^+$. They find a total width of 433 keV for the resonance at $E_{cm} = 1.59$ MeV. They also provide the only differential cross section (at 90°) measurement shown in Fig. 2.3, in which four excited states are identified with arrows at 9.87 MeV, 10.26 MeV, 10.32 MeV and 10.61 MeV. In order to understand fully their differential cross section and fit it, they had to add a state at $E_{ex} = 10.45$ MeV which they said remains unexplained.

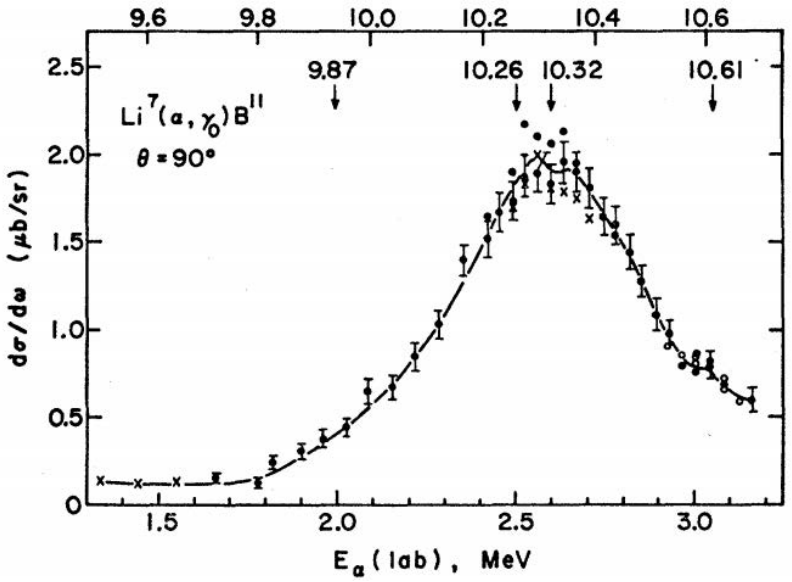

FIGURE 2.3: Differential cross section of $^7Li(\alpha,\gamma)^{11}B$ between $E_\alpha^{lab} = 1.3$ MeV and 3.2 MeV at 90° [1]. The different symbols represent different target-spot position and the arrows indicate previously reported states.

This differential cross section is overestimated. Indeed, the differential cross section measured by Paul et al. [1] is scaled to the cross section of the $E_{cm} = 0.61$ MeV resonance of Jones et al. [56].

Jones et al. [56] found a resonance strength of $\omega\gamma = 3.4$ eV, which is twice as large as the best measurement by Hardie et al. [5] of $\omega\gamma = 1.72$ eV. The Jones et al. [56] measurement agrees with the measurement of Bennett et al. [57], which suggests that the overestimation, in both cases, comes from an overestimation of their detector efficiency at high energy. Bennett et al. [57] explained that they correct the high energy peak (at $E_{ex} = 9272$ keV) for an averaged efficiency at ~ 5 MeV which is going to be much higher than the photopeak efficiency at 9 MeV they were using it for. In Fig. 2.4, we can see the impact of this overestimation on the differential cross section.

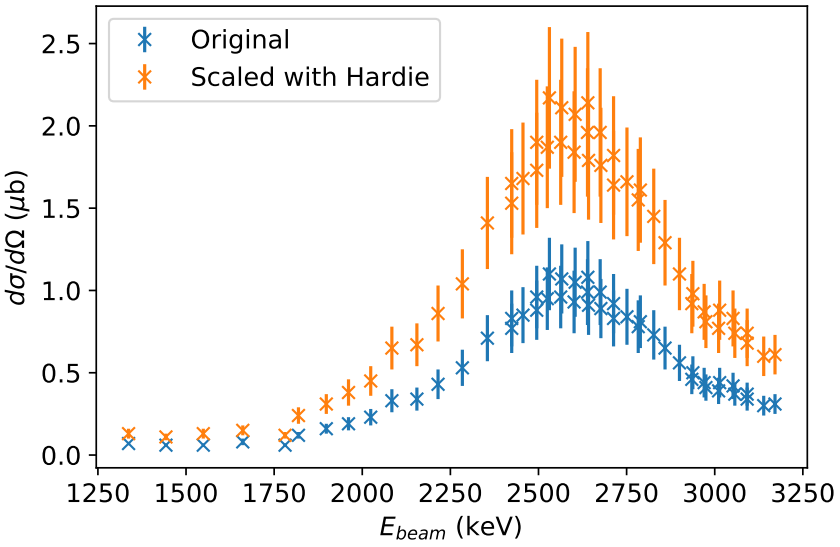

FIGURE 2.4: Differential cross section of $^{7}Li(\alpha,\gamma)^{11}B$ between $E_{cm} = 0.83$ MeV and 2.04 MeV at 90° [1]. Paul et al. [1] used the resonance strength from [56] to calculate their cross sections, shown as orange crosses. The blue crosses show the same cross sections scaled with the new resonance strength measured by [5].

The error bars on the Paul et al. [1] measurement are ± 25% at the "peak cross section". They assumed the cross section to be constant over the target thickness, therefore, they used a thin target approximation to correct their yields from target effects.

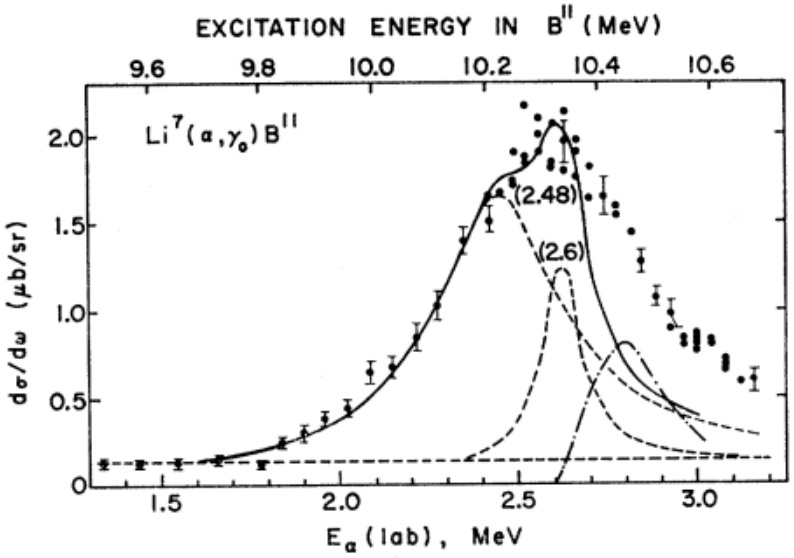

FIGURE 2.5: R-matrix fit from [1]. The plain line is the fit. The contributions of each resonance are represented with dashed line. The dot-dashed line represents the excess yield.

Their R-matrix fit is not really good, see Fig. 2.5 which correspond to Fig. 9 in [1]. The differential cross section for $^{7}Li(\alpha,\gamma)^{11}B$ is much broader than their fit. They added a

state at 10.45 MeV to help explain the shape of their differential cross section but it did not make up for the difference in shape.

2.2.2.3 Transition strength

No other transition than the resonance to ground state transition has been observed so far for the resonances above E_{cm}=1.21 MeV. One way to estimate whether another transition is possible from the resonance via an excited states is to calculate the transition strength. The transition strength, $\frac{\Gamma}{\Gamma_W} \times Br$, where Br is the branching ratio, can be estimated using the state width measured, Γ and the single particle width estimated by Weisskopf, Γ_W.

The two dominant transitions in ^{11}B from the resonances to the states at 5.02 MeV, 4.445 MeV and to the ground state are either E1 or M1. Weisskopf provides for each transition an estimate:

- $\Gamma_W = 6.75 \times 10^{-8} \times A^{2/3} E_\gamma^3$ for an E1 transition
- $\Gamma_W = 2.07 \times 10^{-8} \times E_\gamma^3$ for a M1 transition

where A is the mass number of a nucleus and E_γ the energy of the γ-ray emitted.

The state widths given in Table 2.3 allow us to estimate the transition strength for the higher resonances at E_{cm} = 1.21 MeV, E_{cm} = 1.59 MeV and E_{cm} = 1.66 MeV. The branching ratios of the transitions from these resonances to the states at E_{ex} = 4444.98 keV and E_{ex} = 5020.3 keV are unknown so far.

Resonance (MeV)	Res→5020 keV	Res→4445 keV	Res→g.s
1.21	12.2 w.u (M1)	2.0 w.u (M1)	4.8 w.u (M1)
1.59	54.6 w.u (M1)	40 w.u (M1)	7.3 w.u (M1)
1.66	35.2 w.u (E1)	25.9 w.u (E1)	0.3 w.u (E1)

TABLE 2.5: Transition strength estimation for the three resonances at E_{cm} = 1.21 MeV, 1.59 MeV and 1.66 MeV, assuming a branching ratio of 1. In parenthesis is the transition multipolarity.

The values found in Table 2.5 show that we should observe other transitions than the one to the ground state for these resonances. The transition strength to the excited states at E_{ex} = 4444.98 keV and E_{ex} = 5020.31 keV are larger than the transition strength to the ground state. The branching ratios for these two transitions (to E_{ex} = 4444.98 keV and E_{ex} = 5020.31 keV) would have to be zero for neither of these cascade to be happening.

Since the transitions to the ground state have been measured [1], it is likely to detect one of these transitions.

2.2.2.4 Theoretical S-Factor

The astrophysical S-Factor is the cross section corrected for the s-wave Coulomb barrier transmission probability defined by:

$$S(E) = \sigma(E)Ee^{2\pi\eta} \tag{2.3}$$

where η is the Sommerfeld parameter defined as $\eta = \frac{Z_1 Z_2 e^2}{\hbar v}$ where Z_1 and Z_2 are the atomic numbers of the projectile and target nuclei, e is the elementary charge, $\hbar$ is the reduced Plank constant and v the relative speed between the target and the projectile. There are two theoretical estimations available for the S-Factor of $^7Li(\alpha,\gamma)^{11}B$ [3, 62]. The two theoretical estimations highlight which resonance will have an impact on the S-Factor, hence on the reaction rate.

Descouvemont [62] used the Generator Coordinate Method (GCM) to produce the $^7Li(\alpha,\gamma)^{11}B$ S-Factor. He was interested in Big Bang Nucleosynthesis which occurs at a temperature below 1 GK. The GCM is a microscopic model which uses a harmonic oscillator model assuming an α cluster in ^{11}B. The GCM generates two functions with parameters assuming two different cluster couplings ($^7Li + \alpha$ and $^8Be +^3 H$). These two generated functions will feed later into the wave function. The GCM has fixed parameters for the partial wave, which are the spin, parity and the relative angular momentum of the cluster.

Descouvemont [62] then used a microscopic R-matrix framework (coupling of the GCM and the R-matrix theory) to calculate bound states as well as resonant and scattering wave functions.

According to his paper, he generated a level scheme in fairly good agreement with the experimental one. He inferred as well the $^7Li(\alpha,\gamma)^{11}B$ S-Factor, see Fig. 2.6.

It is clear that the S-Factor calculated by Descouvemont [62] is dominated by the $E_{ex} =$ 9271 keV contribution (peak on the right) at low energy and at higher energies the $E_{cm} =$ 1.21 MeV resonance seems to dominate. However, none of the strong high-energy resonance contributions are represented here, Fig. 2.6. Indeed, the $J_i = 3/2^+$ state corresponds to

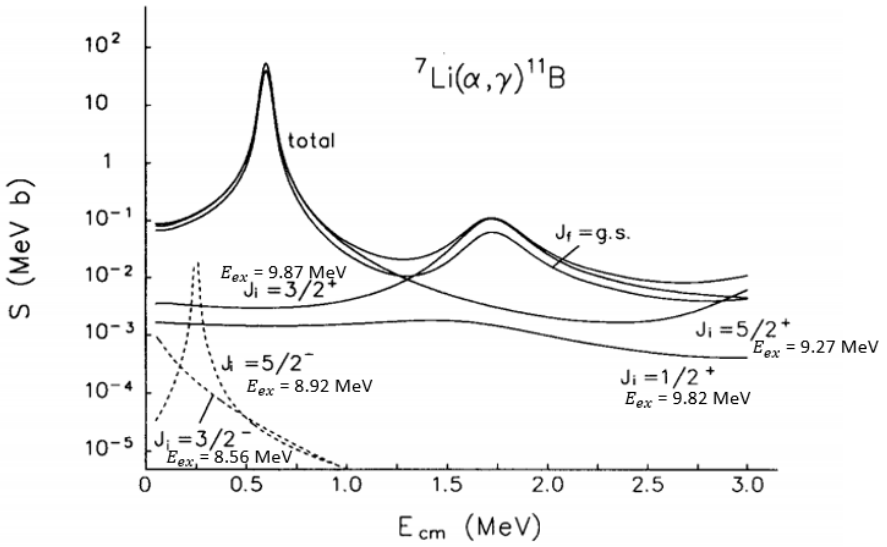

FIGURE 2.6: Modified from [62]. S-Factor of $^7Li(\alpha,\gamma)^{11}B$ between $E_\alpha = 0$ MeV and 3 MeV in the center of mass frame. The excited states corresponding to the spin and parity on the original figure were added for clarity.

the resonance at $E_{cm} = 1.21$ MeV. The resonances at $E_{cm} = 1.59$ MeV and $E_{cm} = 1.66$ MeV were not used because they were beyond the scope of this paper.

Another attempt to calculate the S-Factor was made by Xu et al. [3] using a potential model (Fig. 2.7). To calculate the S-Factor, they performed a fit of the existing resonances in $^7Li(\alpha,\gamma)^{11}B$ at 0.607 MeV, 1.6 MeV, 1.66 MeV and 1.93 MeV and then varied the parameters of their potential (Wood-Saxon + imaginary surface absorption) in order to match the measured parameters. They then applied a transition matrix to the initial state to obtain the final states. Xu et al. [3] assumed an uncertainty of ∼25% on the S-Factor.

Xu et al. [3] declared that no cross sections were available for this reaction and used the resonance strength provided by Paul et al. [1], Hardie et al. [5] and Gyürky et al. [58] for the excited states between 8.9 MeV and 10.6 MeV to constrain their model.

2.3 Summary

In this chapter, the information relevant to calculating the cross section of $^7Li(\alpha,\gamma)^{11}B$ was presented such as the excited state energies, spins and parities. This information will be vital to constrain the R-matrix analysis.

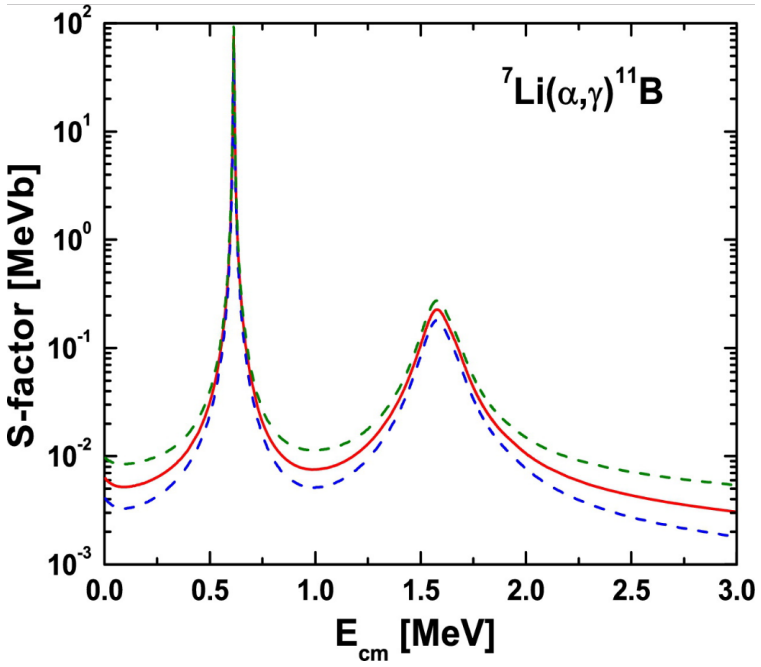

FIGURE 2.7: From [3]. S-Factor of $^7Li(\alpha,\gamma)^{11}B$ between $E_\alpha = 0$ MeV and 3 MeV in the center of mass frame (solid line). The dashed lines correspond to the uncertainties on the S-Factor.

The $^7Li(\alpha,\alpha')$ reaction cross section measurement and angular distribution of Cusson [55] will not be used because of their disagreement with the two other cross section measurement of Paul et al. [1] and Bichsel and Bonner [60].

The low-lying resonances were also investigated. They will be used as references to probe the targets. The resonance strengths of the low-energy resonances are also important to the final goal of this thesis which is to calculate the reaction rate between 1 GK and 5 GK. The resonance strength measurements of Hardie et al. [5] and Gyürky et al. [58] will be used because they are more precise than the measurements of Green et al. [54] and Jones et al. [56].

The differential cross section measurement of the $^7Li(\alpha,\gamma)^{11}B$ reaction at 90° made by Paul et al. [1] was reviewed and corrected.

It was shown using the Weisskopf estimate that, even though no γ cascade was observed between the resonances at $E_{cm} = 1.21$ MeV and 1.91 MeV, one or two cascades could be expected through the excited states at $E_{ex} = 4444.98$ keV and $E_{ex} = 5020.31$ keV.

Chapter 3

Setup & Characterization

The experiment to measure the $^{7}Li(\alpha,\gamma)^{11}B$ cross section took place at the Nuclear Science Laboratory (NSL) at the University of Notre Dame. As pointed out in Chapter 2, previous measurements did not observe all the possible cascades in this reaction.

In this chapter, the facility in which the experiment was performed will be presented. Additionally, details about the experimental setup, addressing the challenges of measuring the $^{7}Li(\alpha,\gamma)^{11}B$ reaction differential cross section, and the characterization of the setup minimizing systematic effects related to the setup will be discussed.

3.1 The Sta. Ana accelerator at the NSL facility at the University of Notre Dame

The NSL's core research is nuclear structure and nuclear astrophysics with three electrostatic accelerators, a 5 MV single ended and 10 MV Tandem accelerator (1 & 2, resp. on Fig. 3.1) at Notre Dame and another Tandem electrostatic accelerator of 1 MV, CASPAR, located 1.5 km underground at the Sandford underground research facility (SURF). A program of applied physics has recently started with the acquisition of a fourth electrostatic accelerator, a 3 MV Tandem (3 on Fig. 3.1).

The 10 MV Tandem has a multipurpose beamline with a large scattering chamber called R2D2 used among other things to measure the angular distribution of charged particle from nuclear reaction or scattering. The line is also used to perform total absorption spectroscopy measurements (c on Fig. 3.1). Another beam line is used by the accelerator mass

spectrometry group, it is one way to separate isobars using a Browne-Buechner spectograph (AMS - d on Fig. 3.1). The TwinSol beam line was the first facility to produce a radioactive beam in the United States. It uses a light stable beam (A $<$ 30) bombarding a target to produce a radioactive beam. The reaction products, aka the radioactive beam, are then separated with the 2 solenoids (e on Fig. 3.1). TwinSol is also used to measure the life time of unstable nuclei such as ^{11}C [63].

The 5 MV single ended electrostatic accelerator - Sta. Ana - (1 on Fig. 3.1) has three beam lines which are presented in a more detailed schematic in Fig. 3.5. The RHINOCEROS [64] beam line with an extended gas target (a on Fig. 3.1). RHINO was recently refurbished and recommissioned with the measurement of the $^{20}Ne(p,\gamma)^{21}Na$ cross section [65]. The second beam line feeds the St. George recoil mass separator, b on Fig. 3.1. St. George is designed to study (α,γ) reactions in inverse kinematics using 6 dipole magnets and a Wien filter. St. George is dedicated to separating the beam from the recoils produced when the heavy ion beam hits the lighter helium target. The commissioning of St. George started with measuring its energy acceptance [66] and is still under way with measuring the angular and energy acceptance as well as the mass rejection.

The last beam line on Sta. Ana is called the solid target line. It is a multipurpose beam line used exclusively with solid targets (blue on Fig. 3.5). This beam line was used during the experiment to study the $^{7}Li(\alpha,\gamma)^{11}B$ reaction.

In this section, the solid target line used to perform the $^{7}Li(\alpha,\gamma)^{11}B$ cross section measurement and the setup around the solid target line will be presented and characterized. Sta. Ana, the accelerator used to perform the measurement, will be introduced followed by the beam line used, the setup and the data acquisition system, and finally, the system characterization will be presented. The procedures and results of the target characterization will be discussed, the techniques used to determine the detector calibration and efficiency will be described along with the results. Finally, the beam energy calibration process will be described and presented.

3.1.1 Sta. Ana: Stable ion accelerator for Nuclear Astrophysics

Sta. Ana is a 5 MV single ended vertical electrostatic accelerator (see Fig. 3.2). The left side of Fig. 3.2 presents the accelerator in the vertical plane while on the right side of the analyzing magnet, the accelerator main beam line is in the horizontal plane.

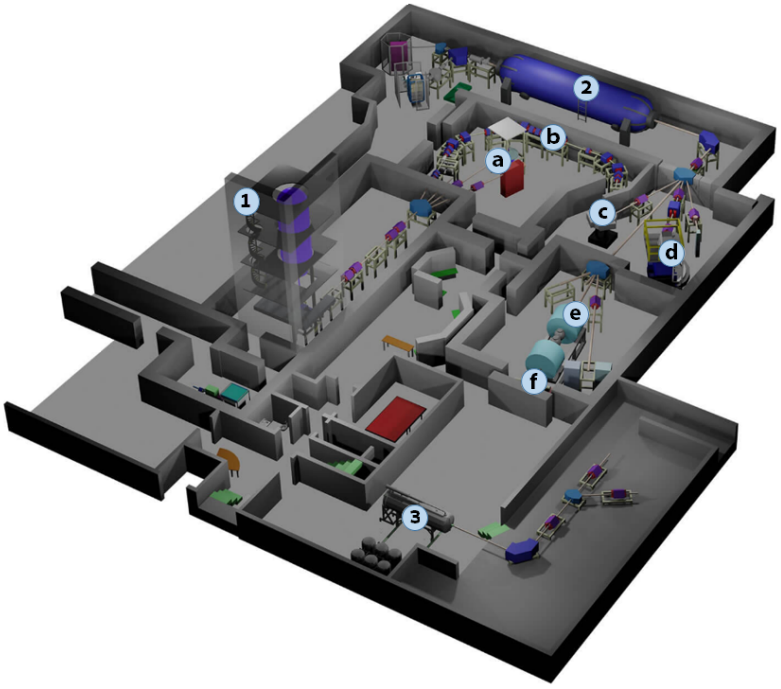

FIGURE 3.1: Layout of the NSL. The numbers represent the three accelerators and the letters represent the different experimental beam lines available for experiments, see text for details.

Ions are accelerated with a static high voltage. Sta. Ana possesses an electron cyclotron resonance ion source (ECRIS) in the terminal shell [67] (top of the accelerator above the acceleration sections). In the ECRIS, gas - containing the element planned to be used as beam - is injected and its electrons are stripped off using a radio frequency power supply to make a plasma. The plasma is also contained in the ion source, only charged particle with the right energy can escape the containment. Two electrostatic plates (the extractor) push the beam out of the source. The ions are extracted from the source, focused and accelerated.

The ion source is placed at a higher potential than the terminal to provide a first acceleration of the produced ions out of the source and toward the acceleration column. The terminal itself is at a potential +TV (terminal voltage), relative to the laboratory ground, corresponding to the desired energy, divided by the charge state of the beam. The potential difference between the terminal shell and ground is responsible for the acceleration of the beam. Resistors along the acceleration section smoothly decrease the electric field, making the acceleration smooth. The metallic hoops connected in series with the resistors along the acceleration sections provide a uniform field by moving the fringe fields away from the center of the beam line, the metallic hoops for three acceleration section are visible in Fig. 3.3. When the beam is accelerated, it takes charge away from the system, electrons

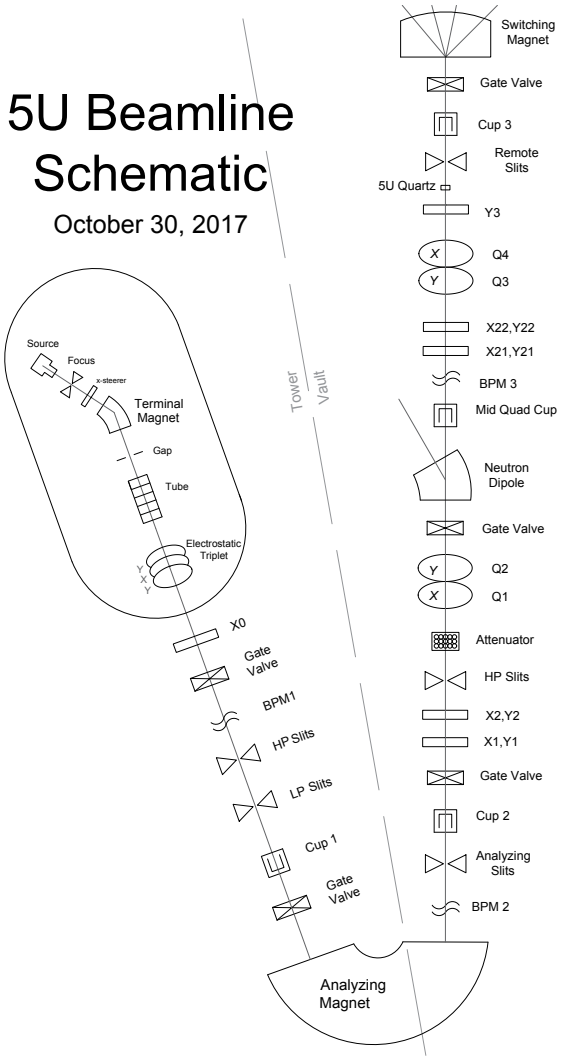

FIGURE 3.2: Schematic of the Sta. Ana vertical accelerator and the horizontal main beam line associated to this accelerator joined by an analyzing/bending magnet.

stripped off of the extracted ions in the ion source will neutralize some of the positive charge maintaining the terminal at the desired voltage, hence, creating a charge deficit requiring additional charge to be added to maintain the terminal voltage. The charge needed to maintain the terminal voltage is provided by a Pelletron charging system, see Fig. 3.4.

To provide the charge needed, Sta. Ana has four chains each using the Pelletron charging system, Fig. 3.4. The Pelletron charging system has two inductors and two suppressors. The inductor at the bottom of the accelerator is negative so the positive charge stays on the chains while the negative charges are pushed toward the ground, thus, the chains are positively charged. The inductor in the terminal shell is positive to push the positive charge to the terminal. The suppressors purpose is to ground the chains.

FIGURE 3.3: View of the 3 acceleration sections at the bottom of the accelerator inside the Sta. Ana accelerator tank.

For the experiment discussed in this work, $^4He^+$ was selected at the exit of the ECRIS using the dipole magnet in the terminal. In addition to the dipole in the terminal magnet, another dipole magnet, the analyzing magnet, contributes to selecting the beam species (the charge state and energy). The terminal magnet located in the terminal shell provides a first coarse selection of the charge state and the energy and the analyzing magnet which bends the beam from the vertical to the horizontal plane provides a fine selection of the beam species. The trajectory of the particles in these two dipole magnets is ruled by the following equations:

$$B\rho = \frac{p}{q} \tag{3.1}$$

where B is the magnetic field, ρ radius of the trajectory that a particle with a momentum p and a charge state q would follow. Along with the energy of the particles, E_p:

$$E_p = q(Extractor + TV) = \frac{1}{2} m_{beam} v^2 \tag{3.2}$$

where Extractor is the extractor voltage relative to the terminal, TV is the terminal voltage

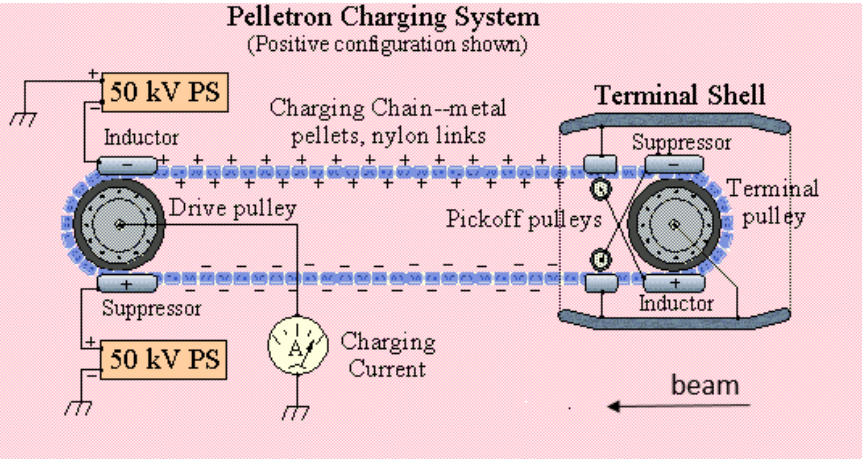

FIGURE 3.4: From National Electrostatic Corps. (NEC) website [68]. Schematic of the Pelletron charging system used to provide charge to the terminal. The beam direction from the terminal high voltage to ground is indicated by an arrow.

relative to the ground, m_{beam} the mass of the beam particle and v their speed. Together, the terminal magnet and the analyzing magnet provide a $\frac{m}{q}$ selection.

The terminal magnet allows for a rough selection of a particular mass over charge state. In our case, $\sim 4/1$. The analyzing magnet is more dispersive than the terminal magnet and makes another mass over charge selection. The analyzing magnet allows the selection of a beam with an energy resolution of 1 keV with a set of analyzing slits following the magnet with an opening of 1.5 mm.

The main beam line, following the analyzing magnet, is composed of 4 quadrupoles and 4 sets of vertical and horizontal steerer magnets. At the end of the main beam line, a switching magnet, seen in green in Fig. 3.2, allows the selection of the experimental beam line.

3.1.2 The solid target beam line

The beam line used to study the $^7Li(\alpha,\gamma)^{11}B$ reaction, the solid target line, in blue in Fig. 3.5, possesses two additional quadrupole magnets and a set of horizontal and vertical steering magnets.

The target, located at the end of the beam line, is made of a lithium compound deposited on a thick metallic backing by evaporation, see section 3.3.1 for details. The backing also serves as a beam stop. This backing is the interface between the vacuum in the beam line and the atmosphere. The end of the beam line is designed so that the target is mounted at a 45° angle relative to the beam. Inside the target chamber is a cold trap (a liquid

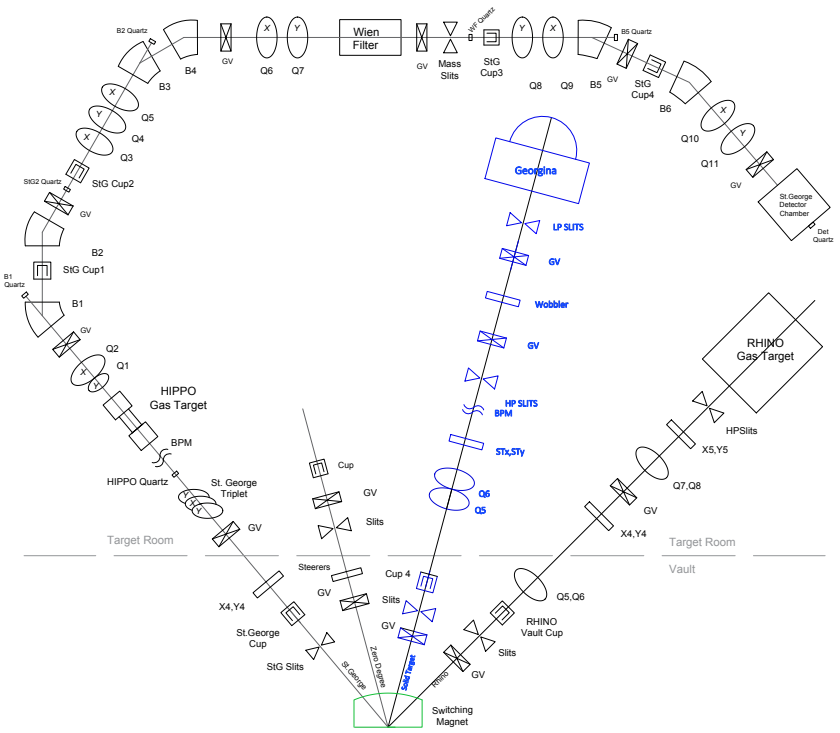

FIGURE 3.5: Schematic of the 5U beam lines. In green, the switching magnet is the link between the main beam line and the different target lines. In blue is the Solid Target line.

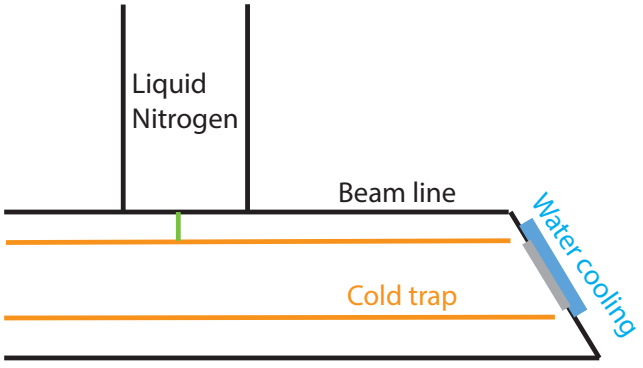

FIGURE 3.6: Cartoon of the cold trap at the end of the solid target line. The beam line is in black and inside, in orange is a copper pipe cooled down at liquid nitrogen temperature. In green is a piece of metal which links the liquid nitrogen tank to the copper pipe allowing the copper pipe to be cooled. This piece of metal also allows for the suppression voltage to be applied on the copper pipe. The water cooling is represented in blue at the end of the target chamber oriented at 45° relative to the beam direction below which is the target in grey also at 45°.

nitrogen cooled copper pipe, see Fig. 3.6) to prevent build up on the target, trapping gases and vapors by condensing them on the cold surface beforehand. Preventing build up on the target minimize the uncertainties on the energy of the beam when it interacts with the lithium target.

The beam intensity is measured on the target. To prevent the electrons created by the interaction of the beam with the target from escaping and creating a false reading of the beam intensity, a potential of -300V is applied to the cold trap copper tube.

A set of horizontal and vertical magnetic steerers called wobbler is used to wobble the beam across the target to cover entirely the target and to help dissipate the heat in the target. The wobbler's magnetic field is varied from zero to a maximum field at a fixed frequency to move the beam back and forth in the x and y axes, the technique is also called beam painting. A set of slits before the target chamber is used to make sure the beam is centered on the target and to tune the amplitude of the wobbling.

3.2 The setup and acquisition system

We used a single γ-ray detector oriented at 45° relative to the beam direction. It is a p-type high purity germanium (HPGe) detector with ∼120% relative efficiency (relative to the efficicency of a 3"×3" NaI detectors for 1332 keV γ-rays).

3.2.1 HPGe detector for γ-ray detection

HPGe detectors are semi conductor detectors. The gap between their valence band and conduction band is small, ∼3 eV, and the thermal energy at room temperature is enough for electrons to get from the valence band to the conduction band. The energy resolution of a semi-conductor is limited by the band gap, thus this small band gap is an interesting property. To limit the ability of electrons to randomly cross over the band gap at room temperature, germanium detectors are cooled down at liquid nitrogen temperature.

There are three ways for γ-rays to interact with matter.

- The photoelectric effect: the γ-ray will deposit all its energy onto an electron. The photoelectron carries the energy of the γ-ray minus its binding energy.
- The Compton effect: the γ-ray will only give part of its energy to an electron via scattering and it will give the rest to another electron, through one of the three possible way, or escape the detector.
- The pair creation: a γ-ray of energy greater than 1022 keV can create an electron positron pair in the vicinity of matter. After the pair creation effect, the positron

recombines and produces two γ-rays. It is possible for one or two of these γ-rays to escape. When only one 511 keV γ-ray escapes the detector, it creates a peak 511 keV lower then the photopeak (the single escape peak). When both γ-rays escape, they create a peak 1022 keV lower than the photopeak (double escape peak).

In this experiment, we will look at the photopeak which correspond to the total energy of the γ-ray detected. The photopeak originates principally from the photoelectric effect, it also can originate from the Compton effect and pair creation effect if all the γ-rays subsequent to these effects deposit their energy in the detector.

3.2.2 Detector orientation

We used the detector oriented at 45°, see Fig. 3.7, because the angular correlations are minimal at 55°, and our detector is large enough for 55° to be encompassed in its angular bite. The Doppler shift is also less consequent at 45° that it would be at 0°.

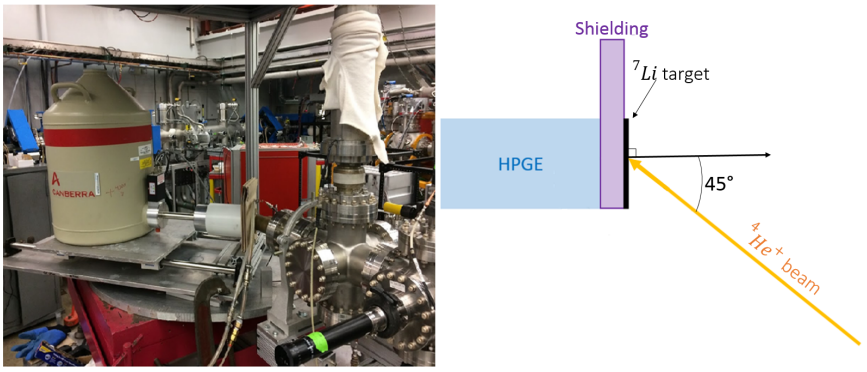

FIGURE 3.7: On the left is a picture of the setup. The left side of the pictures shows the detector and the shielding, on the right side, the end of the solid target line can be seen. On the right, a schematic of the same setup. The beam is coming from the right onto the target and the detector is oriented at 45°.

3.2.3 Shielding

Neutrons are known to damage germanium detectors by displacing the germanium atoms off of their crystalline structure which creates a charge trap and thus degrades the energy resolution of the detector. While we did not expect any neutron production from our experiment, nuclear reactions between the beam and the elements present in the target, on the slits or elsewhere could produce neutrons. For instance, $^{13}C(\alpha, n)$ is one of the most common sources of neutrons because of its large cross section, thus, as a precaution we had

an inch of polyethylene in front of the detector to reduce the potential neutron yield in the detector.

We also installed lead between the target and the detector. The lead is there to block part of the γ-rays coming from the $^7Li(\alpha,\alpha')$ reaction discussed in section 2.2. Limiting the number of 478 keV γ-rays from the $^7Li(\alpha,\alpha')$ reaction will limit dead time and pile-up due to this reaction. The attenuation of radiation through matter is governed by:

$$I = I_0 e^{-\alpha x} \tag{3.3}$$

where I_0 and I is the number of γ-rays emitted by the source and the number of γ-rays left after passing through the lead, respectively. α is the attenuation coefficient per mass density for lead and x is the thickness in cm of lead to cross. The value of α is the inverse ratio of the density of lead and the $\alpha = \mu/\rho$, where μ is the attenuation coefficient and ρ is the mass density, which can be found on the NIST website [69]. Using the attenuation formula, Eq. 3.3, we chose to use 1.905 cm (0.75 inch) of lead to block 97% of the γ-rays at 478 keV coming from the first excited state of ^7Li, see Table 3.1. This thickness

γ energy (MeV)	Percentage of γs going through 3/4" of lead
0.4	0.7
0.5	3.1
4	40.4
5	39.7
10	34.2

TABLE 3.1: Percentage of γ-ray going through 1.905 cm of lead shielding, using NIST attenuation coefficients, [69].

of lead also blocks 45% to 60% of γ-rays between 4 MeV and 11 MeV. The efficiency of the detector was measured with the lead shielding (and the aforementioned polyethylene shielding), therefore the γ-ray losses due to the shielding are accounted for in the analysis and especially it is included in the estimation of the detector efficiency.

3.2.4 Data Acquisition

The germanium detector is provided with a built-in pre-amplifier to link the detector which matches the high output impedance of the detector to the low input impedance of the amplifier. There is then an amplifier which will multiply the signal amplitude by the chosen gain. The gain is chosen to ensure that γ-rays with energies up to 11 MeV are properly detected.

The amplifier sends a signal to an analog to digital converter (ADC) which converts the amplitude of the electric signal into a binary number to be transmitted to the acquisition system. The ADC will assign a number between 0 and 8191 depending on the amplitude of the signal. We used the MPANT acquisition system [70], which is a multiple channel analysis software that reads and records the spectra in text files. The MPANT software can be used in LIST-mode but this was not used during our experiment as we had only one detection channel.

The current on target and on the cold trap, used to suppress secondary electrons, were read and recorded at all times in an independent system. In order to do that we used digital current integrators and digital counters. The charge was displayed on a program in multiples of 10^{-8} Coulomb/pulse.

3.3 Characterization of the setup

The results of the characterization of the setup presented above will be discussed in this section as well as the characterization of the targets. The setup encompasses the target, the detector and the beam. The target selection and behavior of the compound will be discussed as well as the target backings. The detector calibration and efficiency will be presented. The analyzing magnet calibration is also addressed here as it relates to the energy calibration in the detector.

3.3.1 Target characterization

The target is evaporated onto a thick backing, shown in Fig. 3.8, which will also serve as a beam stop. Because the beam is intense (several μA), a self supported target would be rapidly damaged by the power dissipated in the target. The damage associated with thick material bombarded with helium is a well known phenomenon called blistering [71] and is visible on Fig. 3.8. We can see the beam spot being only a 1 cm wide a 3 mm high. We considered a point like source in our analysis, a more rigorous approach would require simulations. To dissipate the heat, in addition to the wobblers, discussed in section 3.1.2, the backing is water cooled.

In general, two target compounds are used to produce lithium targets: LiF [5, 54, 55, 58] and metallic lithium [1, 55, 57, 61]. Metallic lithium, if exposed to air, will rapidly become

FIGURE 3.8: Picture of a target and its backing. In the middle, the blistering of the target can be seen. The target blistered while the wobblers were left off. The wobblers are elements that helps dissipate the heat.

LiOH because lithium is very hygroscopic (attracts water). Several authors mention having trouble with their ^{7}Li targets [1, 55, 57] which are either LiF or LiOH.

We used $^{7}Li^{16}OH$ as our target compound. It is the natural state of lithium once in atmosphere. We evaporated 99.99% enriched ^{7}Li and let water enriched at 99.99% in ^{16}O in the vaccum vessel. Enriched ^{16}O water was used because the (α, n) channel of ^{17}O has a positive Q-value of 0.56 MeV.

LiF is the most stable compound [72]. However, the (α, n) channel of ^{19}F opens close to 2 MeV (Q-value = -1952.33 keV). We tested the stability of our selected target compound, LiOH, against LiF to compare their stability under helium beam bombardment. We also compared two different backings, tantalum and molybdenum.

In the next sections, a method to study targets will be discussed as well as the comparison between the target compound and the selection process for the backing.

The purpose of this study is to answer the following questions:

- How many atoms of ^{7}Li are contained in the target as a function of time?
- How fast does ^{7}Li sputter from the target? How will the target evolve when put under high beam power?

3.3.1.1 Method

In order to characterize the targets, we measured the yield of a well known resonance in $^{7}Li(\alpha,\gamma)^{11}B$ and studied its excitation curve which displays the yield (number of γ-rays detected per incoming beam particle) as a function of the beam energy.

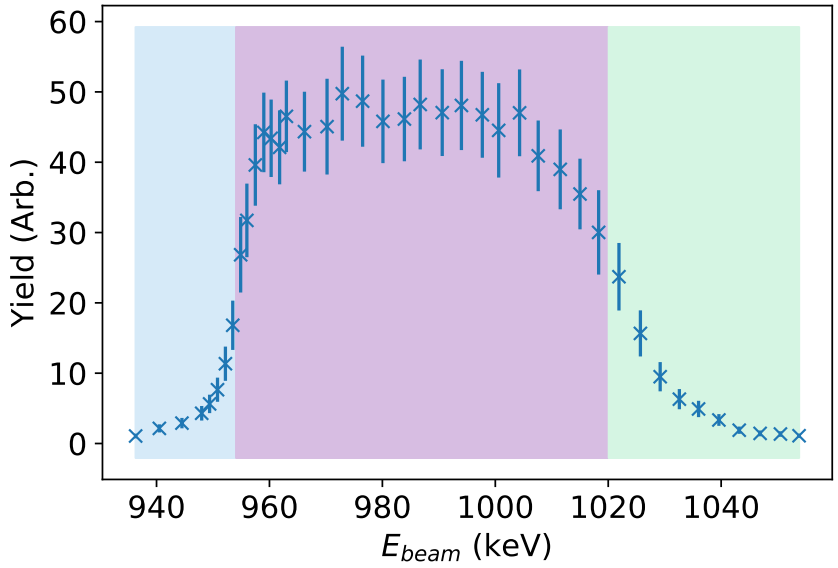

FIGURE 3.9: Resonance Scan -or Excitation Curve- of the resonance at 0.61 MeV (E_{lab} = 954 keV) in ^{11}B. The energy region shaded in blue contains information related to the resonance, the one shaded in purple and green provide information related to the target, see text for more details.

Fig. 3.9 presents a typical example of an excitation curve of the resonance in ^{11}B at E_{cm} = 0.61 MeV. It will be used to describe what can be seen in a typical resonance scan. We will use Fig. 3.10 to explain the behavior of the yield as a function of the beam energy (colored Gaussian) when scanning a resonance with a given width (thick black line).

We assume that the beam energy distribution is smaller than the resonance width. The yield in Fig. 3.9 starts increasing when the high end of the beam energy distribution reaches the low energy side of the resonance, this is represented by the blue Gaussian in Fig. 3.10 and the blue area in Fig. 3.9. As the beam energy increases, more of the beam energy overlaps with the resonance energy distribution and the yield increases. The front slope of the excitation curve contains the information about the resonance, its width and the energy resolution of the beam. The resonance energy can be found at 50% of the maximum yield, on Fig. 3.10, when the maximum of the energy distribution of the beam and the resonance width are overlapping, it corresponds to the purple Gaussian in Fig. 3.10 and purple area in Fig. 3.9.

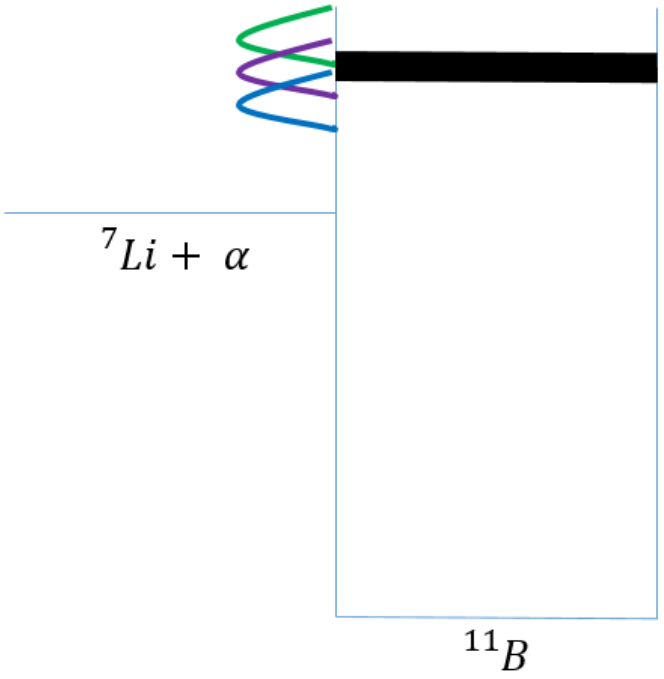

FIGURE 3.10: Schematic representing different beam energy Gaussian distributions relative to a resonance energy. The resonance and its width are in black and the three Gaussians on the side correspond with three beam energies (blue = lower than the resonance energy, purple = close to resonance energy and green = higher than the resonance energy). See text for detailed explanation.

A maximum of the beam ions either are at an energy within the resonance width or lose enough energy to be within the resonance width. As long as this is true, a maximum of beam ions are within the resonance width and the yield is the highest and presents a plateau if the target is thick enough.

Finally, as the beam energy increases more, green Gaussian in Fig. 3.10, the yield will fall off of the plateau, shown with the green area in Fig. 3.9. The high end of the beam energy distribution will not lose enough energy to fall within the resonance width. The target thickness in terms of energy loss is the full width at half maximum of the excitation curve. The slope of the decrease is affected by energy loss, straggling and target thickness inhomogeneity.

We can extract from the excitation curve the quantity of target atoms and follow its evolution over accumulated charge simply by scanning the resonance multiple times over the time of the experiment. The accumulated charge is the amount of beam particles sent on the target measured as a current integrated over time. For a constant beam intensity, the accumulated charge corresponds to the beam intensity multiplied by the time of

bombardment.

In the case of $^{7}Li(\alpha,\gamma)^{11}B$, we measure the evolution of the target over accumulated charge by scanning the resonance at $E_{cm} = 0.61$ MeV in ^{11}B several times. The two methods used in this work to extract the number of ^{7}Li atoms on target from the resonance scan will be explained below.

Method 1

The area under the resonance scan, similar to Fig. 3.9, is directly related to the number of lithium atoms in the target. These two quantities are related through the resonance strength:

$$A_\gamma = n \times \frac{\lambda_r^2}{2} \times \omega\gamma \tag{3.4}$$

where A_γ is the area under the yield, n the number of target atoms, λ_r the De Broglie wavelength of the resonance and $\omega\gamma$ is the resonance strength. To get the actual number of active nuclei n, the yield needs to be expressed as follow:

$$Y = \frac{\text{Counts in the } \gamma \text{ peak}}{\text{accumulated charge}} \times \frac{1}{\text{Detection efficiency}} \tag{3.5}$$

The accumulated charge is the amount of beam particles collected during the acquisition, and the yield is corrected for summing effects if necessary, see section 3.3.4.

The uncertainty on this method arises principally from the uncertainty on the area under the excitation curve (from the number of count in the γ-ray peak and the detection efficiency) and from the uncertainty on the resonance strength of the resonance at $E_{cm} = 0.61$ MeV which is of 10 %.

Method 2

The number of lithium atoms, n, can also be estimated from the target thickness in terms of energy loss in eV (ΔE) and the stopping power at the resonance energy in $eV.cm^2$ ($SP(E_r)$) from SRIM [73] with the following formula:

$$n = \frac{\Delta E}{SP(E_r)} \tag{3.6}$$

The target thickness in terms of energy loss can be deduced from excitation curves, such as the one on Fig. 3.9. The energy loss through the target is given by the full width at half maximum.

The uncertainty on this method comes from the uncertainty from the way the energy loss is determined: The precision with which the field is known (whithin one Gauss) and the quality of the energy calibration of the analyzing magnet. The uncertainty on the stopping power is of 20 % as recommended by [73].

The information extracted from the resonance scans, using method 1 and 2, will be used in the following sections to study the targets.

3.3.1.2 Target stability

In this section, we compare the LiOH target content to the one of the LiF target as a function of time, or accumulated charge. To quantify the behavior of the target under high power and to quantify the stability of LiOH and LiF we scanned the resonance several times and between each scan of the resonance, we tried to do more damage to the target by using a high intensity beam (above 15 μA) at higher energy (E_{cm} =$\sim$0.96 MeV).

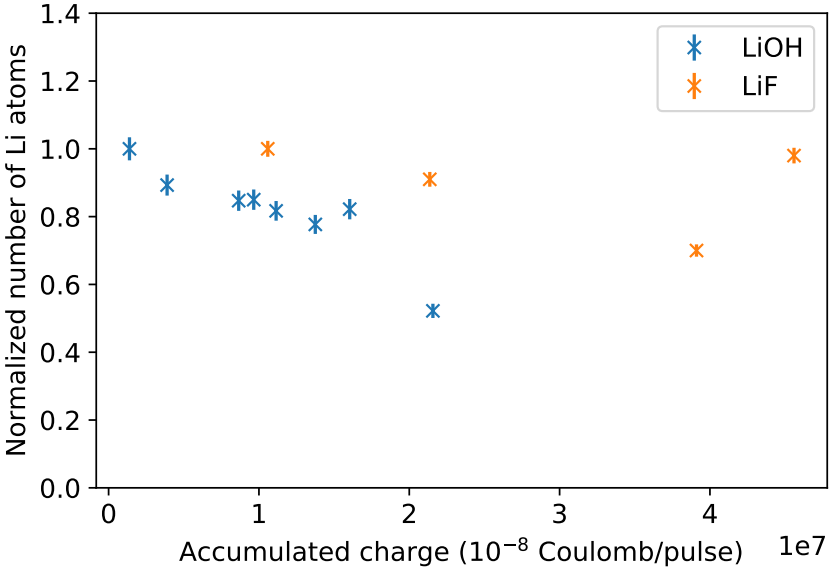

FIGURE 3.11: Evolution of Li content in target, in normalized number of Li atoms as a function of accumulated charge.

The evolution of each target was monitored by looking at the evolution of the number of lithium over accumulated charge. This evolution is shown for one target of each compound in Fig. 3.11, for clarity, the number of lithium atoms has been normalized. The orange

crosses show a target of LiF. The LiF target is stable until we reach 0.41 Coulomb. The LiOH (blue) behaves well enough for us to use it, as long as we stay below 0.15 Coulomb for a target with $\Delta E = 20$ keV.

Lithium fluoride is a more stable compound, however, the (α, n) channel of ^{19}F did not allow us to keep using it. We showed that the LiOH compound can be used under high intensity beam.

3.3.1.3 Evidence of lithium drift in the backing

During the evaluation of the target characteristics with a helium beam at $E_{cm} = 0.72$ MeV on a 40 keV thick LiF target evaporated on tantalum, the resulting γ spectra presented two peaks around the energy where the γ-ray of the transition from the direct capture to the excited state at E_{ex} =4.45 MeV, noted $DC \rightarrow 4.5$ MeV, was expected, see in Fig. 3.12 between 3.2 MeV and 5 MeV. The signature γ-ray from the direct capture at this beam energy to the $E_{ex} = 4.45$ MeV is present at an energy of 4940 keV.

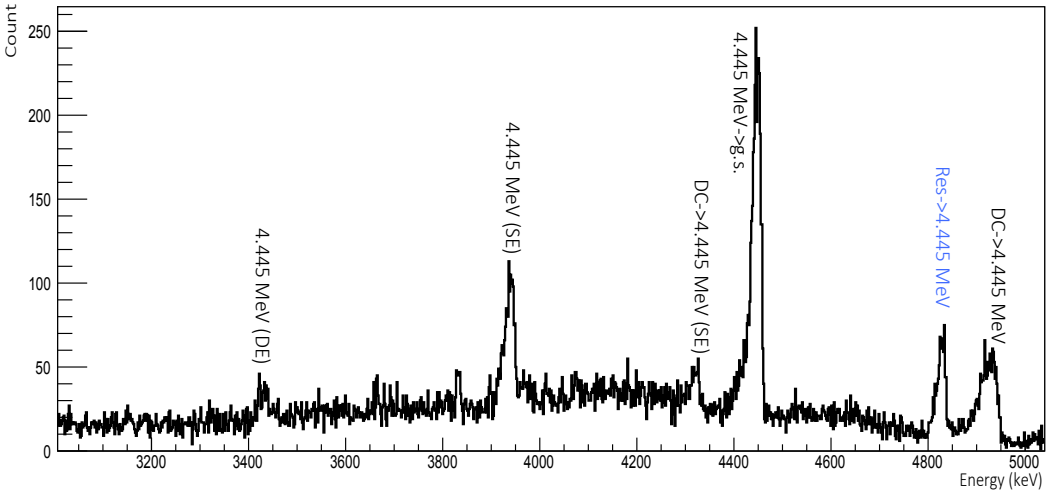

FIGURE 3.12: Spectra above the $E_{cm} = 0.61$ MeV resonance.
γ-ray spectra 100 keV above the resonance at $E_{cm} = 0.61$ MeV. SE and DE indicate the single and double escape peaks.

A second peak a 100 keV lower can be seen. This peak at 4826 keV is the signature that the resonance at $E_{cm} = 0.61$ MeV is being populated. The beam energy (0.72 MeV) is too high to be able to populate the resonance with a 40 keV thick target. The only possible conclusion is that some of the lithium is drifting into the backing where eventually the beam loses enough energy to populate the resonance at $E_{cm} = 0.61$ MeV. Fig. 3.13 is an illustration of this phenomenon.

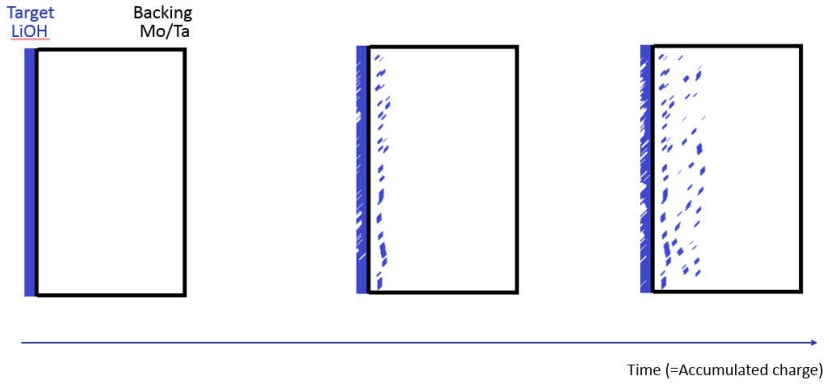

FIGURE 3.13: Cartoon of the lithium drifting into the backing: lithium atoms go deeper into the backing over time.

The inherent problem of this is the fact that the beam will react with the lithium in the backing and generate γ-rays corresponding to reactions taking place at much lower energy than in the bulk of the lithium target.

While it is not a problem for the primary γ-rays, which are coming from the resonance or the direct capture, because the γ energy measured can be separated, it might be inconvenient for the secondary γ-rays, γ-rays coming from the second transition of a cascade, these levels can be populated either by the direct capture (in the LiOH target) or the resonance (from lithium in the backing).

Therefore, it is necessary to understand how the lithium drifting impacts data at higher energies, the most important question being: does the lithium continuously penetrate deeper into the target over time? It is also interesting to evaluate if a different backing material enhances or reduces the amount of lithium drifting in the backing. We compared two backings, tantalum and molybdenum to study the drifting. The results of this comparison are presented below.

To compare these backings, we studied the 4826 keV γ-ray coming from the transition between the resonance and the state at 4444.98 keV ($Res \rightarrow$ 4.445 MeV transition). We compared the yield of this transition on and off resonance:

- Quantity 1: yield of the 4826 keV γ-ray peak at the resonance, effectively, we chose an energy leading to the plateau of the resonance.
- Quantity 2: yield of the 4826 keV γ-ray peak far from the resonance (with a beam energy at least 2 times larger than the target thickness in terms of energy)

We then calculated the ratio of these two quantities: Ratio = Quantity 2/Quantity 1. This corresponds to $Y_{E_{beam}>Res+80keV}/Y_{Res}$ in Fig. 3.14, with E_{beam} defined as:

$$E_{beam} = 2 \times E_{loss} + (E_{beam})_{resonance}$$

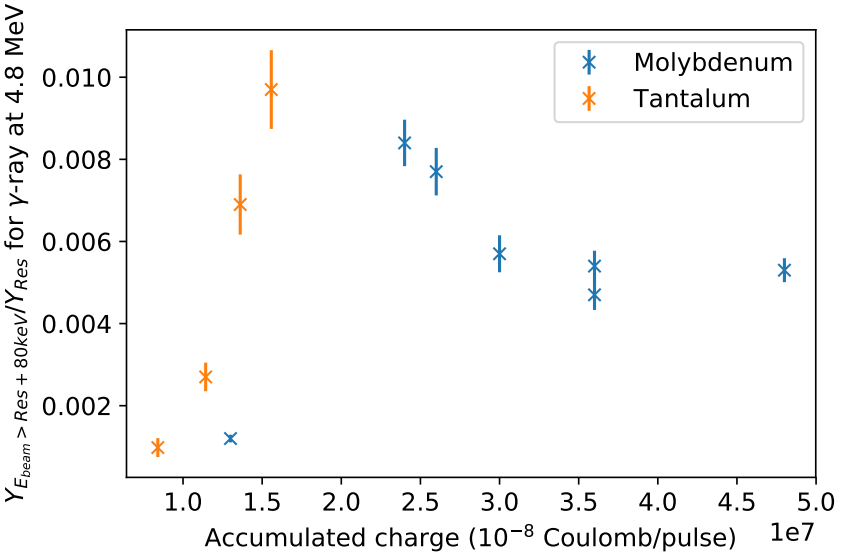

FIGURE 3.14: Ratio of yield in the 4.8 MeV peak at least 80 keV away from the resonance versus on top of the resonance as a function of accumulated charge for two backings: molybdenum and tantalum.

The ratio $\frac{Y_{E_{beam}>Res+80keV}}{Y_{Res}}$ is plotted in Fig. 3.14 as a function of accumulated charge. The blue crosses are for molybdenum and the orange crosses are for tantalum. We do have fewer data points for tantalum, but the trend is slightly steeper (a factor of 1.5) for tantalum. After a great amount of accumulated charge, the amount of lithium drifting seem to reach a plateau in molybdenum. This means that the lithium drifting slows down in molybdenum. We do not have enough data points to conclude anything about the diffusion of lithium into the tantalum backing.

It is important to remark that at most, this phenomenon represents 1% of the counts in the resonance at $E_{cm} = 0.61$ MeV with a tantalum backing and slightly above 0.8 % with a molybdenum backing. This phenomenon is negligible.

During the main experiment, we chose to use the $^{7}Li^{16}OH$ compound evaporated on a molybdenum backing.

The drifting of lithium into the backing for molybdenum, which has been evaluated in this section and compared to the drifting of lithium in tantalum, will be reevaluated, for molybdenum, at energies above $E_{cm} = 1$ MeV in Sec. 4.1.5.

3.3.1.4 Thickness of LiOH layer

The target thickness is a key element to extract the cross section from the yield, see section 4.2.2. Due to the methods used to deduce the target thickness with beam, all the target thicknesses are effective target thicknesses. The target thickness needs to be known and it was estimated and monitored using two different techniques during the main experiment.

Procedure to monitor the target thickness

Between the start of the use of a target and its replacement by a new target, each target was used the following way (detailed description to follow):

- Short run at $E_{cm} = 1.59$ MeV
- Scan of the $E_{cm} = 0.61$ MeV resonance
- Long run measuring the $^7Li(\alpha,\gamma)^{11}B$ cross section, while monitoring the γ-rays from $^7Li(\alpha,\alpha')^7Li^*$ every 20 minutes
- Short run at $E_{cm} = 1.59$ MeV
- Long run measuring the $^7Li(\alpha,\gamma)^{11}B$ cross section, while monitoring the γ-rays from $^7Li(\alpha,\alpha')^7Li^*$ every 20 minutes
- Short run at $E_{cm} = 1.59$ MeV
- Scan of the $E_{cm} = 0.61$ MeV resonance

For each target, we scanned the resonance at $E_{cm} = 0.61$ MeV twice: once when we started to use a new target, and once before replacing it with another target. These scans gave us an estimate of the target thickness in terms of energy loss in the target with a precision of a few keV, as well as an estimate of the number of lithium atoms in the target.

In addition, we used the (α,α') reaction on ^7Li to monitor the degradation of the target as a function of the accumulated charge during and in between each run. To do so, we studied the γ-rays at 478 keV coming from the first excited state of ^7Li. Even with the lead shielding, the cross section of this reaction is high enough to allow for the monitoring of the amount of lithium on target.

A two minute run to get the initial ratio of γ-rays from $E_{ex} = 478$ keV in ^7Li versus accumulated charge was performed at $E_{cm} = 1.59$ MeV to serve as anchor point. We chose

this energy because the cross section is large and in our energy range, although, what was important was to go back to the same energy every time to get a good normalization. The resonance at $E_{cm} = 0.61$ MeV was scanned, after the two minute run at $E_{cm} = 1.59$ MeV, assuming that the number of lithium atoms would not change over the two minute run. Between each long run (used to accumulate statistics in the γ peaks from $^{7}Li(\alpha,\gamma)^{11}B$), a two minute run was performed. This two minute run was always performed at the same energy ($E_{cm} = 1.59$ MeV) to find the ratio of γ-rays at 478 keV and keep track of the relative amount of lithium on target. The number of long runs on each target was variable.

Example of monitoring

An example of the monitoring can be seen in Fig. 3.15. The blue dots are associated with the monitoring of the first excited states of ^{7}Li, $E_{ex} = 478$ keV, during long runs. We do not provide uncertainty on these points because it was a qualitative measurement to make sure that the target was not losing all of its ^{7}Li content. The points which do not follow the line trend could be due to numerous factors, related to the consistency of data taking, because the programs (MPANT and the current integration program used to record the charge on target) were not stopped to get the charge or count in the photopeak at $E_{ex} =$ 478 keV. The numbers used to calculate the normalized yield were acquired during the run without stopping the data acquisition system. Depending on the time period between the recording of the charge on the target and the estimation of the 478 keV peak content the ratio can change significantly. The orange crosses represent 2 minute runs that were done at the same energy before and after each run to keep track of the target thickness.

The ratio of counts in the 478 keV γ peak and the accumulated charge drops at 3.8 Coulomb and increases again at 4.2 Coulomb. The observed drop in normalized yield between 3.8 and 4.2 Coulombs has no conclusive explanation. A possible explanation is that the wobblers were not used and that the target was not evaporated uniformly over the backing, or the beam landed on a target spot with less LiOH.

Results

Using method 1 (using the resonance strength) and method 2 (using the energy loss and the stopping power), see Sec. 3.3.1.1, and following the procedure described above, we were able to extract the thickness of the targets used during the experiment. The results will be presented below.

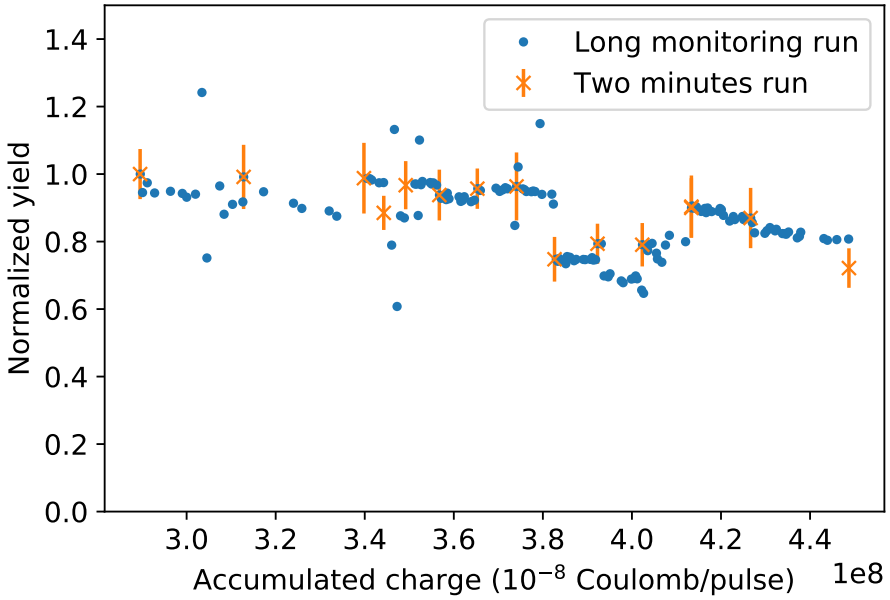

FIGURE 3.15: Sample of monitoring of the yield of the 478 keV line. The blue dots represent the long run monitoring and the orange crosses are the two minute runs in between each long run.

We were able to measure the number of ^7Li atoms using method 1 on each of the γ-rays coming from the resonance at $E_{cm} = 0.61$ MeV, i.e. γ-rays from the following transitions $Res \rightarrow g.s.$ (9271 keV), $Res \rightarrow 4.445$ MeV (4826 keV) and $4.445 \rightarrow g.s.$ (4445 keV).

The different results found using method 1 are plotted in Fig. 3.16. In blue crosses is the number of lithium atoms inferred from the γ-ray at 9271 keV, in green crosses is the one inferred from the γ-ray at 4445 keV and in orange crosses is the one from the γ-ray at 4826 keV. The horizontal axis is the target number + 0.1 * the scan number, hence target 1 is between 1 and 2, target 2 between 2 and 3, and so on. Target 2 does not have a second scan. We can see on the figure that the first scan always has a larger lithium content than the second scan. Fig. 3.16 shows a good agreement within the number of lithium on target inferred from the different γ-rays available. The three different numbers of lithium atoms on target, inferred from the different γ-rays coming from $^7Li(\alpha,\gamma)^{11}B$ at 0.61 MeV, were used to get a weighted average with a smaller uncertainty and are presented in Table 3.2.

The target thickness in terms of energy loss, using method 2, was only inferred from the γ-ray at 4.445 MeV. The results from this method can also be found in Table 3.2.

Table 3.2 shows the thicknesses in energy loss at $E_{cm} = 0.61$ MeV and the number of target atoms, of the targets during their first use and their last moment of use. This information

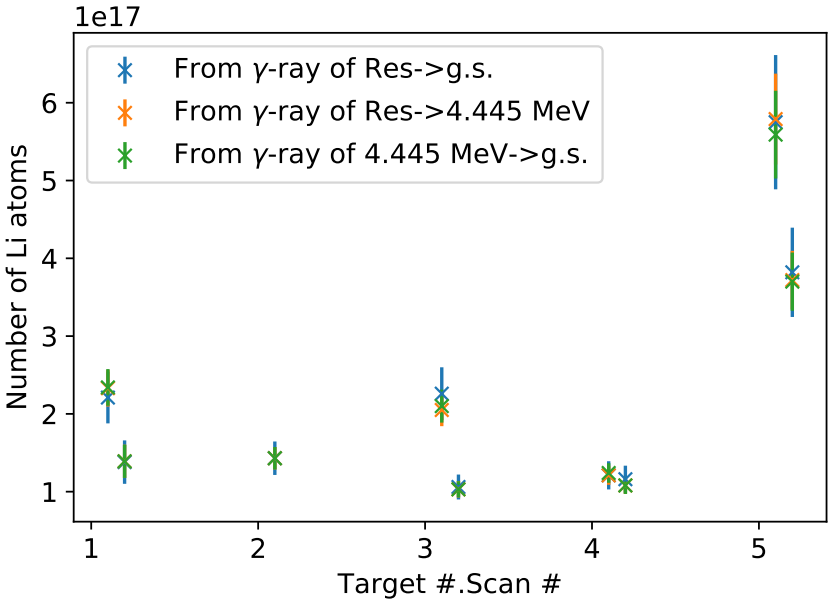

FIGURE 3.16: Number of lithium atoms from different transitions calculated using method 1 with the resonance at $E_{cm} = 0.61$ MeV. The blue crosses are associated with the resonance to ground state transition, the green crosses are from the $E_{ex} = 4445$ keV to ground state transition and the orange crosses are from the resonance to $E_{ex} = 4445$ keV transition. The horizontal axis is the target number + 0.1 * the scan number, hence target 1 is between 1 and 2, target 2 between 2 and 3, etc.

Target number	E_{loss}^{start} (keV)	E_{loss}^{end} (keV)	$\#Li_{atom}^{start}$	$\#Li_{atom}^{end}$
1	24.85	15.19	2.31×10^{17}	1.39×10^{17}
	±0.69	±0.69	$\pm 1.49 \times 10^{16}$	$\pm 1.33 \times 10^{16}$
2	16.15	14.07 *	1.43×10^{17}	1.23×10^{17} *
	±0.69	±0.66	$\pm 9.22 \times 10^{15}$	8.0×10^{15}
3	17.43	12.19	2.10×10^{17}	1.03×10^{17}
	±0.75	±0.84	$\pm 1.36 \times 10^{16}$	$\pm 6.70 \times 10^{15}$
4	16.97	17.65	1.22×10^{17}	1.09×10^{17}
	±0.84	±0.85	$\pm 7.89 \times 10^{15}$	$\pm 7.05 \times 10^{15}$
5	34.21	26.86	5.70×10^{17}	3.73×10^{17}
	±0.69	±0.69	$\pm 3.67 \times 10^{16}$	$\pm 2.41 \times 10^{16}$

TABLE 3.2: Target thicknesses in terms of energy loss and number of lithium atoms at the beginning and end of use of each target.
*: infered from $^7Li(\alpha, \alpha')$ only, see text for details.

is inferred using the excitation curve from the resonance at $E_{cm} = 0.61$ keV using method 1 and method 2.

The information at the end of use of the second target (energy loss and number of Lithium atoms) are only scaled from the ratio of count in the γ peak coming from the $^7Li(\alpha, \alpha')$ reaction at 1.59 MeV with the number of charge measured on target. The last run with this target was cut short because of technical issues and this target was removed before performing a scan of the resonance at $E_{cm} = 0.61$ MeV.

The various uncertainties involved in method 1 (using the resonance strength) are treated as statistical for the error propagation. This is valid because method 1 is based on the number of count in the γ-ray peak coming from the resonance at $E_{cm} = 0.61$ MeV and the number of beam particles. Because three γ-rays were available to calculate the area under the excitation curve, we then used a weighted average to reduce the uncertainty on the number of lithium atoms. The systematic errors due to the resonance strength of the 0.61 MeV resonance and the detection efficiency are included in the propagation of error.

The uncertainties involved in method 2 (using the stopping power from [73]) are also treated as statistical for the error propagation. This is valid since the number of lithium atoms is scaled to the ratio of the number of count of γ-rays coming from the first excited state in ^{7}Li and the number of beam particle. Two γ-rays were used to calculate the energy loss in the target, then a weighted average was performed to reduce the uncertainty on the number of lithium atoms. In the propagation of uncertainty, we used the stopping power which is a systematic error.

Comparison of method 1 and method 2

For a particular run, both methods (using the resonance strength (1) and using the energy loss (2)) were compared.

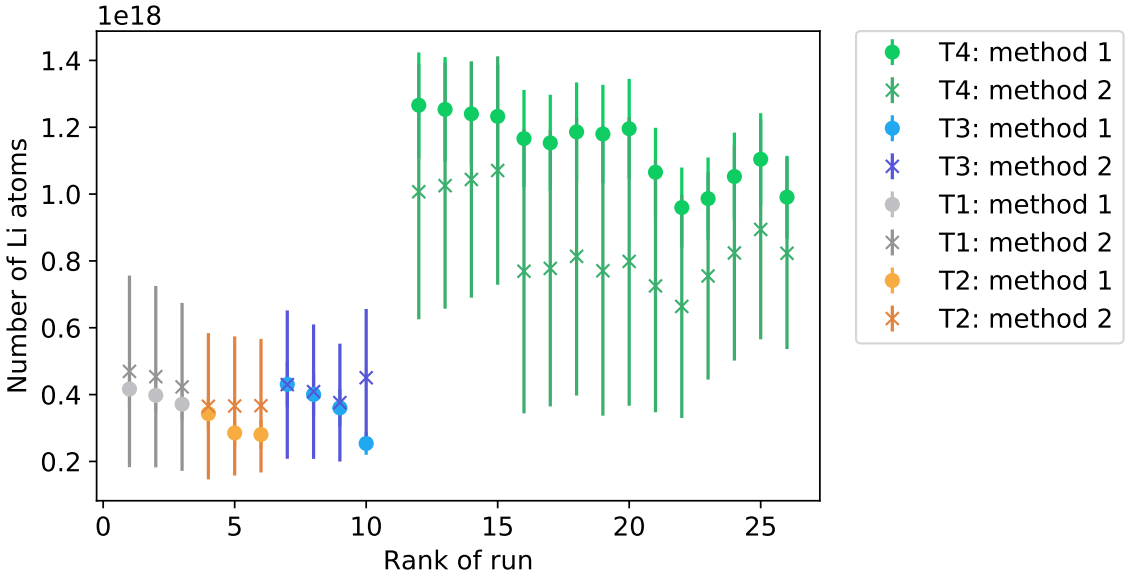

FIGURE 3.17: Comparison of the number of lithium atoms extracted for each run using method 1 (using the resonance strength), dots, and using method 2 (using the energy loss), crosses, as a function of the run ranked from 1 to 26 by order of increasing run number. The different targets are in different colors, target 1 in shades of grey, target 2 in shades of orange, target 3 in shades of blue and target 4 in shades of green.

For each run, the number of lithium atoms during a particular run was calculated with either method 1 and 2. The number of lithium atoms was then scaled to the percentage of $^7Li(\alpha,\alpha')$ reactions detected durung the run at $E_{cm} = 1.59$ MeV right before and right after each run for each target because the exact number of Li atoms, calculated with either method 1 or method 2, was not available for each run: the ratio allowed us to correct for a more accurate number of Li atoms since the target scans were only done twice per target (when that target was first mounted on the beam line and before it was replaced by a new one). The numbers of lithium atoms before and after the run were then averaged as the degradation of the target is linear, see Fig. 3.15.

The results of the two methods (using the resonance strength or the energy loss) used to extract the number of target atoms can be seen in Fig. 3.17. The dots are the number of lithium atoms in a particular run extracted from the excitation curve using the area under the curve. The crosses are the number of lithium atoms for the same run extracted using the energy loss and the stopping power. The two method agree well using the 20% uncertainties advised by Ziegler [73]. The target thickness for each target, separately, agree well with each other and we can observe the degradation of the target as the number of the run increases. A drop can be noticed between rank 20 and 24, it is the same drop we noticed previously in Fig. 3.15.

Energy loss at high energy

The energy loss in keV in LiOH is measured using the resonance at $E_{cm} = 0.61$ MeV. The range of energy we were interested in is between 1.2 MeV and 1.8 MeV and with a higher beam energy, the energy loss, in the same target, will be smaller. We determined the energy loss for beam energies between 1.2 MeV and 1.8 MeV using SRIM [73].

3.3.2 Setup Characterization

The characterization of the setup involves the characterization of both the detector and the analyzing magnet. The results of the characterization, namely the detector efficiency and the summing, the detector energy calibration and the energy calibration of the analyzing magnet, will be presented in this section.

3.3.2.1 Detector energy calibration

Calibrating the energy of the detector consists of relating the channels number of the multiple channel analyzer with the energy from γ-rays deposited in the detector. To do so, the ^{137}Cs, ^{60}Co, ^{56}Co and ^{152}Eu γ-ray sources were used along with the measurement of the resonances at $E_{cm} = 0.61$ keV from ^{11}B and at $E_{cm} = 0.96$ MeV and $E_{cm} = 1.27$ MeV from the $^{27}Al(p,\gamma)^{28}Si$ reaction.

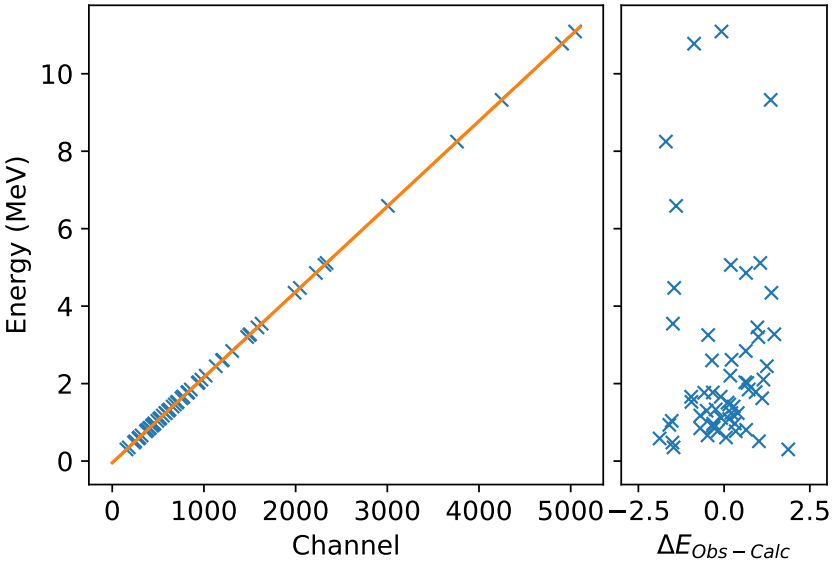

FIGURE 3.18: On the left, detector calibration between 0.61 MeV and 11.7 MeV and its fit. On the right is plotted, for each γ-ray energy, the residual of the fit, $\Delta E_{Obs-Calc}$ in keV.

The energy, vertical axis, and corresponding channel, horizontal axis, are plotted in the left panel of Fig. 3.18 for several known γ-ray energies. They are linearly fitted with:

$$a \times x + b = y \quad \text{with} \quad a = 2.205 \pm 1.1 \times 10^{-4} \quad \text{and} \quad b = -43.76 \pm 0.18$$

The uncertainties on the coefficient a and b come from the linear regression. The right panel of Fig.3.18 shows the residuals of the fit. The calibration of the energy is correct within $\pm$ 2 keV.

3.3.3 Detector Efficiency

The detector efficiency is an essential parameter to extract the differential cross section from the yield, because it corrects for the effects due to the geometry of the setup. In this

section, the method to extract the photopeak efficiency and single escape peak efficiency of the detector will be presented with their results.

Photopeak efficiency

In the setup we used, the detector efficiency includes the solid angle, the geometry of the detector, the effect of the shielding (it was present during each run) and the photopeak efficiency. It is the ratio of the number of γ-rays at energy E detected over the number of the same γ-rays emitted by the source.

The γ-rays expected in our experiment have energies between 4 MeV and 10 MeV. The radioactive sources available at the NSL do not reach these high energies, and thus we used non-calibrated sources and resonances to obtain detector efficiencies at energies as high as 11 MeV.

To calculate the efficiency we used calibrated sources of ^{152}Eu and ^{56}Co as well as two resonances in $^{27}Al(p,\gamma)^{28}Si$ at $E_{cm} = 0.96$ MeV and $E_{cm} = 1.27$ MeV (using the branching ratios from [74]) and the resonance at $E_{cm} = 0.61$ MeV in $^{7}Li(\alpha,\gamma)^{11}B$, see section 2.2.2.1.

The photopeak efficiency was first calculated from a source of ^{152}Eu with a known activity. This gave access to the efficiency of seven γ-rays at low energy using Eq. 3.7

$$\epsilon_{photopeak}(E) = \frac{C_\gamma}{A(t) \times T \times I} \tag{3.7}$$

where $\epsilon_{photopeak}(E)$ is the photopeak efficiency at the energy E, C_γ is the number of counts in the γ peak of energy E, $A(t)$ is the activity of the source at the beginning of the data acquisition deduced from the known activity, time of production of the source and its half life of the source, T is the duration of acquisition and I the branching ratio of the γ-ray at energy E.

Energies reached by ^{152}Eu are too small compared to the energies of the γ-rays of interest. Therefore, a ^{56}Co source was used as a bridge between the calibrated source of ^{152}Eu and the different resonances in ^{28}Si and ^{11}B.

The ^{56}Co source was made at the NSL. The 11 MV tandem accelerator was used to produce a proton beam to bombard a ^{56}Fe target in order to produce ^{56}Co. The activity is unknown.

The efficiency for the γ-rays coming from the ^{56}Co source was calculated using relative efficiencies. The relative efficiency of a γ-ray emitted by ^{56}Co close in energy to the one emitted by ^{152}Eu at 1299 keV was used as a reference to calculate the relative efficiency

of all other γ-rays emitted by ^{56}Co. The energy of the γ-ray used was 1238.3 keV in ^{56}Co; using the following relation, we can determine the relative efficiency of the γ-ray i:

$$R_i = \frac{C_{\gamma i} \times Br_{1238}}{C_{1238} \times Br_{\gamma i}} \tag{3.8}$$

where $C_{\gamma 1238}$ and $Br_{\gamma 1238}$ are the number of counts in the γ peak at 1238 keV used to scale and its branching ratio and $C_{\gamma i}$ and $Br_{\gamma i}$ are the number of counts in the γ peak being scaled and its branching ratio.

Using the γ-rays at 1299 keV in ^{152}Eu, and 1238 keV in ^{56}Co the efficiency of the γ-rays at higher energy from ^{56}Co can be deduced. Since these two γ-rays are close in energy, they were assumed to have the same efficiency. This means that for the γ-ray at 1238 keV and 1299 keV from ^{56}Co and ^{152}Eu respectively, we have $\epsilon_{1238} = R_{1238} \times \epsilon_{1299}$ and $R_{1238} = 1$. The uncertainties on the photopeak efficiency of γ-rays from ^{56}Co were found to be 20% increased compared to the uncertainties of the photopeak efficiency in ^{152}Eu, using the usual propagation of uncertainty. This is valid because most of the uncertainty is statistical: we use the number of count in the γ peaks to calculate the efficiency, the uncertainty due to the activity of the calibrated source is systematic and included in the propagation of uncertainty.

At the energy of interest in boron, a long run on two resonances of ^{28}Si -created through $^{27}Al(p,\gamma)$- at $E_p = 0.96\ MeV$ and $E_p = 1.27\ MeV$ were used. The 0.96 MeV resonance has a γ-ray at 1522 keV that was matched with a γ-ray at 1408 keV in ^{152}Eu in order to avoid a larger uncertainty with scaling from an efficiency already scaled. The γ-ray at 1779 keV from the resonance at 0.96 MeV was matched to the same γ-ray in the 1.27 MeV resonance.

The results of the efficiency calculation up to 12 MeV are presented in Fig. 3.19. The different γ-rays coming from the aluminum resonances had to be corrected for summing, see section 3.3.4.

The shape of the photopeak efficiency in this setup differs a little from a normal germanium photopeak efficiency curve because the low energy γ-rays are blocked by 1.905 cm of lead.

The uncertainties on the efficiency calculated using Eq. 3.7 arise principally from the number of count in the γ-ray peak of which the efficiency is being calculated and from the uncertainty on the original activity of the source used. The uncertainty on the relative efficiency, Eq. 3.8, essentially comes from the uncertainties on the number of counts in the

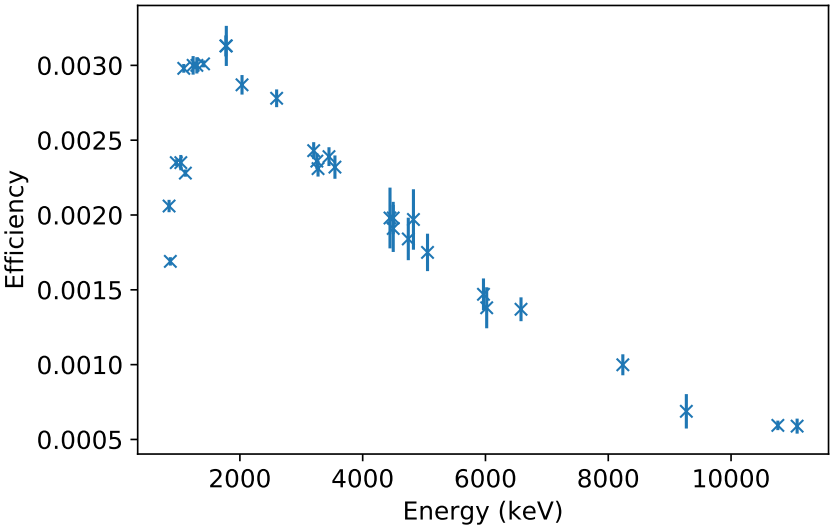

FIGURE 3.19: Photopeak efficiency as a function of γ-ray energy. All efficiency runs were taken with lead shielding in front of the detector.

γ-ray peak because most of the branching ratios in the different reactions used have similar uncertainties and cancel out. The relative efficiency was calculated for several independent acquisition and a weighted average of the relative efficiency was performed to reduce its uncertainty. The uncertainty on the efficiency inferred from the relative efficiency include both the uncertainty of the efficiency they are scaled from and the uncertainty on the relative efficiency, at a first approximation, the correlation can be neglected.

We used the propagation of error in both cases to find the uncertainty on the efficiency.

Single escape peak efficiency

To increase the statistics of the γ-ray counts from the resonance to ground state transition, we used the single escape peak. The efficiency of the single escape γ-ray was then needed to correct the number of γ-rays counted in the single escape peak.

We calculated the relative efficiency by using the ratio of γ-rays counted in the photopeak and γ-rays counted in the single escape peak. The photopeak efficiency was then used to find the efficiency of the single escape peak. The result, corrected for summing, is presented in Fig. 3.20.

The same method as previously described for the photopeak efficiency using the relative efficiency was used to calculate the uncertainties on the efficiencies of the single escape peak γ-ray.

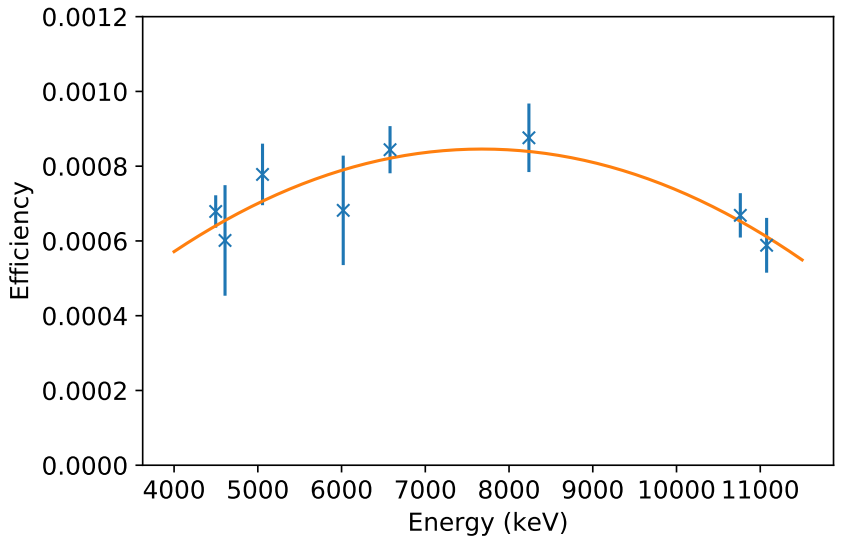

FIGURE 3.20: Photopeak efficiency of the single escape γ-ray peak as a function of γ-ray energy. All efficiency runs were taken with lead shielding in front of the detector.

3.3.4 Summing correction factor

The summing mentioned in this section is the coincidence summing, or true summing, as opposed to random summing which cannot be corrected for. It corresponds to the detector associating two low energy γ-rays from the same cascade. Instead of having one count in each of the low energy peaks in the detector, we will detect one count in a peak at higher energy (being the sum of the two γ-rays energies).

This leads to two effects in the spectra. First, high energy peaks get more counts than they should, so the summing correction needs to take into account the extra counts at high energy. Second, the lower energy peaks lose counts through summing and therefore need a summing correction factor that will increase their count number.

In order to correct for this phenomenon we used the efficiency. For each source and resonance, data were taken close to the target and at a distance of 30.48 cm (= 1 ft) from the target. At a larger distance, the summing is smaller. This gave two efficiencies that are different:

- At close distance, the solid angle is larger and includes a summing term.
- At far distance, the solid angle is smaller and does not include a summing term.

To find the factor needed to correct the data at close distance for summing, the ratio of efficiency at close and far distance was calculated, and corrected for the difference in solid

angle. The different summing correction factors are listed in Table 3.3. Summing factors are expected to vary with energy because they depend on efficiency. The summing also depends on the branching ratios (J^{π} dependence) if the γ-ray is involved in a cascade.

Reaction	Energy (keV)	Summing
$^{27}Al(p,\gamma)^{28}Si$	5967.45	$0.1044 \pm 3.4 \times 10^{-3}$
$^{27}Al(p,\gamma)^{28}Si$	5056.09	$0.1093 \pm 3.6 \times 10^{-3}$
$^{27}Al(p,\gamma)^{28}Si$	4496.92	$0.1107 \pm 2.9 \times 10^{-3}$
$^{27}Al(p,\gamma)^{28}Si$	4497.6	$0.098 \pm 5.2 \times 10^{-3}$
$^{7}Li(\alpha,\gamma)^{11}B$	9271.7	$0.110 \pm 2.28 \times 10^{-2}$

TABLE 3.3: Table of correction factors for summing.

Because summing depends on the branching ratios, the efficiency of γ-rays coming from cascades had to be corrected for summing. For instance, the γ-rays at 4496.92 keV (E_{cm} = 1.27 MeV resonance in $^{27}Al(p,\gamma)^{28}Si$) and 4497.6 keV (E_{cm} = 0.96 MeV resonance in $^{27}Al(p,\gamma)^{28}Si$) have the same energy, thus they should have the same efficiency. However, because they are coming from different resonances and different cascades, the summing affecting them is different, see Table 3.3.

Consequently, the efficiency for these two points in Fig. 3.19 was adjusted with the summing factor. The efficiency of the γ-ray at 4496.97 was corrected by a factor of 0.098/0.1107 in order to account for the different summing factor affecting the efficiency (due to their different branching ratios). When calculating the yield, the same efficiency and summing can now be used for these points, along with their respective branching ratios.

The summing factor multiplies the yield such that it will increase the yield of γ-rays impacted by the summing out and decrease the yield of γ-rays at high energy which are larger due to the summing in.

The uncertainty on the summing arises from the uncertainty on the efficiency. Because we calculate the efficiency using the relative efficiency at different distance from the detector in independent run, we used the propagation of errors.

3.3.4.1 Analyzing magnet calibration

The energy selected by the analyzing magnet, used to define the beam energy, was also calibrated. This means that each field in the analyzing magnet, precisely measured with

a NMR probe, was associated with an energy. In order to calibrate the analyzing magnet, several known resonances in ^{11}B and ^{28}Si were used. They are listed in Table 3.4.

Reaction	E_{ex} (keV)	E_{cm} (keV)
$^{27}Al(p,\gamma)^{28}Si$	12541.5	956.6
$^{27}Al(p,\gamma)^{28}Si$	12715	1130.1
$^{27}Al(p,\gamma)^{28}Si$	12855.1	1270.2
$^{7}Li(\alpha,\gamma)^{11}B$	9271.7	607.4

TABLE 3.4: Resonances used to calibrate the analyzing magnet.

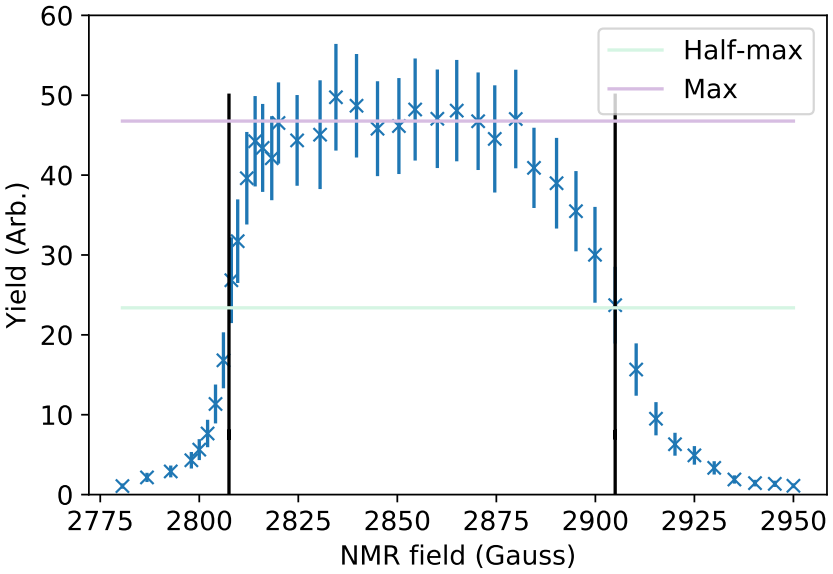

FIGURE 3.21: Typical resonance scan of the E_{cm} =0.61 MeV resonance of the reaction $^{7}Li(\alpha,\gamma)^{11}B$, different colored lines were used to mark the plateau of the resonance, 50% of the plateau and where the excitation curve crosses the lines at 50% of the plateau.

We know precisely the energy of these resonances from the literature (assuming the correct mass) and we measured precisely the field. The plot of the excitation curve, yield versus the analyzing magnet field (in Gauss), allows association of a magnetic field with a resonance energy. The energy can then be linked to the field via the following equation, derived from Eq. 3.1:

$$E = \left(\frac{B\rho q}{\sqrt{2m}}\right)^2 = \left(\frac{Bq}{k\sqrt{m}}\right)^2 \tag{3.9}$$

where E is the beam energy in keV, B the field in Gauss, ρ the magnet bending radius, q the charge and m the beam element mass in amu. The calibration factor found is k. Several resonance scans performed throughout the experiment were used in order to find a good calibration factor.

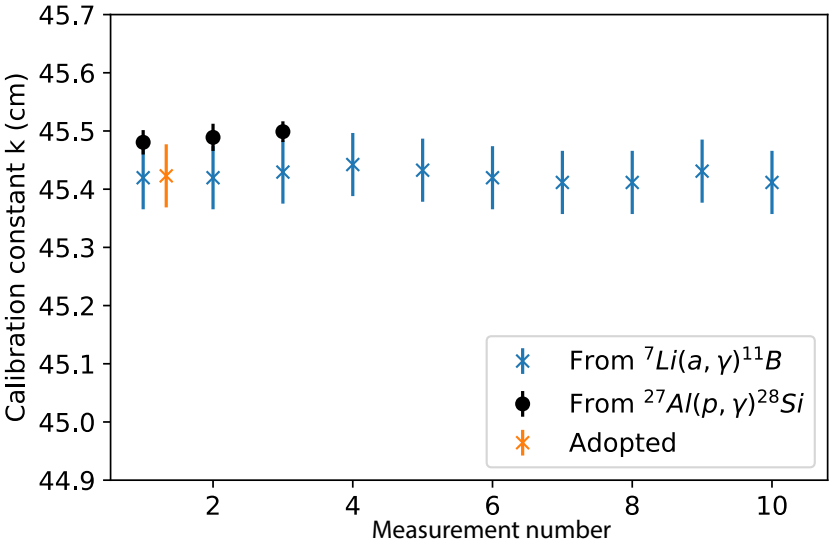

FIGURE 3.22: Calibration factors from different resonances. The black dots indicate resonances in ^{28}Si at 0.96 MeV, 1.1 MeV and 1.3 MeV and the blue crosses indicate the factor extracted from the 954 keV resonance in ^{11}B, the orange cross symbolizes the average of the different factors calculated from the resonance in ^{11}B.

Each calibration factor found with four different resonances from two reactions is plotted in Fig. 3.22. The blue crosses represent every calibration factor from scans of the $E_{cm} = 0.61$ MeV resonance in $^{7}Li(\alpha,\gamma)^{11}B$. The orange cross is the weighted average over all these scans. The black circles represent the calibration factor of three resonances in ^{28}Si from the reaction $^{27}Al(p,\gamma)^{28}Si$ at $E_{cm} = 0.96$ keV, $E_{cm} = 1.13$ MeV and $E_{cm} = 1.27$ MeV, see Table 3.4. While the k value found with $^{27}Al(p,\gamma)^{28}Si$ and $^{7}Li(\alpha,\gamma)^{11}B$ are compatible, a clear trend is visible. The k value obtained from $^{27}Al(p,\gamma)^{28}Si$ are systematically higher than the one obtained with $^{7}Li(\alpha,\gamma)^{11}B$. This difference might be due to the fact that the reactions used to extract the calibration factor used two different beams, helium and hydrogen, and, therefore, two different beam tunes out of the source. However, given that each resonance scan in boron gave the same calibration factor, we are confident we know our beam energy.

There is a good agreement between the several calibration factors from $^{7}Li(\alpha,\gamma)^{11}B$ which were measured over three weeks, and, since every other run used a helium beam, we will use the weighted average of these calibration factors to determine the energy of the beam. Consequently, the calibration factor was reduced to a final value of $k = 45.423 \pm 0.074$ to be used in the rest of the analysis, shown as the orange cross in Fig. 3.22.

The uncertainties on the calibration constant for the bending magnet arise from the uncertainty on the field (known within a gauss which yields a uncertainty on the energy of a

keV) and the uncertainty on the energy of the resonance which comes from the uncertainty on the energy of the excited state and the uncertainty on the masses.

3.4 Summary

In this chapter, the NSL, the accelerator and the setup used to measure the $^{7}Li(\alpha,\gamma)^{11}B$ cross section were presented.

The methods used to characterize the setup and target were presented. The method to keep track of the number of lithium atoms over time was discussed. The results of these different characterizations were presented and we showed that the number of lithium atoms in the LiOH targets are known.

The results of the efficiency and the summing calculations were presented, especially between 4 MeV and 11 MeV, being the range of energy in which we expect γ-ray from the de-excitation of ^{11}B.

The uncertainties due to the efficiency of the detector, the summing and part of the uncertainty due to the target thickness are statistical. For the target thickness we also used the software SRIM, hence part of the uncertainties on the target are systematic. However, the uncertainties are treated as statistical in the error propagation, because the energy loss in the target is statistical, so the uncertainties on the target thickness are statistical. The uncertainties are summarized in Table 3.5

	Statistical (%)	Systematic * (%)
Efficiency $^{\diamond\star}$	1-10	
Summing $^{\diamond\star}$	3-7	
Target thickness (E_{loss})	2-5	$0.2^{\triangleright}$
Stopping power		20
Count number *	3-7	

TABLE 3.5: Different contribution to the uncertainty.
$*$: The uncertainty from the systematic errors were treated as statistical errors in the error propagation.
$\diamond$: The efficiency and the summing are correlated quantities.
$\star$: These elements were used to determine the uncertainty on the yield, differential cross section and the cross section.
$\triangleright$: The systematic uncertainty on the energy loss arises from the uncertainty on the calibration factor that links the field to the energy.

Chapter 4

Data Reduction

The $^{7}Li(\alpha,\gamma)^{11}B$ reaction was studied at the Nuclear Science Laboratory (NSL) of the University of Notre Dame with a helium beam at different energies between 1 MeV and 1.8 MeV (in the center of mass). This energy range is chosen based on the analysis in Chapter 2. As a reminder, the objective is to identify other decay channels than the direct capture or resonance to the ground state. Another goal of this thesis is to calculate the stellar reaction rate between 1 GK and 5 GK, the temperature range relevant to the ν-process. The processes of extracting the cross section and the stellar reaction rate are described in this chapter.

First we will describe the measured γ-ray energy spectra: the γ-rays evidence of ^{11}B de-excitation, the room background and the beam induced background. Then, the extraction of the cross sections will be detailed and we will conclude this chapter by presenting the cross section resulting from our measurement as well as the stellar reaction rate.

4.1 Unraveling the Spectra

In this section, the different features of the spectra will be presented: the γ-ray that gives evidence that the $^{7}Li(\alpha,\gamma)^{11}B$ reaction took place, the background, the evidence of the production of neutrons and the drifting of lithium in the backing in this particular energy range will be discussed.

4.1.1 The γ-rays from $^{7}Li(\alpha,\gamma)^{11}B$

The γ-ray evidence that the $^{7}Li(\alpha,\gamma)^{11}B$ reaction took place can be seen in Fig. 4.1, all the spectra we took between $E_{cm} = 1$ MeV and $E_{cm} = 1.8$ MeV are available in Appendix A. This spectrum is a typical γ spectra between 4 MeV and 10 MeV, it is obtained by bombarding a ^{7}Li target with a helium beam at an energy of $E_{cm} = 1.2$ MeV. In this spectrum, we can observe the γ-ray transition between either the resonances (Res) or the direct capture (DC) and the ground state at $E = 9.93$ MeV, noted $DC/Res \rightarrow g.s.$. Because the detector is oriented at 45°, this γ-ray is affected by the Doppler effect, as well as any other γ-ray coming from a reaction. Once corrected for the Doppler effect, the energy of the γ-ray is $E = 9.85$ MeV. The associated single escape peak, at $E = 9.93 - 0.511$ MeV $= 9.42$ MeV can also be observed. We detect the γ-rays corresponding to the $DC/Res \rightarrow 5.02$ MeV transition and the 5.02 MeV $\rightarrow g.s.$ transition as well as their respective single escape peaks. We also measured the γ-rays from the $DC/Res \rightarrow 4.445$ MeV transition and the 4.445 MeV $\rightarrow g.s.$ transition.

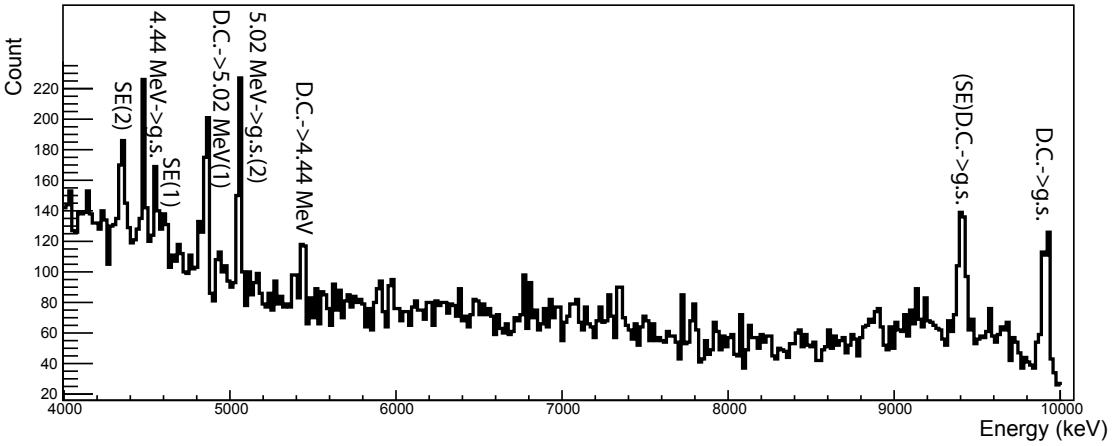

FIGURE 4.1: Energy spectrum of γ-rays obtained with a helium beam at $E_{cm} = 1.2$ MeV. The different γ-rays coming from ^{11}B are identified.

The transitions from the resonances and the direct captures to the ground state were observed before by Paul et al. [1], however, none of the cascades were observed before. The transition $DC \rightarrow g.s$ is present in all of our spectra. The cascade through the excited state at 5.02 MeV is present in all the spectra as well. This is not the case for the cascade through the 4.445 MeV excited state as we will see in section 4.1.4.

Our detector being oriented at 45°, the energy of the γ-ray detected is affected by the Doppler effect according to:

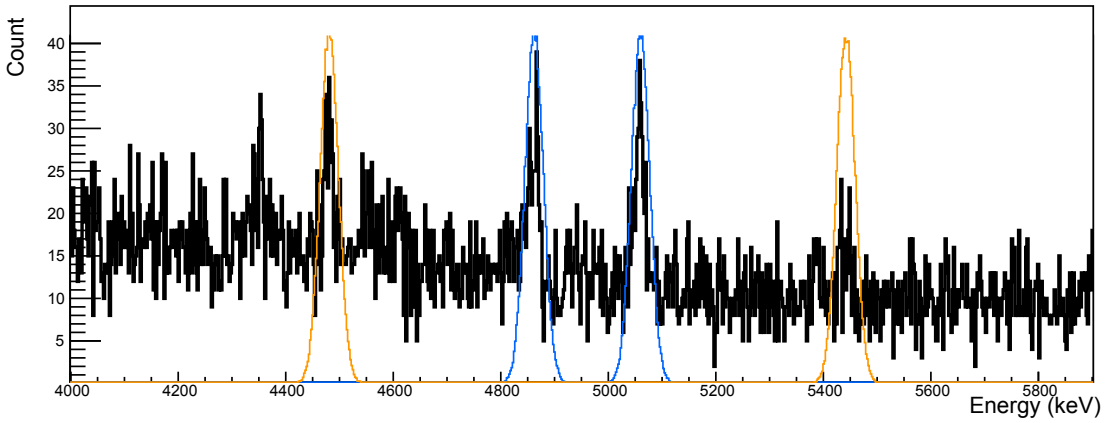

FIGURE 4.2: Zoom of the spectrum in Fig. 4.1 at $E_{beam} = 1.87$ MeV between 4 MeV and 6 MeV. In blue are the γ peaks that arise from the cascade going through the state at 5.0203 MeV and in orange are the γ peaks that arise from the de-excitation through the 4.445 MeV state, see details in the text.

$$E_{doppler} = E_{\gamma}(1 + \cos(\theta)\frac{v}{c}) \tag{4.1}$$

where $E_{doppler}$, E_{γ} are the γ energy measured (affected by Doppler shift) and the energy of the γ-ray emitted, θ is the angle at which the γ-ray is detected (detector position), v is the speed of the de-exciting recoil and c the speed of light. The correction for the Doppler shift was calculated using Eq. 4.1, after rearrangement into Eq. 4.2 where $\frac{v}{c}$ was calculated considering an (α, γ) reaction,

$$E_{doppler} = E_{\gamma}\left[1 + \cos(\theta)\sqrt{\frac{2 \times E_{beam}}{M_{\alpha}}}\left(\frac{M_{\alpha}}{M_{Recoil}}\right)\right] \tag{4.2}$$

E_{beam} is the energy of the beam in MeV. M_{α} and M_{recoil} are the masses of the beam particle and the recoil in MeV/c^2.

In order to demonstrate that the peak attribution in Fig. 4.1 is correct, a simple simulation following the two γ-rays emitted from each cascade described was performed. Eq. 4.2 was used to reproduce the energy of the cascade we observed from ^{11}B. The two peaks associated with the 5.02 MeV and 4.445 MeV cascade were randomly generated following a Gaussian distribution with a width corresponding to the target thickness. The peaks simulated are from the following transitions:

- $DC/Res \rightarrow 5.02$ MeV
- 5.02 MeV $\rightarrow g.s.$

- $DC/Res \rightarrow 4.445$ MeV
- 4.445 MeV $\rightarrow g.s.$

Each of the simulated γ-rays associated with these transitions was corrected for the Doppler shift. Hence, the Gaussian on which a Doppler shift is applied are centered on the measured energy of the γ-rays detected. The Gaussian peak randomly filled on which a Doppler shift is applied can be seen in Fig. 4.2. The Gaussian peaks in blue are associated with the cascade through the $E_{ex} = 5.02$ MeV excited states and in orange are the ones associated with the cascade through the $E_{ex} = 4.445$ MeV excited states. For each cascade, the peak with the highest energy is coming from the $E_{cm} = 1.2$ MeV direct capture and the second one is the γ-ray going to the ground state.

Across the energy range studied, from $E_{cm} = 1.0$ MeV to $E_{cm} = 1.80$ MeV, the $DC/Res \rightarrow g.s$ transition was observed. In addition, the cascade through the level at 5.0203 MeV has been observed for transitions from the direct captures and the resonances at $E_{cm} = 1.21$ MeV, $E_{cm} = 1.59$ MeV and $E_{cm} = 1.66$ MeV, see Appendix A. Below a beam energy of $E_{cm} = 1.2$ MeV, we observed the cascade through the excited states at 4.45 MeV, as it was observed for the low-lying resonances by Hardie et al. [5], see section 2.2.2.1. Paul et al. [1] did not see any cascade coming from ^{11}B above $E_{cm} = 1$ MeV, see section 2.2.2.2.

4.1.2 Background

The majority of γ-rays in a spectrum comes from background. It can be decomposed into three contributions. The cosmic rays, the room background and the beam induced background. The cosmic ray background is random in energy, in angle and in time, and it will not be discussed here. The impact on the data of the room background and beam induced background will be discussed in the following paragraphs.

4.1.2.1 Room Background

Most of the background present in our γ-ray spectra is due to the room background and comes from natural radioactivity. This is mostly due to the thorium and uranium decay chains.

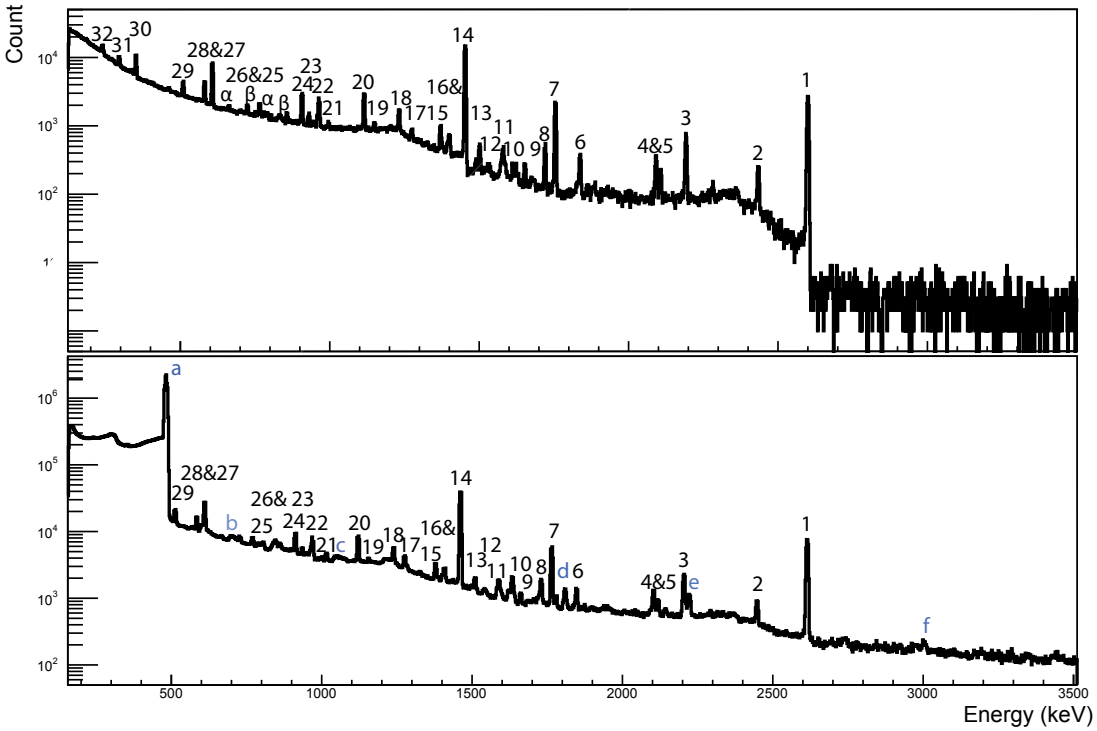

FIGURE 4.3: Top panel: the spectrum of a background run lasting 6 hours. Bottom panel: a 17 hours spectrum at $E_{cm} = 1.352$ MeV below 3.5 MeV.

The start of the uranium decay chain is:

$$^{238}U(\alpha)^{234}Th(\beta^-)^{234}Pa(\beta^-)^{234}U(\alpha)^{230}Th(\alpha)^{226}Ra$$

$$^{226}Ra(\alpha)^{222}Rn(\alpha)^{218}Po(\alpha)^{\mathbf{214}}\mathbf{Pb}(\beta^-)^{\mathbf{214}}\mathbf{Bi}...$$

and the start of the thorium decay chain is:

$$^{232}U(\alpha)^{228}Th(\beta^-)^{\mathbf{228}}\mathbf{Ac}(\beta^-)^{228}Th(\alpha)^{224}Ra(\alpha)^{220}Rn$$

$$^{220}Rn(\alpha)^{216}Po(\alpha)^{212}Pb(\beta^-)^{212}Bi(\alpha)^{\mathbf{208}}\mathbf{Tl}...$$

The major sources of γ background from these two reaction chains are in bold. A room background run is presented in the top panel of Fig. 4.3. The run was six hours long and does not present any identifiable γ-rays peak above 3 MeV. The highest energy γ-ray for room background has an energy of 2614.7 keV and is from the thorium decay chain.

Each peak in the top panel of Fig. 4.3 is associated with a number. The numbers point out room background. Between 600 keV and 800 keV the peaks are assigned a number and

either α or β, due to the limited space. A list of the energies associated with the numbers and Greek letters and the nuclei they come from can be found on Table 4.1 for the room background.

Number	Energy (keV)	Nucleus
1	2614.7	^{208}Tl
2	2447.9	^{214}Bi
3	2204.2	^{214}Bi
4	2103.7	^{214}Bi
5	2118.6	^{214}Bi
6	1847.4	^{214}Bi
7	1764.5	^{214}Bi
8	1729.6	^{214}Bi
9	1661	^{214}Bi
10	1630.4	^{228}Ac
11	1588.0	^{228}Ac
12	1538.5	^{214}Bi
13	1509.3	^{214}Bi
14	1460.8	^{40}K
15	1408.0	^{214}Bi
16	1377.7	^{214}Bi
17	1280.96	^{214}Bi
18	1238.1	^{214}Bi
19	1155.19	^{214}Bi
20	1120.3	^{214}Bi
22	969.1	^{228}Ac
23	934.1	^{214}Bi
24	911.1	^{228}Ac
25β	860.56	^{208}Tl
25β	835.71	^{228}Ac
25α	806.2	^{214}Bi
25α	785.9	^{214}Pb
25α	768.4	^{214}Bi
26β	727.33	^{228}Ac
26β	726.86	^{212}Bi
26α	661.61	^{137}Cs
27	609.3	^{214}Bi
28	583.1	^{208}Tl
29	511.0	e^- annihilation
30	351.93	^{211}Bi
31	295.22	^{214}Pb
32	238.63	^{212}Pb

TABLE 4.1: List of γ-rays from room background [75].

4.1.3 Beam induced background

The beam induced background corresponds to any γ-rays associated with reactions induced by the helium beam which is not the $^{7}Li(\alpha,\gamma)^{11}B$ reaction. The beam induced background is the dominant form of background above 3 MeV and contributes in a lesser part to the background below 3 MeV. In the bottom panel of Fig. 4.3 the beam induced background is indicated with blue letters. The letters, the corresponding γ-rays and the reaction it comes from are listed in Table 4.2.

As discussed in section 2.2.1, the $^{7}Li(\alpha,\alpha')$ channel is an important contribution to the γ count rate in the detector. Despite the lead shielding used to block 97% of the 478 keV γ-rays, the associated peak can be clearly seen in the bottom panel of Fig. 4.3. This is a clear evidence of the large cross section of this reaction.

There is evidence of nuclear reactions on fluorine, sodium and phosphorus in the spectra. They are among the most abundant elements on Earth, so their presence as contaminants in the system is not surprising.

We can also see evidence of a reaction on ^{98}Mo which is the most abundant isotope of molybdenum. This is not surprising either since the LiOH target is evaporated on a thick molybdenum backing.

Number	Energy (keV)	Reaction taking place to produce compound emitting γ-ray
a	477.6	$^{7}Li(\alpha,\alpha')^{7}Li$
b	691.43	$^{72}Ge(n,n')^{72}Ge$
c	1049.4	$^{31}P(n,\gamma)^{32}P$
d	1810.7	$^{98}Mo(\alpha,\gamma)^{102}Ru$
e	2218	$^{19}F(\alpha,\gamma)^{23}Na$
f	3004.2	$^{23}Na(\alpha,\gamma)^{27}Al$
*	4438.91	$^{9}Be(\alpha,n\gamma)^{12}C$

TABLE 4.2: List of background γ-rays induced by the α beam. See section 4.1.4 for the $^{9}Be(\alpha,n\gamma)^{12}C$ reaction named *.

The presence of the peaks labelled b and c in the bottom panel of Fig. 4.3 demonstrates that neutrons are produced and the peak labelled b shows that the neutrons interact with the HPGe detector. The peak labelled b is associated with reactions induced by neutrons on the detector itself. The peak at 691 keV is typical of the $^{72}Ge(n,n')^{72}Ge$ reaction. Over the time of the experiment and in an experiment done after using this detector, we did not observe a degradation in the resolution of the γ peak.

4.1.4 The ∼ 4.4 MeV line

According to the transition strength calculation, see section 2.2.2.3, there is a probability to observe a transition through the 4.445 MeV state and we detected it, see Fig. 4.2, as one of the signatures of the $^{7}Li(\alpha,\gamma)^{11}B$ reaction. However, while a broad peak close to 4.5 MeV is present is every spectrum, most spectra do not seem to present this transition through the 4.445 MeV state.

It can be demonstrated that the peak visible at $E = 4.48$ MeV in Fig. 4.4, as an example, might not be coming from the decay of the $E_{ex} = 4.445$ MeV state to the ground state of ^{11}B, especially, for beam energies above $E_{cm} = 1.19$ MeV. The first evidence is the absence of any γ-ray corresponding to the direct capture to $E_{ex} = 4.445$ MeV in ^{11}B as can be seen in figure 4.4. This figure obtained with a beam energy of $E_{cm} = 1.651$ MeV is zoomed in between 4 MeV and 6.5 MeV. The energy spectrum is in black and in orange the energies where the γ-rays going in and out of the 4.445 state in ^{11}B are expected. For comparison, the energies where the γ-rays going through the state at 5.0203 MeV are in blue. The

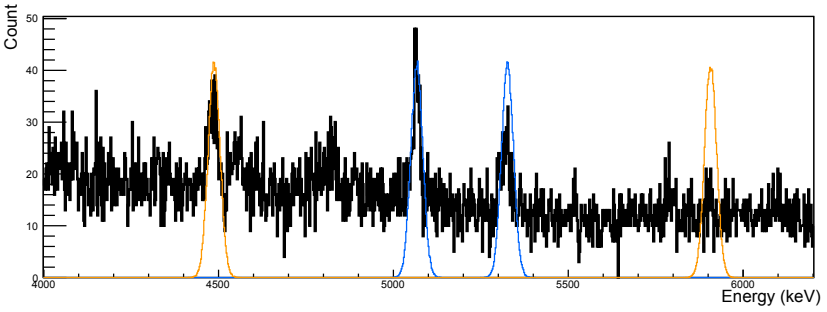

FIGURE 4.4: Extract of the spectra at $E_{cm} = 1.651$ MeV between 4 MeV and 6 MeV. The peaks that should arise from the cascade going through the state at 4.445 MeV in ^{11}B are in orange and the peaks that should arise from the cascade going through the excited state at 5.02 MeV are in blue.

γ-ray at 4.447 MeV matches with the simulated γ-ray coming from the state at 4.445 MeV. However, the γ-ray from the transition between the direct capture and the 4.445 MeV excited state is missing. Since the γ-ray coming from the $DC/Res \rightarrow 4.445MeV$ transition is missing, we can question the origin of the peak at 4.47 MeV.

We also superposed two spectra with different energy, $E_{cm} = 1.65$ MeV in black in Fig. 4.5 and $E_{cm} = 1.60$ MeV in blue in Fig. 4.5, the top panel has been rebinned 4 times and the bottom panel has not. The arrows are pointing at the place where the γ-ray coming from the transition between the direct capture or the resonance and the state at 4.45 MeV

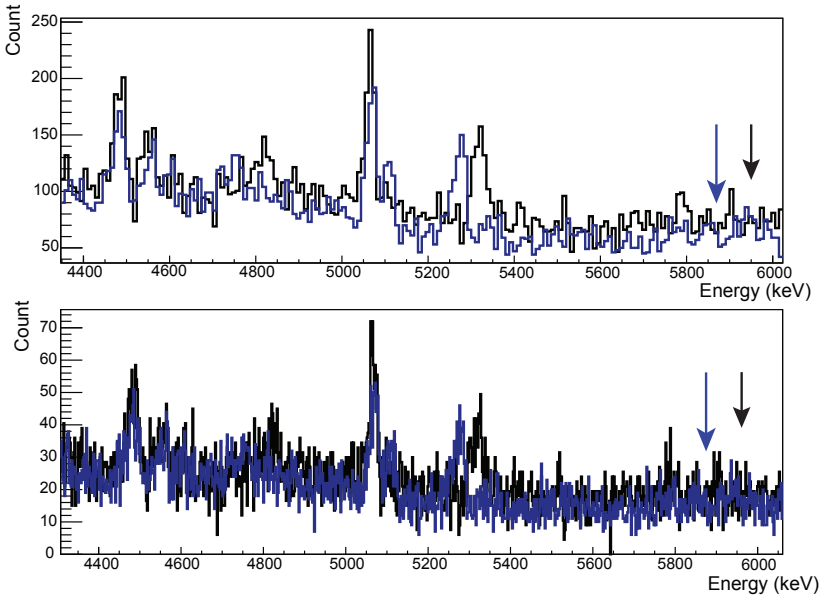

FIGURE 4.5: Superposition of run at different energies (E_{cm} = 1.65 MeV in black and E_{cm} = 1.60 MeV in blue). The top panel in re-binned 4 times and the bottom panel is not. The blue arrow indicate the position of the γ-peak coming from the transition DC→4.445 MeV associated with the spectra in blue and the black arrow indicate the position of the γ peak for the spectra in black.

are expected. Given that even with the Doppler shift, we have a resolution of 2 keV, we understand that, if this γ-ray is emitted, we do not observe it.

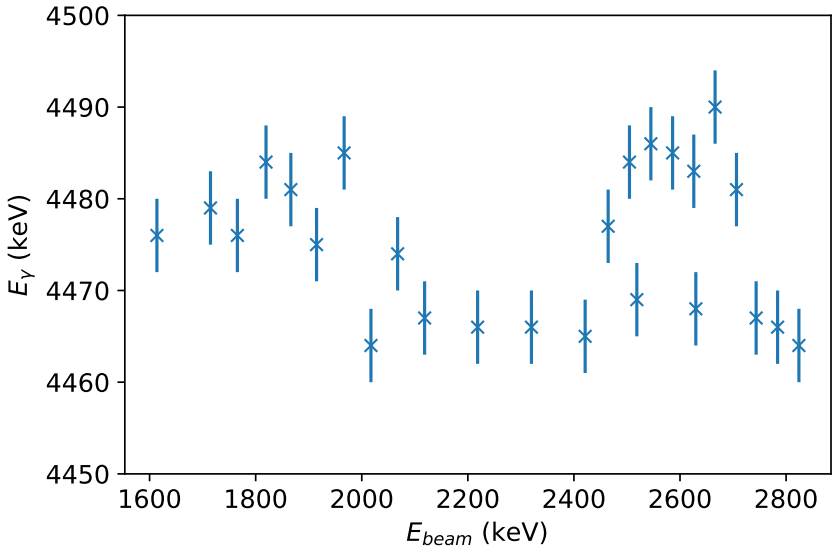

FIGURE 4.6: Evolution of the centroid of the peak at ∼4.4 MeV as a function of the beam energy in the laboratory frame (corresponding to E_{cm} = 1 MeV to E_{cm} = 1.8 MeV).

As another piece of evidence that the 4.445 MeV γ-rays are not coming from a γ cascade in ^{11}B, the evolution of the measured average peak energy as a function of the beam energy was investigated using equation 4.2. From Eq. 4.2, we would expect the trend of the

centroid of the γ-ray as a function of the beam energy to be proportional to $\sqrt{E_{beam}}$. The centroid of the γ-ray at $\sim$ 4.4 MeV from the experimental data is plotted as a function of the beam energy in Fig. 4.6. The trend is not proportional to $\sqrt{E_{beam}}$.

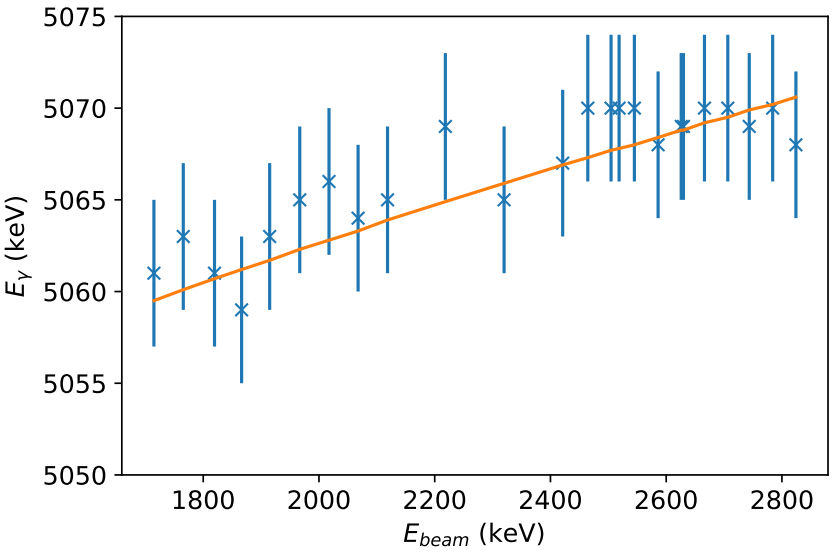

FIGURE 4.7: Doppler trend of the 5.02 MeV line as a function of the beam energy in the laboratory frame (corresponding to E_{cm} = 1 MeV to E_{cm} = 1.8 MeV).

Since the cascade through the 5.02 MeV state is a consistent feature in our γ-ray spectra, the centroid of the peak at 5020.30 keV as a function of the beam energy is plotted, for comparison, in Fig. 4.7. The trend is proportional to $\sqrt{E_{beam}}$, which corresponds to what can be expected from the Doppler effect, see Eq. 4.2. Both the 5.02 MeV and 4.445 MeV γ-rays are secondary γ-rays and should have similar behavior regarding the Doppler effect. We can note that the trend of the centroid of the γ-ray at $\sim$ 4.4 MeV is very different from the one of the γ-ray at $\sim$ 5.02 MeV to which it should be similar. Therefore, it seems that most of the γ-rays in the γ peak at 4.445 MeV might not be coming from $^{7}Li(\alpha,\gamma)^{11}B$ and if part of the transition in ^{11}B goes through the state at 4.45 MeV, we do not observe it.

4.1.4.1 The γ-ray at 4.4 MeV explained

A suitable candidate for the source of the γ-ray at $\sim$ 4.4 MeV is the $^{9}Be(\alpha,n\gamma)^{12}C$ reaction which emits a γ-ray from its first exited state at 4438.91 keV. The cross section of $^{9}Be(\alpha,n\gamma)^{12}C$ is on the order of 0.1 barn, see Fig. 4.8 [76], several orders of magnitude higher than the expected cross section from the $^{7}Li(\alpha,\gamma)^{11}B$ reaction of a few μb maximum [1].

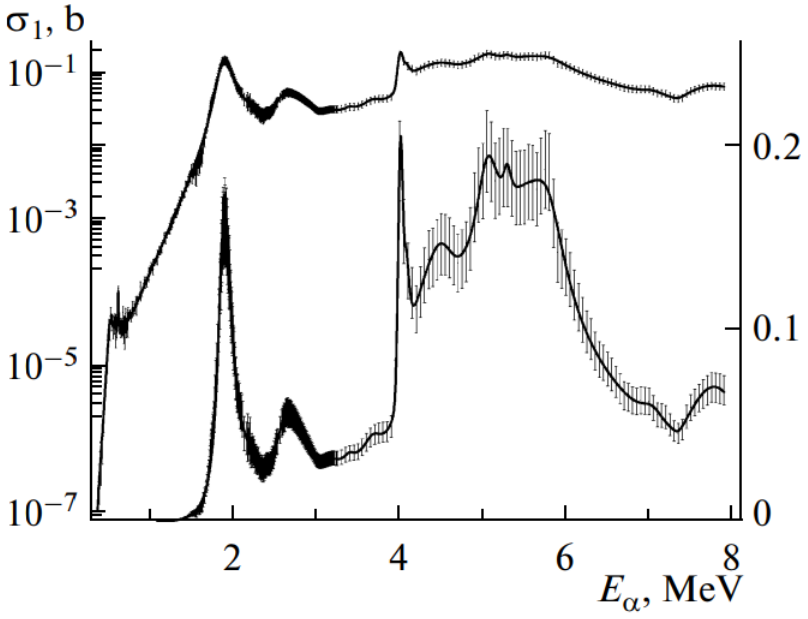

FIGURE 4.8: Figure from [76] presenting the $^{9}Be(\alpha, n\gamma)^{12}C$ total cross section as a function of the beam energy. The left axis addresses the logarithmic curve (highest curve) and the right axis addresses the linear curve (lowest curve).

Another measurement to study the $^{9}Be(\alpha, n\gamma)^{12}C$ reaction by Gin et al. [77] shows a γ-ray shape very similar to the shape observed in our measurement.

The Doppler shift is simulated for this reaction with neutrons emitted at 120°, 100°, 80° and 20°, it gives an idea of the peak that would arise from this reaction and can be seen in Fig. 4.9. The cross section of this reaction was not taken into account: the cross section is assumed to be the same at all angle. The shape was assumed to be a Gaussian as well, this is not true all the time, as showed by Gin et al. [77] and, only 4 angles are considered for the emission of the neutron when they could be emitted in all direction.

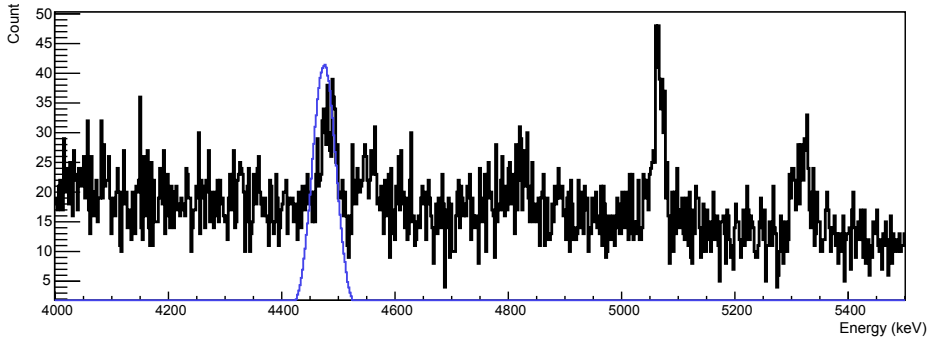

FIGURE 4.9: Extract of the spectra at $E_{cm} = 1.651$ MeV between 4 MeV and 5.5 MeV. The peak that arises from the reaction $^{9}Be(\alpha, n\gamma)^{12}C$ is in blue.

The Doppler simulations made in this work and the measurements of Gin et al. [77] and Gin et al. [76] seem to indicate that most of the counts in the peak at 4.4 MeV are coming from the $^{9}Be(\alpha, n\gamma)^{12}C$ reaction.

4.1.5 Lithium drifting into the backing between E_{cm} = 1.0 MeV and 1.8 MeV

The lithium drifting in the target backing was discussed in section 3.3.1.3. In this section, we examine how the drifting affected the data in the energy range of interest.

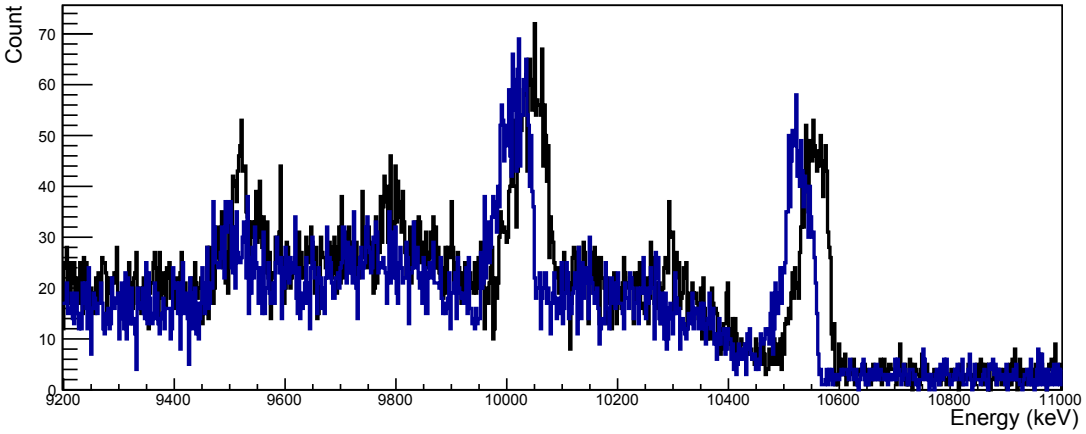

FIGURE 4.10: Drifting evidence at high energy on spectra at E_{cm} = 1.80 MeV, in black, and at E_{cm} = 1.75 MeV, in blue.

The γ spectrum in black in Fig. 4.10 is the highest energy beam with which we bombarded the LiOH target, E_{cm} = 1.80 MeV and the γ spectrum the most affected by the lithium drifting into the backing. The peak due to the lithium drifting into the backing is at 10.3 MeV. This corresponds to the beam losing enough energy in the LiOH target and in the backing to reach the energy corresponding to the resonance at E_{cm} = 1.59 MeV. The peak due to lithium drifting into the backing has 25 $\pm$ 5 counts, while the peak due to the bulk of the target has 1225 $\pm$ 35 counts.

For comparison, in blue in Fig. 4.10 is a γ spectrum at E_{cm} = 1.75 MeV. In this γ-ray spectrum, the peak due to lithium drifting is less present even though the peak due to the bulk of the target has the same number of counts as the one in the spectrum in black. This is due to the fact that by decreasing the beam energy, the beam energy after the bulk of the target is too low to reach the resonance previously reached, the cross section being smaller, the peak due to lithium drifting in the backing is smaller as well.

The spectra in Fig. 4.10 are the worst cases of lithium drifting into the backing above $E_{cm} = 1.0$ MeV. As we can observe, at high energy, the peak from the lithium drifting into the backing is well separated from the peak coming from the bulk of the target. Hence, the high energy peaks from the bulk of the target are not affected by the lithium drifting into the backing. At lower energy, the drifting does not affect the data either because the branching ratio to the excited state at $E_{ex} = 5.02$ MeV is 9.6 % compared to the 90 % branching ratio for the transition $DC/Res \rightarrow g.s.$. Consequently, a significant increase of the count rate is not to be expected from the lithium drifting into the backing. The drifting contributes even less to the spectra than it did at lower energy and can thus be neglected.

4.2 Extracting cross sections

In the following, the analysis of each transition, $DC/Res \rightarrow g.s.$, $DC/Res \rightarrow 5.02$ MeV and 5.02 MeV $\rightarrow g.s.$, will be presented separately. After that, the cross section will be extracted for each of the three γ transitions detected.

4.2.1 Yields

The yield of each transition (Y) was calculated taking into account the parameters of the system: the efficiency (ϵ) and the summing (S) as well as the total number of beam particles measured on target (N_{BP}) and the number of γ-rays at the specific energy corresponding to the transition being studied (C_γ):

$$Y = \frac{C_\gamma}{N_{BP} \times \epsilon \times S} \tag{4.3}$$

This equation was used to calculate the yields of all the transitions observed, i.e. $DC/Res \rightarrow g.s.$, $DC/Res \rightarrow 5.0203$ MeV and 5.0203 MeV $\rightarrow g.s.$.

The uncertainty on the yield principally arises from the number of counts in the γ-ray peak, the efficiency and the summing. The uncertainty in the yield from the efficiency and the summing were calculated using the propagation of correlated quantities, such as:

$$\Delta f(S,\epsilon) = \sqrt{\frac{df(S,\epsilon)}{d\epsilon}\Delta\epsilon + \frac{df(S,\epsilon)}{dS}\Delta S + \frac{df(S,\epsilon)}{d\epsilon}\Delta\epsilon\frac{df(S,\epsilon)}{dS}\Delta S cov(\epsilon,S)}$$

where ΔS is the uncertainty on the summing, $\Delta\epsilon$ is the uncertainty on the efficiency and $cov(\epsilon, S)$ is the covariance of the efficiency and the summing. The uncertainty on the yield was calculated using the propagation of uncertainty.

Cascades yield

Fig. 4.11 presents the yield of $DC/Res \rightarrow 5.0203$ MeV and 5.0203 MeV $\rightarrow g.s.$ not corrected for target effects as a function of beam energy. Considering that the yield is not corrected for target effects, data points taken with different targets will have different yields. The two yields agree within uncertainties. This means that most of the transitions from the direct captures or resonances to the excited state at 5.02 MeV are followed by a transition between this state and the ground state. There is no evidence of γ-rays at an energy lower than 5.0203 MeV that could come from ^{11}B. A weighted average yield of the two transitions, using the uncertainty on the yield as a weight, was used to extract the final yield.

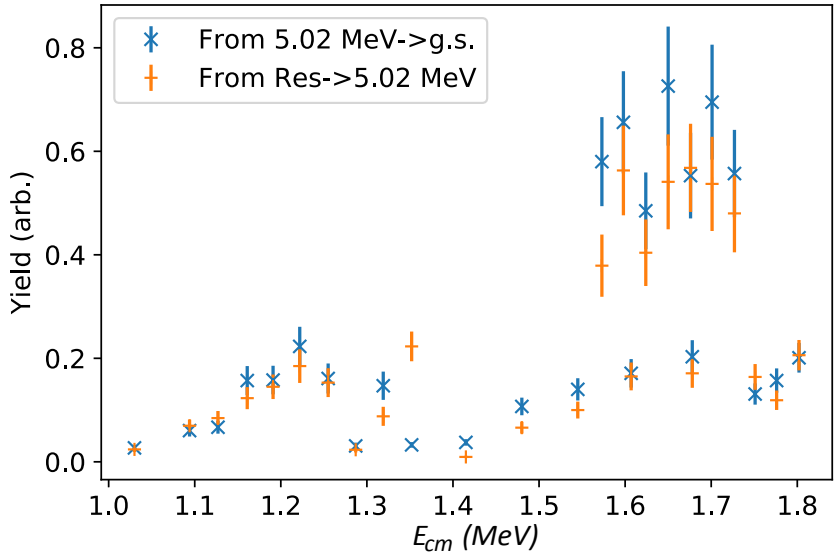

FIGURE 4.11: Yield of $DC/Res \rightarrow 5.0203$ MeV and $5.0203 \rightarrow g.s.$ lines as a function of the beam energy. The points with a lower yield around 1.6 MeV are lower because they were taken on a target with a different thickness (in term of energy loss) as the other points. The yields corrected for target effects can be found in Fig. 4.15

Another cascade from the excited state at $E_{ex} = 5.02$ MeV via the excited state at $E_{ex} = 2.12$ MeV exists, see Fig. 2.1. Although, we do not observe any γ-rays from this transition, this does not mean that this transition does not take place. The transition could be too weak to be detected with our detection system. If this transition does take place, only 14 % of the γ-rays going through the excited state at 5.02 MeV would then undergo a cascade through the excited state at 2.12 MeV, see Fig. 2.1. The branching ratio of the cascade

through $E_{ex} = 5.02$ MeV is 9.6 %, therefore only 1.3 % of the γ-rays would undergo a second cascade through the excited state at 2.12 MeV.

The yield of the cascade through the excited state at 4.445 MeV that we observed at energies below $E_{cm} = 1.15$ MeV are presented in Table 4.3, it has not been corrected for target effect yet. The yield for the secondary transition is much larger than the yield for

E_{cm} (MeV)	Yield $d\sigma/d\Omega_{4.445MeV->g.s.}$	Yield $d\sigma/d\Omega_{DC->4.445MeV}$
1.77	$1.48 \times 10^{-14} \pm 3.81 \times 10^{-15}$	$4.44 \times 10^{-15} \pm 1.47 \times 10^{-15}$
1.72	$1.55 \times 10^{-14} \pm 3.95 \times 10^{-15}$	$7.91 \times 10^{-15} \pm 2.39 \times 10^{-15}$
1.62	$1.24 \times 10^{-14} \pm 3.21 \times 10^{-15}$	$7.01 \times 10^{-15} \pm 2.11 \times 10^{-15}$

TABLE 4.3: Yield for the transition through the excited state at 4.445 MeV. The first column is the secondary transition between the excited state at 4.445 MeV and the ground state, the second column is for the primary transition between the direct capture and the state at 4.445 MeV.

the primary transition, this is due to the contaminant mentioned in Sec. 4.1.4.1. Therefore, the yield that correspond to the transitions through the 4.445 MeV state in ^{11}B is the yield in the second column.

Direct capture to ground state

The γ-ray yield from the direct capture to the ground state was calculated from the photopeak and from the single escape peak which has a comparable number of counts. Because the efficiency was calculated separately for the photopeak and the single escape peak (assuming that all γ-rays detected are only in one peak) the two peaks should yield the same curve.

Fig. 4.12 shows that the two calculations agree with each other. The yields are not corrected for target effects, this is the reason why some of the yields are lower: they were taken with a different target. A yield corrected for target effects can be found in Fig. 4.14. The same method of weighted average was used here to get a better estimation of the yield, weighted using the uncertainties on the yields.

4.2.2 Differential cross sections

The differential cross sections were calculated using two techniques which will be described below.

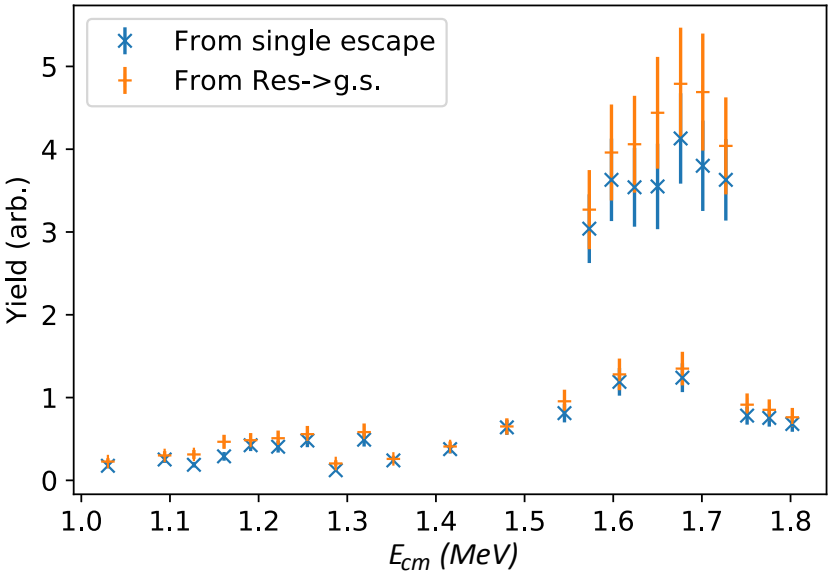

FIGURE 4.12: Yield of $DC/Res \rightarrow g.s$ lines as a function of the beam energy. The points with a lower yield around 1.6 MeV are lower because they were taken on a target with a different thickness (in term of energy loss) as the other points. The yields corrected for target effects can be found in Fig. 4.14.

Thin target approximation

A first approximation of the differential cross section at 45° $(\frac{d\sigma}{d\Omega})_{TTA}$ was calculated using a thin target approximation (TTA). The thin target approximation considers the cross section to be constant over the target thickness.

From the measurement of Paul et al. [1], we expected the resonances to have resonance strength above 100 keV. The targets used had thicknesses below 40 keV, thus the TTA should be a valid approximation: the variation of the cross section over the target thickness should be slow enough to be considered constant.

In this approximation, the differential cross section is found by dividing the yield, Y, by the number of target atoms (N_{Li}):

$$\frac{d\sigma}{d\Omega}_{TTA} = \frac{Y}{N_{Li}} \tag{4.4}$$

The uncertainty on the differential cross section calculated using TTA was calculated using the propagation of uncertainty. The number of lithium atoms is known from a completely independent measurement done on the resonance at $E_{cm} = 0.61$ MeV. This yields uncertainties between 18% and 22%.

Deconvolution of the yield and the target thickness

The differential cross section was also inferred from calculating the yield by integrating the differential cross section. The differential cross section was then varied and integrated to match the calculated yield to the measured yield. This is the accurate way to correct for target effects, the correction is closer to the trend of the cross section. It can be achieved by integrating the cross section over the target thickness using the following equation:

$$Y = \int_{\Delta E} \frac{\frac{d\sigma}{d\Omega}(E)}{SP(E)} dE \tag{4.5}$$

where ΔE is the target thickness in terms of energy loss, $\frac{d\sigma}{d\Omega}(E)$ is the differential cross section and $SP(E)$ is the stopping power. All is known, see section 3.3.1.4, except the differential cross section.

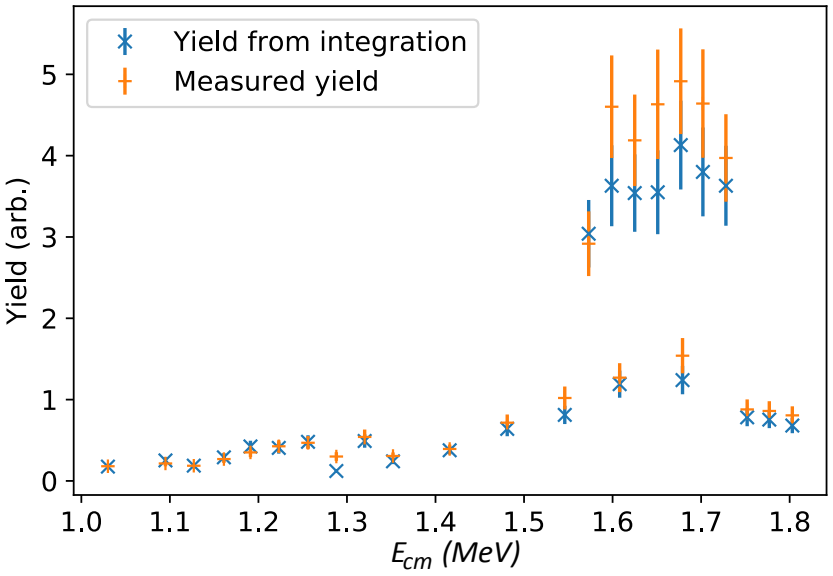

FIGURE 4.13: Yield of $DC/Res \rightarrow g.s$ transition as a function of the beam energy. The experimental yield measured is in orange and the yield calculated by integrating the differential cross section is in blue.

Fig. 4.13 is a comparison of the experimental yield we measured and the yield obtained with the differential cross section we found by integrating the differential cross section over the target thickness to get a yield in agreement with the yield measured. These two yields agree, validating the differential cross section we calculated from the de-convolution of the yield and the target thickness. $\frac{d\sigma}{d\Omega}_{TTA}$ was used as a starting point and then the differential cross section was varied in order to find a yield matching to the measured yield.

The uncertainty on the differential cross section calculated via the deconvolution of the yield and the target effect were inferred from the uncertainty on the yield, because we

reproduced the measured yield while deconvoluting, the uncertainty will only be as good as the uncertainty on the measured yield. The percentage of uncertainty was calculated for the yield and this percentage was applied to the differential cross section (15%).

Comparison of $\frac{d\sigma}{d\Omega}(E)$ and $\frac{d\sigma}{d\Omega}_{TTA}(E)$ for the $DC/Res \rightarrow g.s$ transition

The two differential cross sections are compared on Fig. 4.14. The $\frac{d\sigma}{d\Omega}_{TTA}(E)$ is in orange and $\frac{d\sigma}{d\Omega}(E)$ is in blue. We can see that the integration method, which corrects for the variation of the cross section over the target thickness is different from the differential cross section from the thin target approximation. This means that the cross section variation is not negligible over the target thickness and consequently, the differential cross section from integration should be adopted.

The uncertainty is higher on the differential cross section from the thin target approximation because there is an additional uncertainty due to the target thickness that we do not take into account for the differential cross section from the deconvolution because we use the error of the yield.

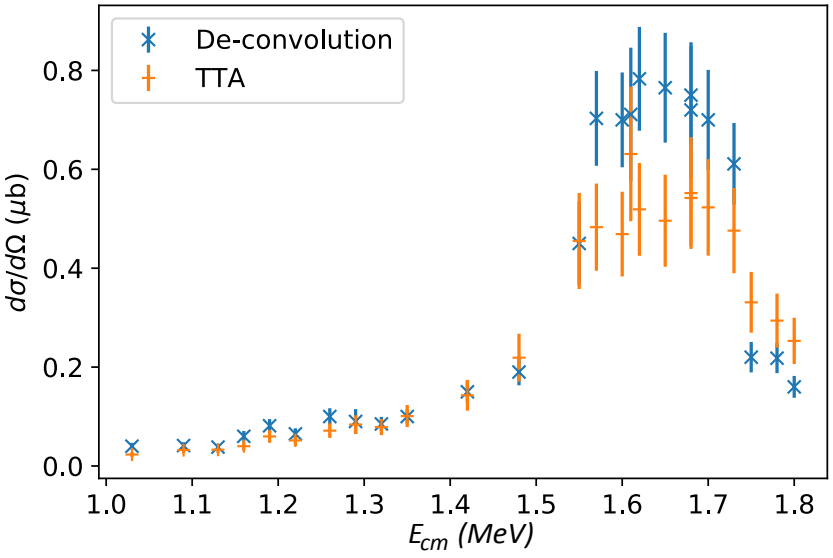

FIGURE 4.14: Differential cross section as a function of the beam energy for the $DC/Res \rightarrow g.s.$ transition. In blue is the differential cross section from the deconvolution of the target effect from the yield. In orange is the differential cross section from the thin target approximation.

Differential cross section for the cascade through the E_{ex} 5.02 MeV

The differential cross section calculated using the deconvolution of the target effect from the yield for the transition between the direct capture and resonances to the excited states at 5.02 MeV is displayed in Fig. 4.15.

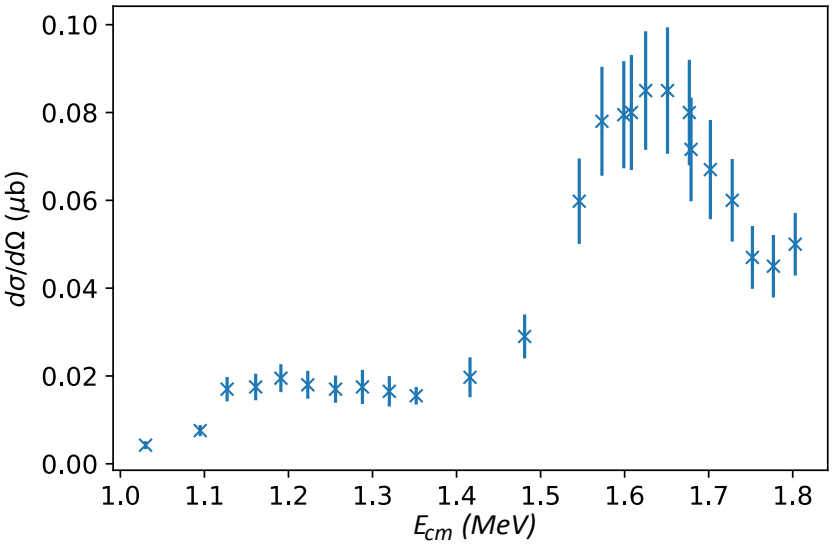

FIGURE 4.15: Differential cross section of the $DC/Res \rightarrow 5.02$ MeV transition as a function of the beam energy.

The two major contributions to the differential cross sections from the three different transitions observed in ^{11}B will be added together as cross sections in the next section to obtain the total cross section.

Differential cross section for the cascade through the E_{ex} 4.445 MeV

The differential cross section for the two transitions through the excited state at 4.445 MeV can be seen in Table 4.4. We observe that the primary transition decreases as the

E_{cm} (MeV)	$d\sigma/d\Omega_{4.445MeV->g.s.}$ (μb)	$d\sigma/d\Omega_{DC->4.445MeV}$ (μb)
1.77	1.06 ±0.31	0.32 ±0.12
1.72	0.88 ± 0.25	0.45 ± 0.15
1.62	0.71 ± 0.21	0.40 ± 0.14

TABLE 4.4: Differential cross section for the transition through the excited state at 4.445 MeV in μb. The first column is the secondary transition between the excited state at 4.445 MeV and the ground state, the second column is for the primary transition between the direct capture and the state at 4.445 MeV.

energy increases and the opposite phenomenon for the secondary transition. This is due to the contamination of the secondary transition by a γ-ray coming from ^{12}C, see Sec. 4.1.4.1. Therefore, the differential cross section of this cascade is the one in the second column. At higher beam energies, we did not observe anymore γ-ray coming from the primary transition. The contribution from this transition to the differential cross section was added to the total cross section as a tale from the resonance at $E_{cm} = 607$ keV.

4.2.3 From differential to total cross section

The R-matrix and A-matrix theory software *Azure* [78] was used to extract the total cross section from our measurements due to its ability to constrain the total cross section using other measurements, namely measurements of the exit channels of $^7Li + \alpha$. Despite the lack of angular distribution measurements available for this cross section, or the fact that there is no information on the mixing of the different transitions and the proximity of the resonances at $E_{beam} = 1.59$ MeV and $E_{beam} = 1.66$ MeV which might lead to interference (constructive or destructive), there is a lot of measurements available that would constraint the R-matrix. The R-matrix theory and A-matrix theory allows one to take into account the other cross sections and angular distribution measurements from the $^7Li + \alpha$ reaction. The more input measurements that are available, the more constraints exist on the different exit channels of the reaction. The information known from previous works will be used, see Chapter 2. Below, we present a summary of the R-matrix and the A-matrix theory, a complete description of the theory is beyond the scope of this thesis and can be found in [79]. Our results will then be presented.

4.2.3.1 *A*-matrix theory

The A-matrix theory that we used in our analysis is a development of the R-matrix theory. In this section, we will summarize the R-matrix theory and then the A-matrix theory because it is based on the same ideas as the R-matrix theory.

The *R*-matrix theory

The R-matrix theory is a phenomenological nuclear reaction theory. The interaction between projectile and target happens within a certain radius, namely the channel radius a_c. The interaction itself takes place in the internal region and is described with a complete set of eigenstates from the projectile and the target. The R-matrix theory connects the external region of states from the compound nucleus to the internal region using the channel radius, the spins, parities and energies of the entrance channel and compound nucleus, as well as the available experimental data for the exit channels.

The more experimental data and parameters on the different exit channels are known, the more it will constrain the "reaction black box" because it will constrain the different widths used in the R matrix. As an example, the different inputs used for $^7Li(\alpha,\gamma)^{11}B$ are presented in Fig. 4.16.

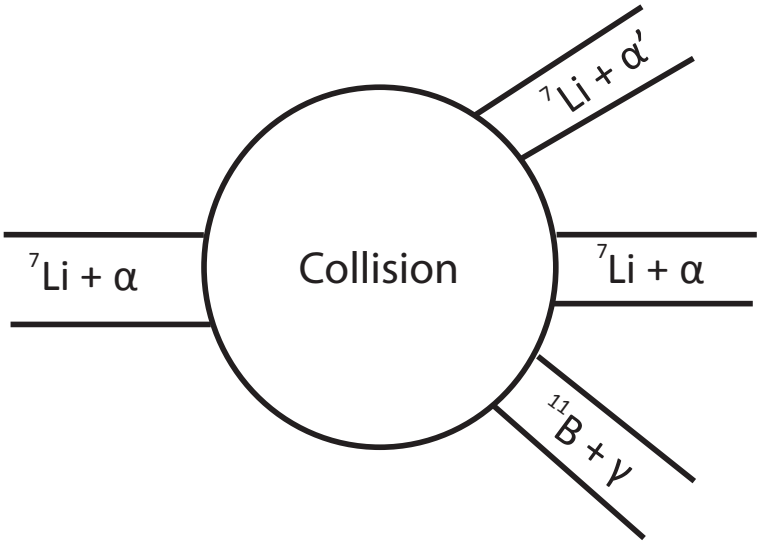

FIGURE 4.16: Schematic of the reaction $^7Li+\alpha$ seen by the R-matrix theory. The reaction happens in the internal region and is constrained by the accessible channels described in the external region.

The matrix **R** is defined as:

$$\mathbf{R} = \sum_c \frac{\gamma_{c\lambda}^2}{E_\lambda - E} \text{ with } \Gamma_{c\lambda} = \frac{2\gamma_{c\lambda}^2 P(E)}{(1 + \gamma_{c\lambda}^2 \frac{dS(E)}{dE})} \tag{4.6}$$

where the energy is $E = E_{cm}$+Q-value where E_{cm} is the beam energy in the center of mass, $\Gamma_{c\lambda}$ is the width of a specific level λ of a particular channel c defined, $\gamma_{c\lambda}^2$ is the associated reduced width and $P(E)$ the penetrability at energy E and $\frac{dS(E)}{dE}$ the derivative of the shift function. The **R**-matrix links the eigenstates of the compound nucleus to the measurable quantities such as the cross section and the resonance width.

A-matrix theory

The A-matrix was defined to provide an easier way to do R-matrix analysis for nuclei with many channels and few levels. The matrix **A** is defined as:

$$(A^{-1})_{\lambda\lambda'} = (E_\lambda - E)\delta_{\lambda\lambda'} - \sum_c \gamma_{\lambda c}\gamma_{\lambda' c}(S_c - B_c) - \frac{i\Gamma_{\lambda\lambda'}}{2}$$

where **S** is a shift matrix, **B** represents the boundary conditions, $\Gamma_{\lambda\lambda'}$ is the state width and $\gamma_{\lambda c}$ is the reduced channel width.

In this analysis, the A-matrix formalism was used to extract the angle integrated cross section from the differential cross section.

For any channel, particle or photon, the link between the matrix **A** and the total cross section is always through the transition matrix, such as:

$$\sigma = \frac{\pi}{k^2} \sum \frac{2J+1}{(2j_0+1)(2j_1+1)} |\mathbf{T}(\mathbf{A})|^2$$

where k is the wave number associated with the incoming particle pair, j_0 and j_1 are the spins of the target and projectile respectively, **T** is the transition matrix which is a function of the matrix **A**. The transition matrix will change depending on whether the ejectile is a photon, a charged particle or a neutron. Indeed, photons cannot be treated as particles because of their different electromagnetic properties.

A series of background poles are always added to an R-matrix analysis. They are high energy excited states with different spins and parities to mock up the higher energy excited states.

4.2.3.2 *A*-matrix results

The goal of our A-matrix analysis was to determine the total cross section that would fit, simultaneously, most of the data sets available for the $^7Li + \alpha$ reaction:

- The $^7Li(\alpha, \gamma)$ differential cross section of Paul et al. [1].
- The $^7Li(\alpha, \gamma)$ differential cross section of two transitions from this work.
- The $^7Li(\alpha, \alpha')$ cross section measurement of Paul et al. [1].
- The $^7Li(\alpha, \alpha')$ angular distribution of Cusson [55].
- The $^7Li(\alpha, \alpha)$ cross section measurement of Yamaguchi et al. [59].
- The $^7Li(\alpha, \alpha)$ cross section measurement of Cusson [55].

We did not included the 3 data point at which we observe a transition through the state at 4.445 MeV but it was accounted for by adding the resonance at $E_{cm} = 0.61$ MeV in the A-matrix analysis. The γ-ray observed from the transition through the 4.445 MeV can be considered as the tail of the resonance at 0.61 MeV because their differential cross section is small, see Sec. 4.2.2.

Some of the disagreements between the different sets of experimental data were mentioned in Sec. 2.2.1 and 2.2.2.2. The A-matrix analysis puts into light more disagreement:

- The $^7Li(\alpha,\alpha)$ measurements by Cusson [55] and Yamaguchi et al. [59] are incompatible.
- The $^7Li(\alpha,\alpha')$ measurement of Paul et al. [1] and the angular distribution of this reaction by Cusson [55] at $E^{lab}_{beam} = 3.03$ MeV are incompatible. The other angular distribution in the energy range measured by [55] is not usable because the axis cannot be read.
- The $^7Li(\alpha,\alpha)$ measurement of Cusson [55] and the $^7Li(\alpha,\gamma)$ measurement of Paul et al. [1] seem to be incompatible.
- Our measurement of the $^7Li(\alpha,\gamma)$ differential cross section at 45° and the measurement of Paul et al. [1] at 90° are incompatible.

These conflicts arose from the A-matrix analysis. In Fig. 4.17 the best fit of the data achieved, simultaneously, is shown. Aside from the total cross section of the $^7Li(\alpha,\alpha')$ measurement of Paul et al. [1] and the differential cross section of the cascade through the excited state at 5.02 MeV from our measurement, the fits are not good.

The agreement of the $^7Li(\alpha,\alpha')$ cross section by Paul et al. [1] with the other independent measurement of $^7Li(\alpha,\alpha')$ by Bichsel and Bonner [60] caused us to include the measurement of Paul et al. [1] in all our A-matrix analysis.

From the fit visible in Fig. 4.17, we attempted through different combinations of fits to deduce which sets of data were compatible. We rejected the measurement of [55]. The issue with the data set of Cusson [55] most likely comes from the detector system they used which had a 40 keV resolution. They used LiOH and LiF targets, and at the energy at which they measured the cross section and angular distribution, a number of other channels with high cross sections were open, for instance see Section 4.1.4.1.

We rejected the measurement of Yamaguchi et al. [59] because of our inability to fit their measurement with the inelastic scattering measurement of [1]. The detection system of [59] had an energy resolution of 100 keV at low energy which could explain why we could not have it agree with the rest of the data available.

The disagreement between our measurement of the $^7Li(\alpha,\gamma)^{11}B$ direct capture to ground state transition and the one of Paul et al. [1] could come from the difference of our respective energy resolutions. The way [1] corrected for target effects was questioned: did they use

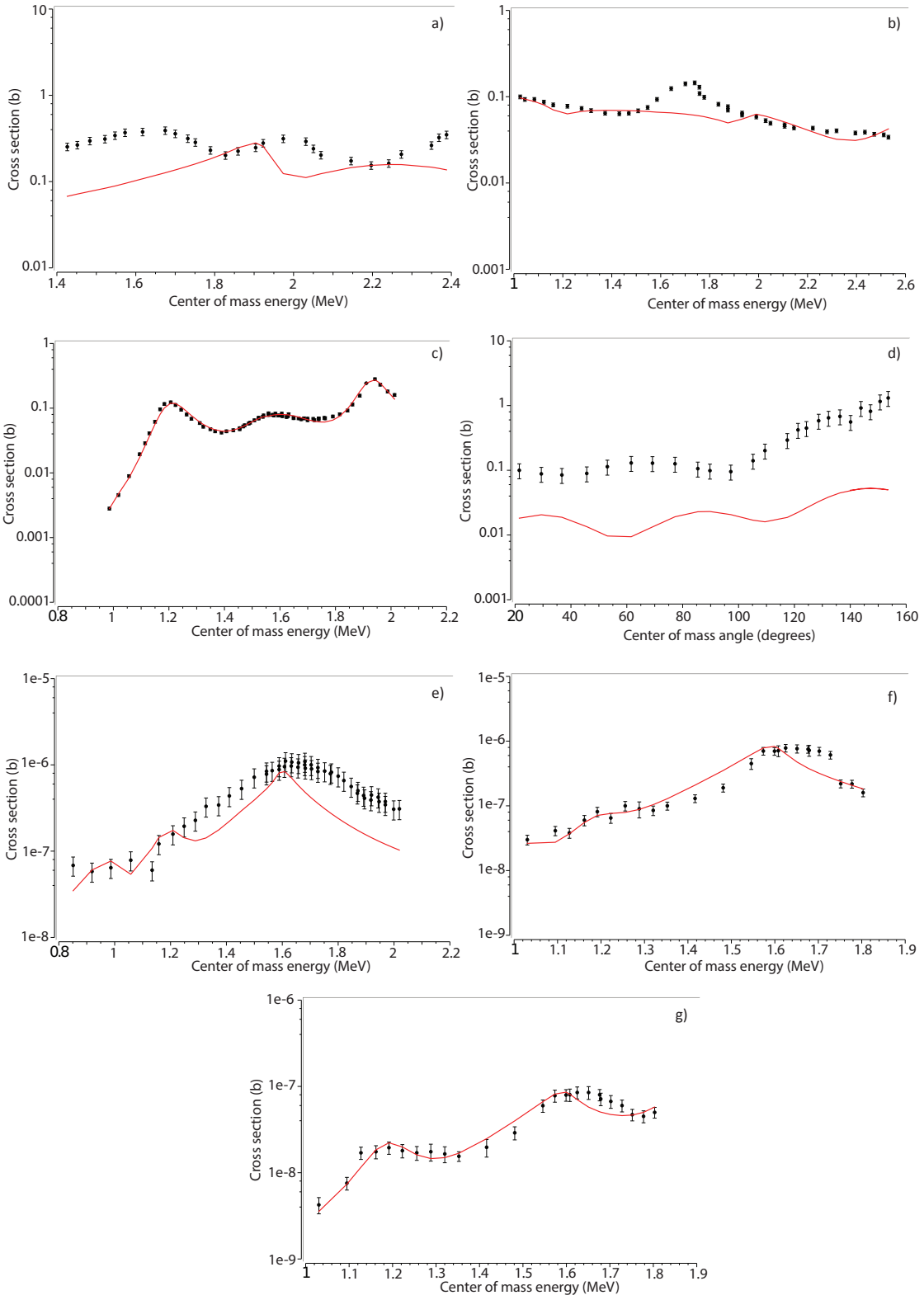

FIGURE 4.17: Simultaneous A-matrix fits of the data sets available. The data are the black dots and the fit is the solid red line.
a) is the $^7Li(\alpha,\alpha)$ differential cross section measured at 180° of [59].
b) The $^7Li(\alpha,\alpha)$ total cross section measured by [55].
c) The $^7Li(\alpha,\alpha')$ total cross section measured by [1].
d) The $^7Li(\alpha,\alpha')$ angular distribution at 3 MeV measured by [55].
e) The $^7Li(\alpha,\gamma)$ differential cross section measured at 90° of [1].
f) The $^7Li(\alpha,\gamma)$ differential cross section of the $DC \rightarrow g.s.$ transition measured at 45° of this work.
g) The $^7Li(\alpha,\gamma)$ differential cross section of the transition through the excited state at 5.02 MeV measured at 45° of this work.

the thin target approximation and was it valid for them to do so? All our efforts to identify whether the thin target approximation was valid on their data showed that it was.

As pointed out in Chapter 2, both Paul and Cusson did not obtain a good fit of their data using the A-matrix theory and both introduced new excited states to obtain better agreement. The new state at $E_{ex} = 9.82$ MeV discovered by Van Der Steenhoven et al. [48] is not sufficient to explain the disagreement between Paul et al. [1] and Cusson [55].

Because of these incompatibilities, we extracted the total cross section from our measurement at 45° and from Paul's measurements at 90° separately. To add constraints on the fit we used the measurement of the $^7Li(\alpha,\alpha')$ cross section by Paul et al. [1] because it agrees with the other independent measurement of $^7Li(\alpha,\alpha')$ by Bichsel and Bonner [60]. The data sets used for each fit can be seen in Table 4.5 and the results of the two fits can be seen in Fig. 4.18.

Data set	Fit 1	Fit 2
$^7Li(\alpha,\gamma)$ differential cross section at 90° [1]		√
$^7Li(\alpha,\gamma)$ differential cross section at 45° $(DC \rightarrow g.s.)^\star$	√	
$^7Li(\alpha,\gamma)$ differential cross section at 45° (cascade)*	√	
$^7Li(\alpha,\alpha')$ total cross section [1]	√	√
$^7Li(\alpha,\alpha')$ angular distribution at 3 MeV [55]		
$^7Li(\alpha,\alpha)$ differential cross section at 180° [59]		
$^7Li(\alpha,\alpha)$ total cross section [55]		

TABLE 4.5: Summary of data set used in the R-matrix fit. The symbol √ means the data set was used.The symbol $\star$ is used for the measurement of this work.

For each fit, background poles were added to the A-matrix at an energy of 20 MeV. States with the parity +1 and -1 were created at this energy for each spin represented in the levels of ^{11}B used in the fits.

The results of the fits are available in Table 4.6 and Table 4.7. The uncertainties were obtained using the Minuit processor MINOS [80].

The partial width Γ_γ can be estimated from the transition probabilities. The Weisskopf estimates which describe the transition probabilities are commonly used as the Wigner limit for Γ_γ. It has been shown that the Weisskopf estimates are often several order of magnitude larger than the experimentally measured width. The partial widths Γ_γ are physical parameters only if they are less than $\lambda_W\hbar$, the Weisskopf estimates, in eV, for the

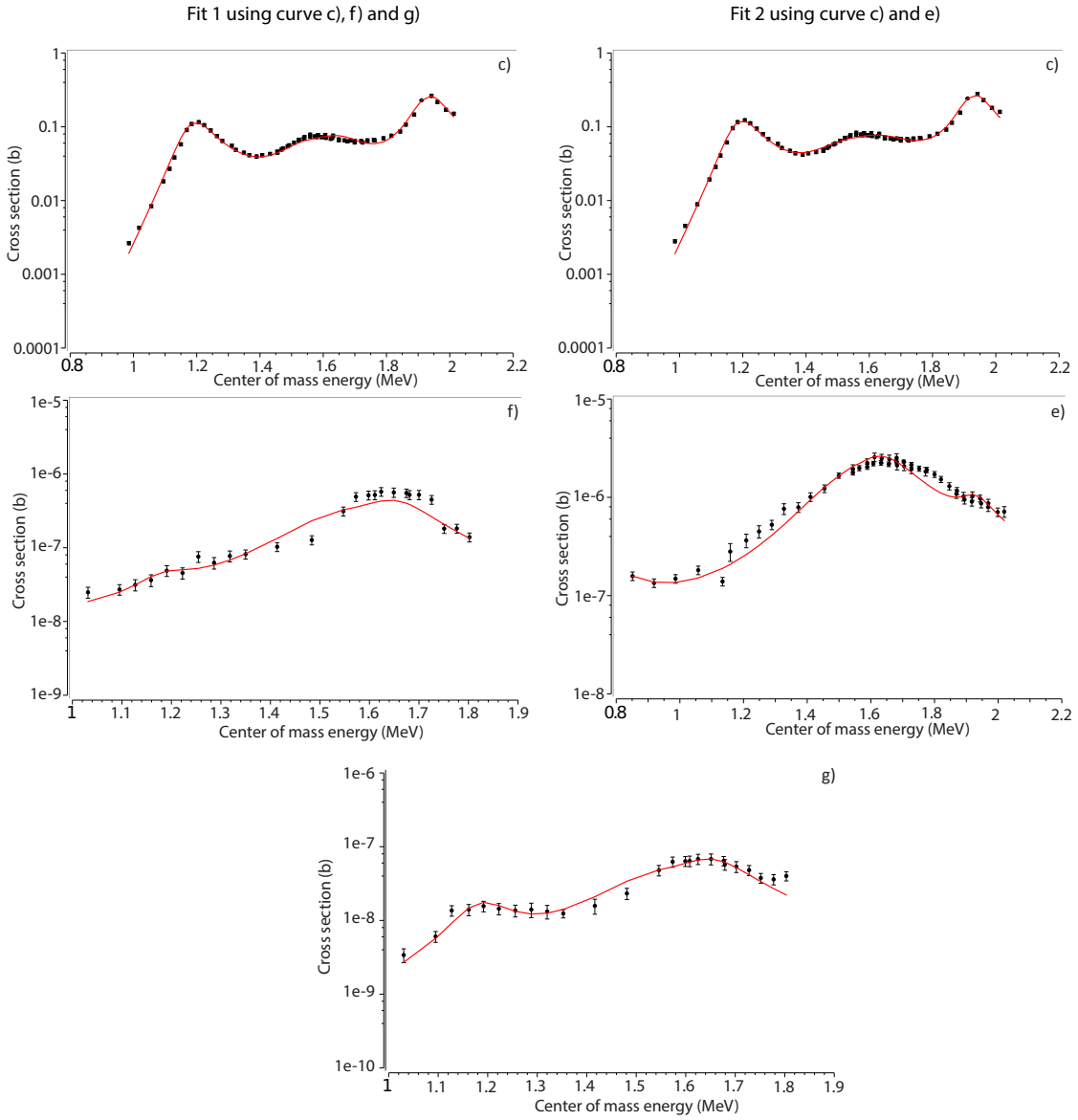

FIGURE 4.18: Simultaneous A-matrix fits of data from this work and the work of [1]. The data are the black dots and the fit is the solid red line. For clarity the letters associated with a particular data set in Fig. 4.17 were kept.
c) The $^7Li(\alpha,\alpha')$ total cross section measured by [1].
e) The $^7Li(\alpha,\gamma)$ differential cross section measured at 90° of [1].
f) The $^7Li(\alpha,\gamma)$ differential cross section of the $DC \rightarrow g.s.$ transition measured at 45° of this work.
g) The $^7Li(\alpha,\gamma)$ differential cross section of the transition through the excited state at 5.02 MeV measured at 45° of this work.

γ transition:

$$\begin{aligned}\lambda_W(E1)\hbar =& 6.8 \times 10^{-2} A^{2/3} E_\gamma^3 \\ \lambda_W(M1)\hbar =& 2.1 \times 10^{-2} E_\gamma^3\end{aligned} \tag{4.7}$$

where E_γ is the energy, in MeV, of the γ-ray emitted from a level to another one in the compound nucleus and $\hbar$ the reduced Planck constant. Wigner and Eisenbud [81] and Dover et al. [82] show that there is an upper limit to the reduced width and there is a Wigner limit for each single resonance. Then, the particle widths are physical if they are less than the Wigner limit:

$$\gamma_W^2 = \frac{3\hbar^2}{2m_{01}a_c^2} \tag{4.8}$$

where m_{01} is the reduced mass of the target and projectile, and a_c the channel radius.

E_{ex} (keV)	$\Gamma_\alpha\Gamma_{\alpha'}$ (MeV)	Γ_α (eV)	Γ_γ (Res$\rightarrow g.s$)	Γ_γ (Res$\rightarrow$ 5.02 MeV)
10602	$1284.8^{4.4\%}_{4.4\%}$			
10330	$1387.5^{2\%}_{2.1\%}$		23.14*	3.14*
10262	$9454.3^{2.2\%}_{2.3\%}$		19.68*	2.55*
9873	$5322.3^{2.5\%}_{2.6\%}$		$0.241^{+19.5\%}_{-18.5\%}$	$0.169^{+7.6\%}_{-7.7\%}$
9271.7		4000†	1.15†	

TABLE 4.6: Results of the A-matrix fit for this work with the $^7Li(\alpha,\alpha')$ measurement of Paul et al. [1]. Γ_α is the entrance channel width, $\Gamma_{\alpha'}$ is the exit channel width of the inelastic scattering and Γ_γ (i$\rightarrow f$) is the contribution to the exit channel width for the radiative capture. The channel radius is $a_c = 8$ fm.
* fixed to the Weisskopf estimates, see text for explanation.
† fixed to best known value from [5].

To fit our measurement (Table 4.6, see Fit 1 in Table 4.5), the well known state and parameters of the $E_{cm} = 0.61$ MeV resonance were used and fixed to the value reported by Hardie et al. [5]. The width of the transition to the 5.02 MeV excited state was fixed for the resonance at $E_{cm} = 1.66$ MeV and $E_{cm} = 1.59$ MeV to the Weisskopf estimates because the fit was naturally going to a higher value. For the same reason, the width of the $DC/Res \rightarrow g.s.$ transition was also fixed for these two resonances. This shows a lack of experimental constraint in our A-matrix analysis and the necessity for further measurements of the $^7Li(\alpha,\gamma)^{11}B$ reaction.

The Γ_α were all fixed in order to determine the uncertainty, because they are being deduced from the $^7Li(\alpha,\alpha')$ reaction cross section ($\Gamma_\alpha\Gamma_{\alpha'} \propto \sigma_{\alpha\alpha'}$) and are therefore highly correlated

to $\Gamma_{\alpha'}$. The Γ_α and $\Gamma_{\alpha'}$ were,however, free parameters while performing the fit and fixed at the value found during the fit when calculating the uncertainty. Thus, we present in Table 4.6 a new evaluation of $\Gamma_\alpha\Gamma_{\alpha'}$ and its uncertainty.

In order to fit the data of Paul et al. [1] (see fit 2 in Table 4.5), the parameters of the 0.61 MeV resonance were fixed, and because of correlations between the Γ_α and $\Gamma_{\alpha'}$ widths, Γ_α was fixed to calculate the uncertainty. However, the values of Γ_α and $\Gamma_{\alpha'}$ were free parameters while performing the fit and fixed at the value found during the fit. The results of the fit and the uncertainty, calculated with MINOS, are available in Table 4.7.

E_{ex} (keV)	$\Gamma_\alpha\Gamma_{\alpha'}$ (MeV)	Γ_α (eV)	Γ_γ (eV)	Γ°_{tot}	Γ^+_{tot} (keV)
10602	$1357.2^{3.5\%}_{3.5\%}$		$0.203^{+0.02\%}_{-0.02\%}$	75	90
10450					∼140
10330	$1951.1^{5.1\%}_{5.4\%}$		$20.54^{+5.7\%}_{-6.3\%}$	213	100
10262	$5315.8^{7.3\%}_{9.8\%}$		$8.1^{+14\%}_{-13\%}$	261	433
9873	$504.3^{2.5\%}_{2.6\%}$			45	290
9271.7		$4000^\dagger$	$1.15^\dagger$		

TABLE 4.7: Results of the A-matrix fit of the work of Paul et al. [1] with their $^7Li(\alpha,\alpha')$ measurement. Γ_α is the entrance channel width, $\Gamma_{\alpha'}$ is the exit channel width of the inelastic scattering and Γ_γ is the contribution of the exit channel width, here, $DC/Res \rightarrow g.s.$. The channel radius is $a_c = 8$ fm.
$^\circ$ estimated from A matrix fit performed in this work.
$^+$ from Table III in [1].
† fixed to best known value from [5].

The last column of Table 4.7 reports the Γ_{tot} values of Paul et al. [1]. Their values are to be compared with the Γ_{tot} we estimated. The Γ_{tot} we provide is only an estimation because of the correlation between Γ_α and $\Gamma_{\alpha'}$ we are not able to provide a more accurate value. The value they found are larger than the one we estimate from our A-matrix analysis with the exception of the Γ_{tot} of the state at 10.33 MeV. The value Γ_{tot} associated with the state at 10.33 MeV is higher than the one Paul et al. [1] provide because they added a state at 10.45 MeV to be able to fit their data and we were able to fit them without adding this state. If we consider the two Γ_{tot} of the state at 10.33 MeV and 10.45 MeV from their publication, it is higher than what we found for the state at 10.33 MeV like the other Γ_{tot} we provide. The values are smaller most likely due to the fact that we scaled down their differential cross section, see Sec. 2.2.2.2.

Usually, the channel radius is close to $a_c = 1.2A^{1/3}$ fm which in our case gives $a_c = 2.5$ fm. In comparison, the fits using our data and the data of [1] have a larger channel radius of 8 fm. It is probably due to the fact that our A-matrix analysis does not have enough experimental data: we only use a total cross section of the $^7Li(\alpha,\alpha')$ reaction and

differential cross sections at only one angle for each analysis (45° or 90°). The background poles and the channel radius are heavily correlated and might also have a role in the large a_c. This means that we may need additional background poles to the ones already included in the analysis.

We can see in Table 4.6 that our best estimate for the Γ_γ are the Weisskopf estimates which are only rough estimates. The Fit of Paul et al. [1] seems better only because there was even less data used to fit their measurement. This shows the necessity to measure an angular distribution of the $^7Li(\alpha,\gamma)$ reaction. In this analysis, we were only able to constraint the product $\Gamma_\alpha\Gamma_{\alpha'}$ because the $^7Li(\alpha,\alpha)$ measurements are incompatible. Therefore a new measurement of the $^7Li(\alpha,\alpha)$ reaction total cross section would be helpful to constraint future **A**-matrix analysis.

4.2.4 Total cross section

From the two fits, we get two total cross sections: one for the scaled data of Paul et al. [1] and one for the data measured in this work. They can be seen in Fig. 4.19. The incompatibility of the data explains the disagreement of the two total cross sections. This disagreement could be an interplay of several differences in our setups: our better energy resolution, maybe they used a thin target approximation to correct for the target effect, maybe they had random or coincidence summing that was not accounted for. Only one or none of these cross sections is physical, however all our efforts were not conclusive in ruling out our measurement or the corrected work of [1].

The yield of the resonance at $E_{cm} = 0.61$ MeV from our measurement was calculated and compared with the yield calculated using the parameters of Hardie et al. [5] with:

$$Y(E_0) = \frac{\lambda_r^2}{2\pi}\frac{\omega\gamma}{SP(E_r)}\left[arctan\left(\frac{E_0 - E_r}{\Gamma/2}\right) - arctan\left(\frac{E_0 - E_r - \Delta E}{\Gamma/2}\right)\right] \tag{4.9}$$

where λ_r^2 is the De Broglie wavelength at the resonance energy, ΔE is the energy thickness of the target in terms of energy loss, E_r is the resonance energy and E_0 is the energy at which the beam is estimated to be. We chose 965.45 keV which is on the plateau of our resonance scan. The yield we measured, $Y_{measured} = 2.36 \times 10^{-10} \pm 7.1 \times 10^{-11}$, and the yield we calculated using the parameters determined by Hardie et al. [5], $Y_{calcuated} = 1.62 \times 10^{-10} \pm 1.62 \times 10^{-11}$, agree within uncertainty. This increases our confidence in our measurement at higher energy.

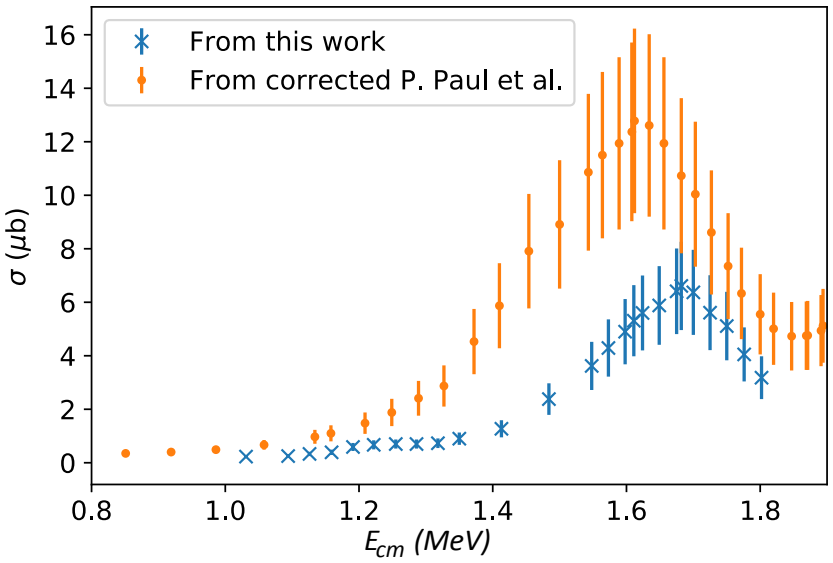

FIGURE 4.19: Total cross section as a function of the beam energy inferred from P. Paul's measurement at 90° and the measurement from this work at 45°.

The uncertainties on both of the total cross sections were estimated by fitting the inelastic scattering data from Paul et al. [1], the data from this work and the work of Paul et al. [1] that we scaled using the new measurement of the resonance strength by Hardie et al. [5] because [1] had scaled their differential cross section to a less acurate measurement of the resonance strength. The spins and parities of the excited states at 10.262 MeV and 10.330 MeV with J^π were changed with the spins and parities recommended by Cusson [55] and Paul et al. [1], see section 2.2, in order to determine the uncertainty on the cross section. Changing the spin and parity of these excited states changed the interference (constructive or destructive) between the different resonances and therefore affected the shape of the cross section. The total cross sections resulting from the change in J^π that were the furthest (highest and lowest) from the total cross section of this work with the adopted J^π of $\frac{3}{2}^-$ (10.262 MeV) and of $\frac{3}{2}^-$ (10.330 MeV) were used to define the uncertainties on both total cross sections.

4.2.5 Resonance strength

The resonance strength for each resonance was calculated using the parameters of the A-matrix fit, see Table 4.8.

The resonance strength is defined as:

$$\omega\gamma = \frac{(2J_R+1)(2\delta_{01}+1)}{(2j_0+1)(2j_1+1)}\frac{\Gamma_\alpha\Gamma_\gamma}{\Gamma_\alpha+\Gamma_\gamma} \tag{4.10}$$

where J_R, j_0, j_1 are the spin of the resonance, the spin of the target element and the spin of the beam element, respectively.

E_{cm} (MeV)	$\omega\gamma_{thiswork}$ (eV)	$\omega\gamma_{[1]}$ (eV)
1.94		0.202 ± 0.018
1.66	26.15 ± 4.5	20.5 ± 1.3
1.59	22.2 ± 3.8	8.1 ± 1.1
1.21	0.41 ± 0.06	

TABLE 4.8: Table of resonance strength for each resonance for our measurement and the measurement of Paul et al. [1].

A resonance strength at $E_{cm} = 1.94$ MeV cannot be extracted from our work because we did not go as high in energy as Paul et al. [1] did. There is no evidence in the data of Paul et al. [1] that a resonance is present at $E_{cm} = 1.21$ MeV because their energy resolution was not good enough to properly see it. The resonance strength of the resonance at $E_{cm} = 1.59$ MeV and $E_{cm} = 1.66$ MeV disagree for the two different set of data. Given that the two total cross section we calculated disagree this is not surprising but does show the necessity of a angular distribution measurement for the $^7Li(\alpha,\gamma)$ reaction.

4.2.6 Experimental astrophysical S-Factor

In nuclear astrophysics, it is common to work with the astrophysical S-factor. The astrophysical S-factor is the total cross section without the contribution of the s-wave Coulomb barrier transmission probability. It is defined as:

$$S = \sigma(E) \times E \times e^{-2\pi\eta} \text{ with } \eta = \frac{e^2 Z_0 Z_1}{\hbar}\sqrt{\frac{\frac{m_0+m_1}{m_0 m_1}}{2E_{cm}}} \tag{4.11}$$

where η is the Sommerfeld parameter.

The S-factor calculated for each energy is in Table 4.9 along with the total cross section from this work and the beam energy associated in the center of mass.

4.3 Reaction rate

Network reaction calculations in a given stellar environment require the reaction rate of reactions. The reaction rate takes into account the temperature at which the reaction happens as well as the probability of this interaction which includes the Coulomb barrier penetration. It is defined as:

E_{beam} (MeV)	$\sigma_{thiswork}$ (μb)	S-factor$_{thiswork}$ (keV.b)
1.031	0.23 ± 0.06	2.70 ± 0.69
1.094	0.25 ± 0.06	2.40 ± 0.61
1.126	0.33 ± 0.08	2.80 ± 0.71
1.159	0.39 ± 0.10	3.02 ± 0.77
1.191	0.59 ± 0.15	4.16 ± 1.06
1.222	0.67 ± 0.17	4.38 ± 1.13
1.255	0.70 ± 0.17	4.14 ± 1.05
1.286	0.70 ± 0.17	3.84 ± 0.99
1.318	0.73 ± 0.18	3.69 ± 0.94
1.350	0.90 ± 0.23	4.26 ± 1.08
1.413	1.27 ± 0.32	5.21 ± 1.32
1.484	2.38 ± 0.59	8.47 ± 2.15
1.548	3.62 ± 0.90	11.42 ± 2.90
1.573	4.29 ± 1.07	12.96 ± 3.29
1.598	4.90 ± 1.22	14.16 ± 3.59
1.611	5.31 ± 1.33	15.02 ± 3.87
1.624	5.60 ± 1.40	15.47 ± 3.93
1.649	5.88 ± 1.47	15.59 ± 3.96
1.675	6.41 ± 1.60	16.31 ± 4.14
1.682	6.61 ± 1.65	16.63 ± 4.22
1.700	6.37 ± 1.59	15.57 ± 3.95
1.725	5.61 ± 1.40	13.21 ± 3.35
1.750	5.11 ± 1.28	11.58 ± 2.94
1.776	4.05 ± 1.01	8.84 ± 2.27
1.802	3.18 ± 0.80	6.70 ± 1.70

TABLE 4.9: Table of the cross sections and S-factors calculated for each beam energy from this work.

$$\begin{aligned} N_A < \sigma v > &= \sqrt{\frac{8}{\pi m_{01}}} \frac{N_A}{(kT)^{3/2}} \int e^{-2\pi\eta} S(E) e^{-E/kT} dE \\ &= \sqrt{\frac{8}{\pi m_{01}}} \frac{N_A}{(kT)^{3/2}} \int E\sigma(E) e^{-E/kT} dE \end{aligned} \tag{4.12}$$

where N_A is the Avogadro number, T is the temperature in GK.

In this section the calculation of different reaction rates will be presented, first the narrow-resonance reaction rate, the broad-resonance reaction rate and finally the total reaction rate to be compared with the available reaction rate of Angulo et al. [2] (NACRE).

4.3.1 Narrow-resonance reaction rate

A narrow resonance is a resonance with a total width, Γ, less than a few keV. This can be used for the low-lying resonances at $E_{cm} = 0.61$ keV, $E_{cm} = 0.52$ keV and $E_{cm} = 0.26$ keV.

These resonance are also considered to be isolated.

The narrow resonance total cross section can be described using the Breit-Wigner cross section formula:

$$\sigma_{BW}(E) = \frac{\pi\hbar^2}{2m_{01}E}\frac{(2J+1)(1+\delta_{01})}{(2j_0+1)(2j_1+1)}\frac{\Gamma_\alpha\Gamma_\gamma}{(E_r-E)^2+\Gamma^2/4} \tag{4.13}$$

where J is the spin of the resonance, j_1 and j_2 are the spin of the target element and projectile respectively, E_r is the resonance energy and $E = E_{cm}$+Q-value, Γ_α and Γ_γ are the α and γ width for the resonance.

For a sufficiently narrow resonance, the total width, Γ, and the $e^{-E/kT}$ term in the reaction rate can be considered constant over the resonance with their value at E_r. Consequently, the reaction rate is obtained this way:

$$N_A < \sigma v >= N_A(\frac{2\pi}{m_{01}kT})^{3/2}\hbar^2 e^{-E_r/kt}\omega\gamma \tag{4.14}$$

where N_A is the Avogadro constant and k is the Boltzmann constant.

Each narrow-resonance contribution to the reaction rate was calculated individually, for the resonances at $E_{cm} = 0.61$ keV, $E_{cm} = 0.52$ keV and $E_{cm} = 0.26$ keV. We consider that the contribution of the transition through the excited state at 4.445 MeV we observe is accounted for by the narrow resonance at $E_{cm} = 0.61$ MeV. The resonance strengths used are listed in Table 4.10. The narrow-resonance contribution to the reaction rate is the sum

E_{cm}^{Res} (MeV)	$\omega\gamma$ (eV)
$0.26^\star$	0.31 ± 0.05
0.52^+	0.303 ± 0.026
$0.61^\star$	1.72 ± 0.17

TABLE 4.10: Resonance strength of the low-lying resonances used to calculate the reaction rate.
$\star$ Resonance strength measured by Hardie et al. [5].
$+$ Weigthed average of the resonance strengths measured by Hardie et al. [5] and Gyürky et al. [58].

of the contributions of these resonances. The results for the narrow-resonance contribution to the reaction rate can be seen in Table 4.11.

The uncertainty on the narrow resonances contribution to the reaction rate takes into account only the uncertainty of the resonance strength determined by Hardie et al. [5] and Gyürky et al. [58] of 10% each because it is much larger than the other uncertainties which

T_9 (MeV)	$N_A < \sigma v > (cm^3 mol^{-1} s^{-1})$
1	101.1 ± 10.7
1.25	253.7 ± 25.5
1.5	459.6 ± 45.4
1.75	685.1 ± 67.2
2	903.8 ± 88.3
2.5	1267.9 ± 123.4
3	1515.0 ± 147.2
3.5	1661.6 ± 161.4
4	1734.5 ± 168.4
5	1745.9 ± 169.4

TABLE 4.11: Total contribution to the reaction rate of the three resonances at $E_{cm} = 0.61$ keV, $E_{cm} = 0.52$ keV and $E_{cm} = 0.26$ keV using the resonance strength recommended by Hardie et al. [5] and Gyürky et al. [58].

contribute to the uncertainty on the narrow-resonant reaction rate (namely, the uncertainty on the masses and the energy).

4.3.2 Broad-resonance reaction rate

As opposed to a narrow resonance, a broad resonance is a resonance with a total width larger than a few keV. The cross section of a broad resonance varies slowly over the energy, and thus, the convolution of the cross section and the Maxwell-Boltzmann distribution needs to be integrated. Eq. 4.12 was used to calculate the broad resonance reaction rate.

The results of the integration for the broad resonance contribution to the reaction rate is available in Table 4.12.

T_9 (MeV)	$N_A < \sigma v >_1 (cm^3 mol^{-1} s^{-1})$	$N_A < \sigma v >_2 (cm^3 mol^{-1} s^{-1})$
1	14.7 ± 3.7	15.3 ± 4.1
1.25	47.2 ± 11.8	50.7 ± 13.7
1.5	99.9 ± 25.0	112.0 ± 30.2
1.75	168.5 ± 42.1	200.5 ± 54.1
2	249.4 ± 62.4	319.1 ± 86.2
2.5	442.9 ± 110.7	660.2 ± 178.2
3	674.8 ± 168.7	1143.3 ± 308.7
3.5	936.8 ± 234.2	1739.3 ± 469.6
4	1214.4 ± 303.6	2398.7 ± 647.6
5	1757.5 ± 439.4	3722.7 ± 1005.1

TABLE 4.12: Contribution to the rate of the 4 resonances at $E_{cm} = 1.2$ keV, $E_{cm} = 1.59$ keV, $E_{cm} = 1.66$ keV and $E_{cm} = 1.94$ keV using the cross sections calculated for this work ($N_A < \sigma v >_1$) and the corrected work of Paul et al. [1] ($N_A < \sigma v >_2$).

We measured the $DC/Res \rightarrow g.s.$ and the $DC/Res \rightarrow 5.02$ MeV transitions which include both the direct capture, outside the resonances, and the resonances component of the

cross section. Thus, the integration of the cross section which provides the reaction rate includes the contribution from the broad resonances and the non-resonant contribution in the experimental energy range.

The uncertainty on the broad resonances contribution to the reaction rate is principally affected by the uncertainty of the total cross section. The uncertainty on the total cross section was calculated by variation of the spins and the parities in *Azure*, see section 4.2.4. The total cross sections from our work and the corrected work of Paul et al. [1] have an uncertainty of 25% and 27 %, respectively. It is much larger than the other uncertainties which contribute to the uncertainty on the broad-resonant reaction rate (namely, the uncertainty on the masses $\sim 1/10^9$). The uncertainty was then calculated on the reaction rate using the propagation of uncertainty.

4.3.3 Results

In this section, the total reaction rate is calculated using the reaction rates calculated in the previous section:

$$N_A < \sigma v >= N_A < \sigma v >_{Narrow} + N_A < \sigma v >_{Broad+Non-resonant}$$

where $N_A < \sigma v >_{Narrow}$ is the reaction rate contribution from the narrow resonances and $N_A < \sigma v >_{Broad+Non-resonant}$ is the contribution of the reaction rate of the broad resonances and the non-resonant contribution. The reaction rates are calculated from independent measurement.

The total reaction rate from this work and from the measurement of Paul et al. [1] are plotted along with the NACRE [2] evaluation of the reaction rate and the NACRE II evaluation of the reaction rate [3] in Fig. 4.20. The NACRE [2] reaction rate evaluation used the measurement of Hardie et al. [5] for the low-lying resonances and the measurement from Paul et al. [1] for the high energy resonances. Based on the work of Descouvemont [62], they used the tail of the low-lying resonances to evaluate the non-resonant contribution. They also used the excited state at 10.45 MeV that was added by Paul et al. [1] to fit their data. The NACRE II reaction rate evaluation used the resonance strengths from Paul et al. [1] for the broad resonances with the exception of the excited state at 10.45 MeV that they did not included, and the resonance strength from Hardie et al. [5] and Gyürky et al. [58]

for the narrow resonances. They use a potential model to calculate the S-Factor and then the reaction rate.

All the reaction rates are in agreement if we consider the uncertainty, with the exception of the reaction rate we calculate with the data of [1] scaled and the reaction rate calculated by NACRE II [3].

The disagreement between the reaction rate we calculated using the corrected work of Paul et al. [1] and the evaluation of NACRE II[3] could be due to the poor R-matrix fit provided by [1]. The NACRE II reaction rate is also lower at low temperature. This is interesting because, as we will see in Sec. 4.3.3.1, the dominant contribution comes from the resonance at $E_{cm} = 0.61$ MeV and they use the same resonance strength as NACRE did and as we did. This can also explain the disagreement between the NACRE II evaluation and the reaction rate we calculate using the corrected data of Paul et al. [1].

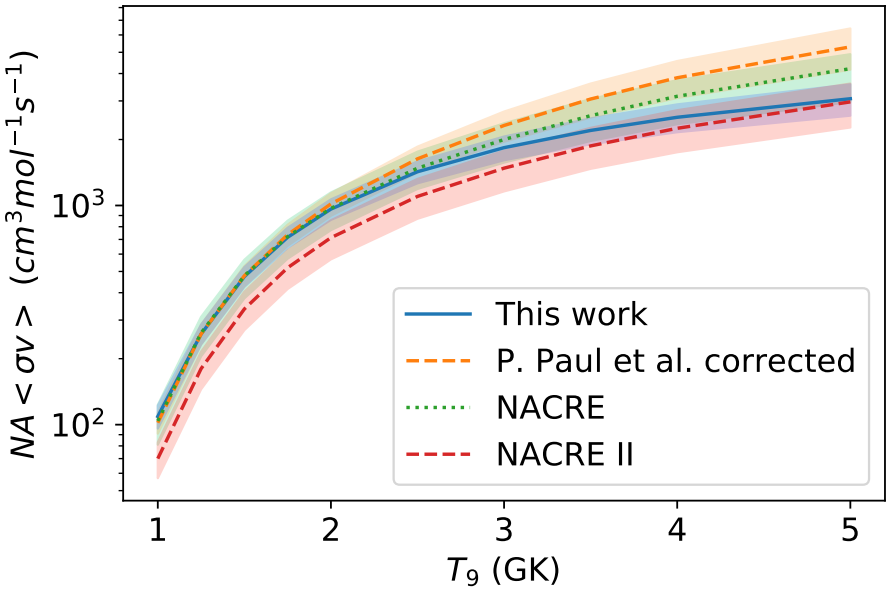

FIGURE 4.20: Total reaction rate calculated with the A-matrix output as a function of temperature in GK. The green doted line and the green band are the reaction rate from NACRE [2] and the associated uncertainty. The orange dashed line and the associated orange band are the reaction rate and the corresponding uncertainty from the corrected work of Paul et al. [1]. The blue line and band are the reaction rate from this work and its uncertainty. The red dashed line is the reaction rate from the evaluation of NACRE II [3] and the associated uncertainty is the red band.

The exact procedure that lead to the reaction rate published by NACRE [2] is unclear. In the internal report from the NACRE collaboration [83] they use a code not available publicly and are unclear as to what their code, *finira3*, does exactly. It seems like they use the Breit-Wigner cross section to calculate the reaction rate. However, in doing this, it is unclear how they determine Γ_{alpha}, $\Gamma_{\alpha'}$ and Γ_{γ} given that they only know the total

width and the resonance strength of the resonances. In the publication, they mention a multi-resonance approach with which they calculate the reaction rate (they do not mention this approach in the internal report), which would require to know Γ_{alpha}, $\Gamma_{\alpha'}$ and Γ_{γ}. We tried to reproduce these two approaches in Fig. 4.21: the first one, we tried to use a Breit-Wigner approach for all the resonances, it is the all Breit-Wigner approach in the orange dashed line and, we tried a multi-resonance approach in the blue line, the green dotted line is the adopted reaction rate published by NACRE [2]. To try to explain how they infer their reaction rate from the resonance strength and total width, we also tried to consider all resonances as a narrow resonance, in dashed red line in Fig. 4.21. We also imagined they could have used the differential cross section provided by Paul et al. [1] by mistake, this is plotted in the purple dotted line.

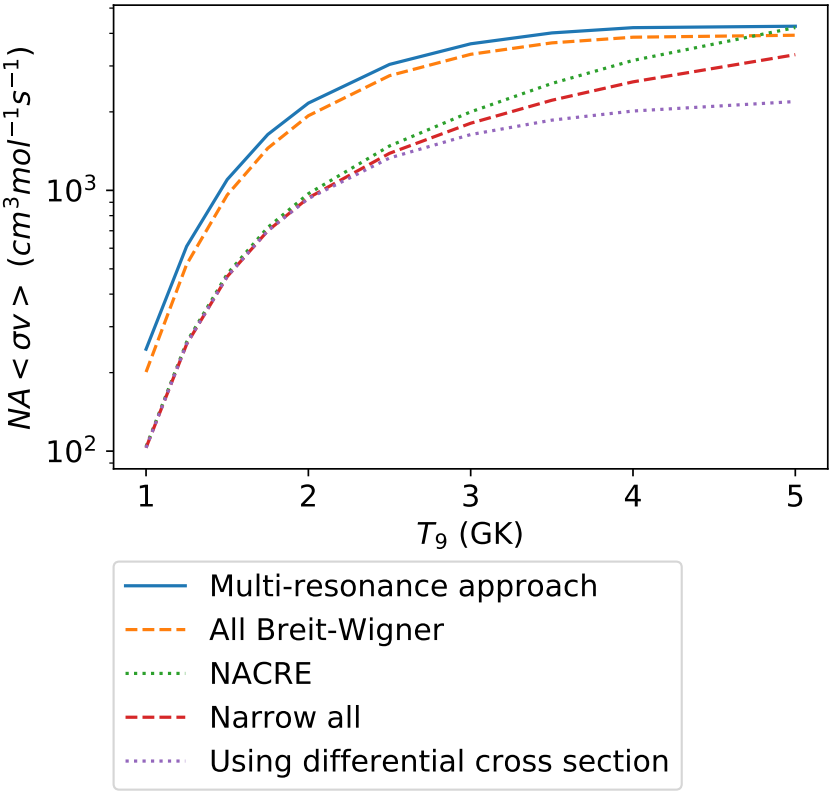

FIGURE 4.21: Reproducing the reaction rate published by NACRE: based on the publication and the internal report, we tried to reproduce their calculation using an all Breit-Wigner approach, a multi-resonance approach, a narrow resonance approach for all resonances and we also tried integrating the differential cross section, resp. in orange dashed line, blue line, red dashed line and purple dotted line. The reaction rate published by NACRE is represented by the green dotted line.

The interference between the different resonances in the range of temperature studied was investigated as well. Each resonance contribution to the reaction rate was calculated separately using *Azure* and the different sets of parameters we obtained from the two A-matrix

fits, see purple dotted line and red dashed line in Fig. 4.22. This is an evidence that some interference between the resonances are constructive.

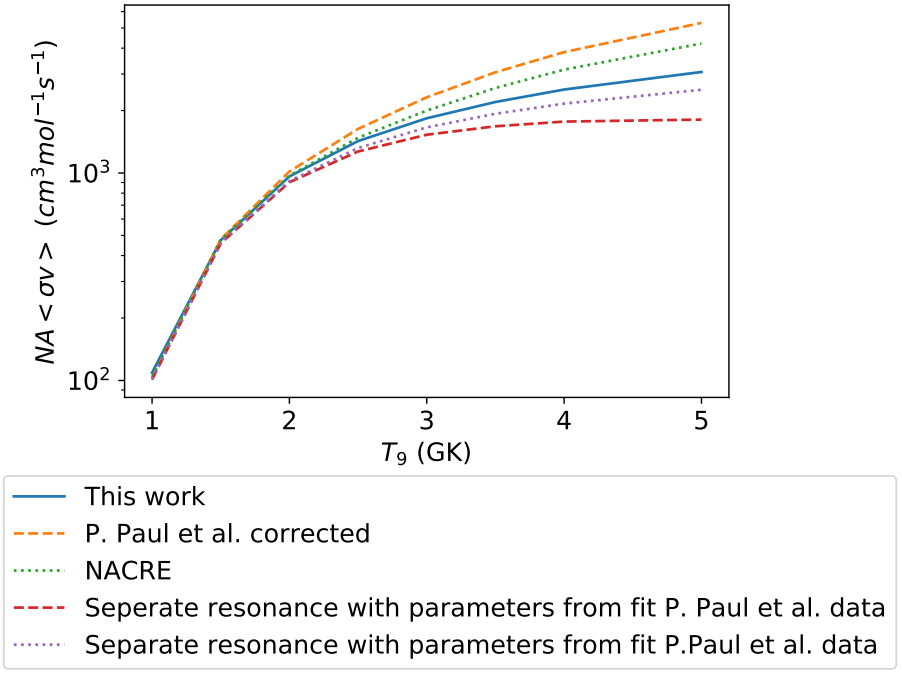

FIGURE 4.22: Role of interference in the reaction rate.

The total reaction rate from our work is within the uncertainty of the total reaction rate reported by NACRE [2] and it is low compared to the reaction rate from the corrected work of Paul et al. [1]. This is due to the fact that the cross sections calculated using the corrected work of Paul et al. [1] are higher than the one from the measurements of this work, see Fig. 4.19. The total reaction rate from our work is also low compared to the reaction rate evaluation from NACRE. It is possible that the non-resonant reaction rate calculated based on the work of Descouvemont [62] is overestimated. It could also be due to using a different mass evaluation to calculate the Q-value.

The uncertainty on the total reaction rate is the quadratic sum of the uncertainty of each contribution because the reaction rates are calculated from independent measurements. The uncertainties of each contribution were explained is the associated sections, Sec. 4.3.2 and Sec. 4.3.1.

4.3.3.1 Resonance contribution to the reaction rate

To estimate the contribution of the resonance to the reaction rate of the high energy resonances, the parameters of the A-matrix fit were used in the Breit-Wigner formula,

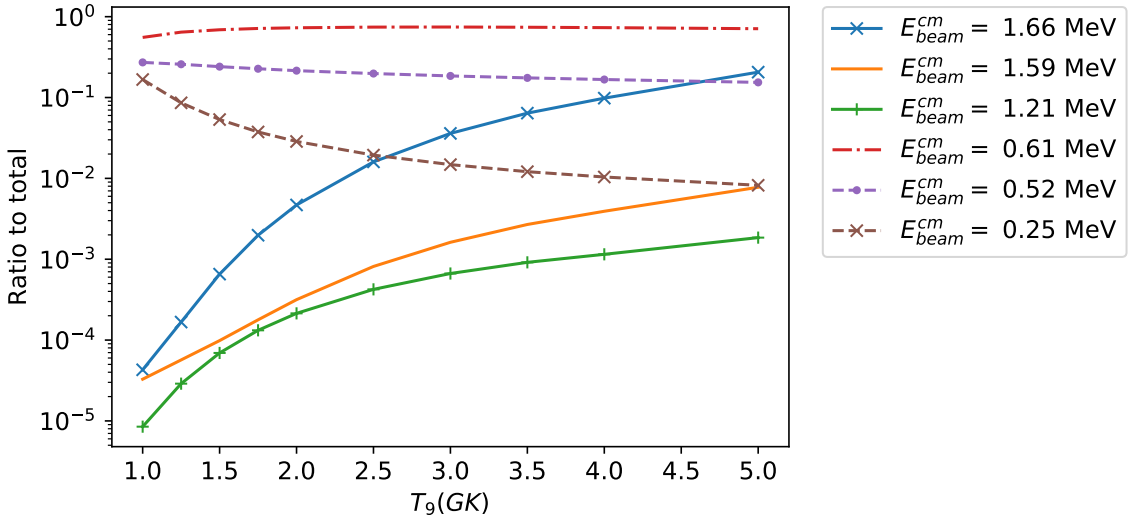

FIGURE 4.23: Contribution to the total reaction rate calculated using the cross sections from this work as a function of temperature in GK. The plain lines are for the broad resonances and the dashed lines are for the narrow resonances.

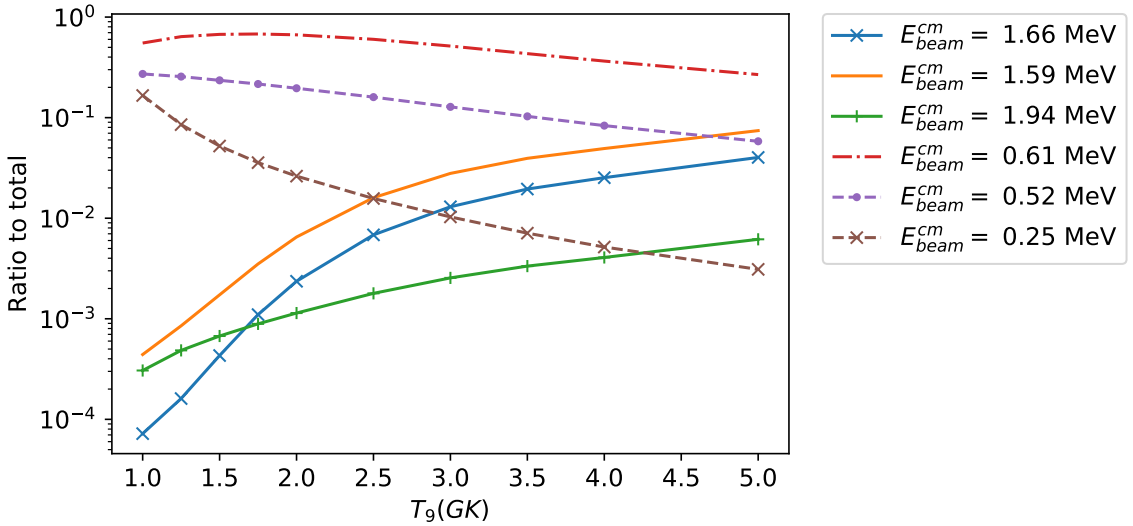

FIGURE 4.24: Contribution to the total reaction rate calculated using the cross sections from the work of P. Paul as a function of temperature in GK. The plain lines are for the broad resonances and the dashed lines are for the narrow resonances.

Eq. 4.13, and scaled to match the height of the total cross section from the A-matrix theory. The reaction rate was then calculated for each resonance individually using Eq. 4.13.

Fig 4.23 shows the different resonant contributions to the reaction rate as a function of temperature. The low-lying resonances, in dashed line, dominate the reaction rate. Above 3 GK, the contribution from the resonance at $E_{cm} = 1.59$ MeV becomes larger than the contribution of the $E_{cm} = 0.25$ MeV resonance.

Fig 4.24 shows the different resonant contributions to the reaction rate inferred from the work of Paul et al. [1] as a function of temperature. The low-lying resonances, in dashed line, dominate the reaction rate with the highest contribution being from the $E_{cm} = 0.61$ MeV resonance. Above 3 GK, the contribution of the resonances at $E_{cm} = 1.59$ MeV and $E_{cm} = 1.66$ MeV to the reaction rate becomes larger than the contribution of the $E_{cm} = 0.25$ MeV resonance.

By comparing Fig. 4.23 and Fig. 4.24, we note that the large total reaction rate inferred from the work of Paul et al. [1] is due to the contribution of the resonance at $E_{cm} = 1.66$ MeV. Indeed, the contribution from this resonance is larger in the reaction rate calculated from their work than it is in the reaction rate calculated from our work which is in agreement with the total cross section presented in Fig. 4.19. The contribution from the resonance at $E_{cm} = 1.94$ MeV, which was measured by Paul et al. [1] but not in our measurements, and the resonance at $E_{cm} = 1.21$ MeV which is nonexistent in the measurement of Paul et al. [1] have similar contributions in both reaction rates.

4.4 Summary

In this chapter we calculated the differential cross section from our experimental data and extracted the total cross section using the A-matrix theory. We showed that the corrected measurements of Paul et al. [1] and the measurements from our work are incompatible. We were not able to rule out either of the two measurements because of a certain lack of details in the publication of [1] and our ability to show that our measurement is compatible with the measurement of Hardie et al. [5]. Consequently, we deduced two reaction rates.

Both of the reaction rates inferred from this work and the work of P. Paul were compared with the reaction rate evaluations of NACRE [2] and NACRE II [3]. Both reaction rates, from the corrected work of Paul et al. [1] and ours, agree with NACRE [2]. The reaction rate inferred from our measurement agrees with the reaction rate from the NACRE II [3] evaluation but this is not the case for the reaction rate we calculated with the corrected work of Paul et al. [1]. The reaction rate reported by NACRE II [3] seems to be underestimated at low temperature even though they report using the same resonance strength, measured by Hardie et al. [5], for the dominant resonance at $E_{cm} = 0.61$ MeV as NACRE and we did. The reaction rate calculated with the corrected work of Paul et al. [1] is higher than the reaction rate calculated by NACRE and NACRE II and we were not able to fully

understand why. The difference between the two reaction rates we calculated lays in the resonance at $E_{cm} = 1.66$ MeV.

Chapter 5

Conclusion

We measured the differential cross section of $^{7}Li(\alpha,\gamma)^{11}B$ at 45° with helium beam energies between 1.6 and 2.8 MeV in the laboratory frame using a high purity germanium detector. This, by itself, adds a constraint on the cross section of this reaction because the only other measurement was performed at 90° with a sodium iodine detector. We also measured the cross section associated with a transition that was not seen before through the ^{11}B excited state at 5.02 MeV.

We corrected the measurement of Paul et al. [1] as it was relying on the scaling of their data based on a resonance strength from Jones et al. [56] that was later re-measured with better precision by Hardie et al. [5].

We identified disagreement between the $^{7}Li(\alpha,\alpha')$ cross section measurement of Cusson [55] and Paul et al. [1], and the disagreement between Paul et al. [1] and Yamaguchi et al. [59].

An A-matrix analysis was used in order to extract the total cross section, because of the interference between the resonances at $E_{cm} = 1.59$ MeV and $E_{cm} = 1.66$ MeV. The A-matrix analysis highlighted more disagreement between the different sets of experimental data.

We calculated separately cross sections from our measurement as well as the one from the corrected measurement of Paul et al. [1] because these two measurements are incompatible. We have evaluated in details our measurements and cannot provide a reason for the discrepancy. We also attempted to provide a source of error in the analysis of Paul et al. [1], but we were not able to demonstrate the validity of that interpretation.

From these two cross sections, we calculated the reaction rates associated with each measurement for this reaction at temperatures between 1 GK and 5 GK.

It is unclear where the reaction rate recommended by NACRE [2] and NACRE II [3] come from. We had access to an internal report of NACRE [2] and tried to reproduce their results without success. Despite this, the reaction rates, from the corrected work of Paul et al. [1] and from our work, both agree with the reaction rate provided by the NACRE compilation [2].

The reaction rate calculated from our work agrees with the reaction rate recommended by NACRE II [3], this is not the case for the reaction rate we calculated using the corrected work of Paul et al. [1]. The discrepancy between these reaction rates might be the consequence of an anomaly at low energy in the reaction rate recommended by NACRE II [3]: the resonance strength of the dominant resonance at this energy, namely the $E_{cm} = 607$ keV resonance, is the same for all the reaction rates presented in this thesis and NACRE II [3] does not match all other reaction rates calculated at low energy.

The measurement of the $^{7}Li(\alpha,\gamma)^{11}B$ cross section should be performed again with an array of shielded γ detectors in order to deduce the angular distribution, which is needed to fully constrain this total reaction cross section. Ideally, because the measurements of Cusson [55] and Yamaguchi et al. [59] disagree, the $^{7}Li(\alpha,\alpha)^{7}Li$ reaction, as well as its angular distribution, should be measured in order to get a better understanding of this reaction.

Appendix A

Run Summary

In this section, each run is summarized in Table A.1. For each run, two spectra are presented, one between 4 MeV and 6 MeV and one between 8.5 MeV and 11 MeV. Each run has a different amount of charge on target and a different target thickness (on average during the run). The average target thickness over the run is an average of the target estimated before and after the long run and was used to correct for target effects.

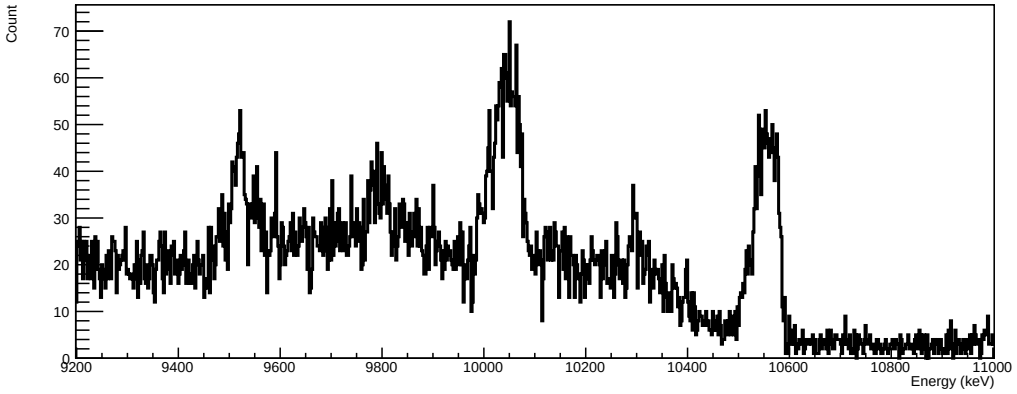

FIGURE A.1: Spectrum of a run at $E_{beam} = 2.83$ MeV between $E = 9.2$ MeV and $E = 11$ MeV.

Run #	E_{beam} (keV)	Charge	E_{loss} (keV)	Figures
163	2830.05 ±0.65	2.27×10^{18}	12.02 ±0.33	A.1 and A.2
164	2789.80 ±0.65	1.96×10^{18}	11.61 ±0.32	A.3 and A.4
166	2749.26 ±0.64	1.81×10^{18}	10.83 ±0.30	A.5 and A.6
213	2635.30 ±1.19	1.09×10^{18}	9.35 ±0.40	A.7 and A.8
215	2523.86 ±0.61	1.17×10^{18}	9.37 ±0.40	A.9 and A.10
216	2426.2 ±0.60	1.87×10^{18}	9.39 ±0.40	A.11 and A.12
257	2324.73 ±0.59	2.03×10^{18}	11.01 ±0.47	A.13 and A.14
259	2223.04 ±0.57	4.13×10^{18}	10.47 ±0.45	A.15 and A.16
261	2122.92 ±1.06	5.10×10^{18}	9.63 ±0.41	A.17 and A.18
329	2021.54 ±0.54	1.93×10^{18}	11.53 ±0.57	A.19 and A.20
375	1918.78 ±0.53	6.58×10^{17}	25.78 ±0.52	A.21 and A.22
377	1823.3 ±0.51	7.31×10^{17}	26.25 ±0.54	A.23 and A.24
380	1718.38 ±0.95	1.45×10^{18}	26.72 ±0.55	A.25 and A.26
382	1617.18 ±0.48	1.68×10^{18}	27.40 ±0.56	A.27 and A.28
387	2671.69 ±0.63	2.94×10^{17}	19.69 ±0.40	A.29 and A.30
389	2591.42 ±1.18	2.91×10^{17}	19.91 ±0.41	A.31 and A.32
391	2509.95 ±0.61	4.58×10^{17}	20.83 ±0.42	A.33 and A.34
393	2712.12 ±0.64	5.11×10^{17}	19.73 ±0.40	A.35 and A.36
395	2631.46 ±0.63	5.68×10^{17}	20.44 ±0.42	A.37 and A.38
397	2550.36 ±0.62	5.58×10^{17}	18.56 ±0.38	A.39 and A.40
399	2469.69 ±0.61	5.72×10^{17}	16.99 ±0.35	A.41 and A.42
402	2071.92±0.55	6.46×10^{17}	19.33 ±0.39	A.43 and A.44
404	1970.90±0.53	6.81×10^{17}	21.09 ±0.43	A.45 and A.46
407	1870.21±0.52	8.04×10^{17}	22.89 ±0.43	A.47 and A.48
410	1769.20±0.50	1.41×10^{18}	21.07 ±0.43	A.49 and A.50

TABLE A.1: Compilation of information about the runs with their number, beam energy, charge and the energy loss in the target at their particular beam energy.

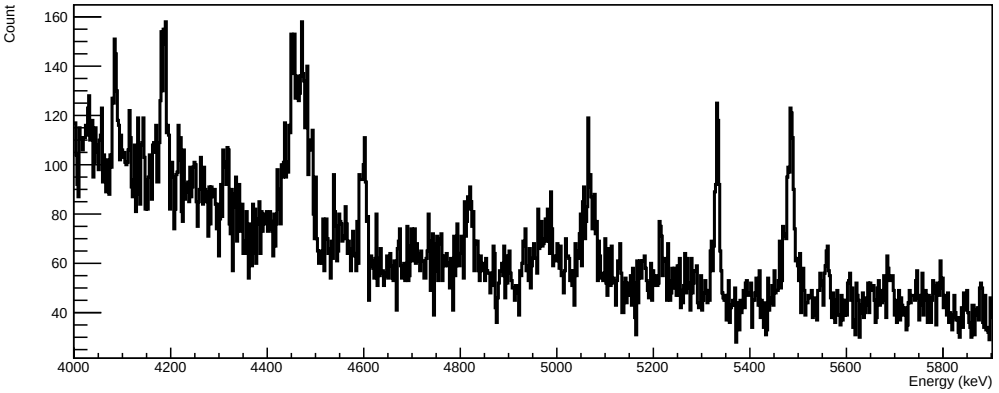

FIGURE A.2: Spectrum of a run at $E_{beam} = 2.83$ MeV between $E = 4$ MeV and $E = 6$ MeV.

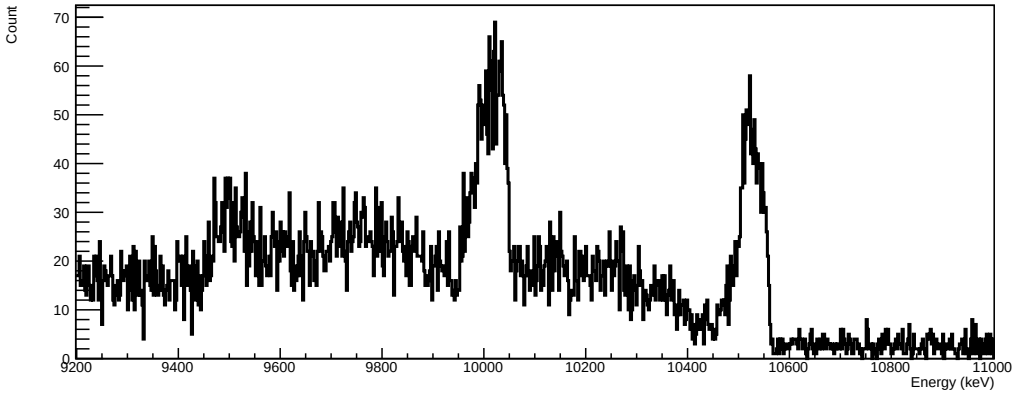

FIGURE A.3: Spectrum of a run at $E_{beam} = 2.79$ MeV between $E = 9.2$ and $E = 11$ MeV.

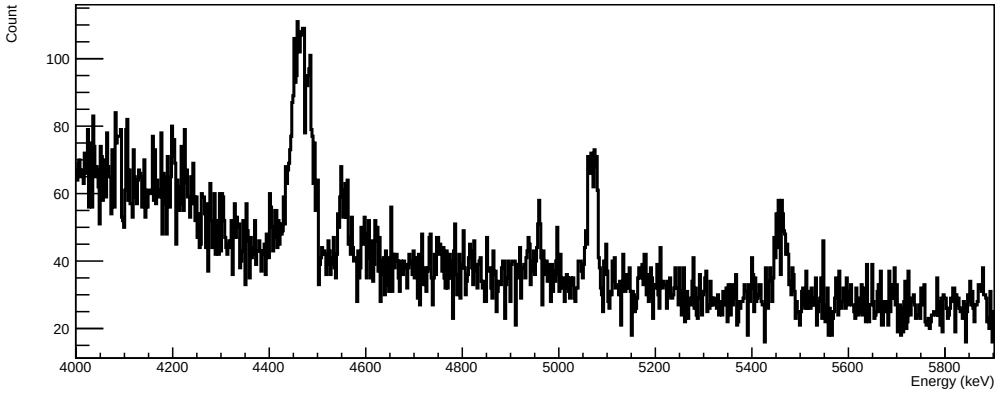

FIGURE A.4: Spectrum of a run at $E_{beam} = 2.79$ MeV between $E = 4$ MeV and $E = 6$ MeV.

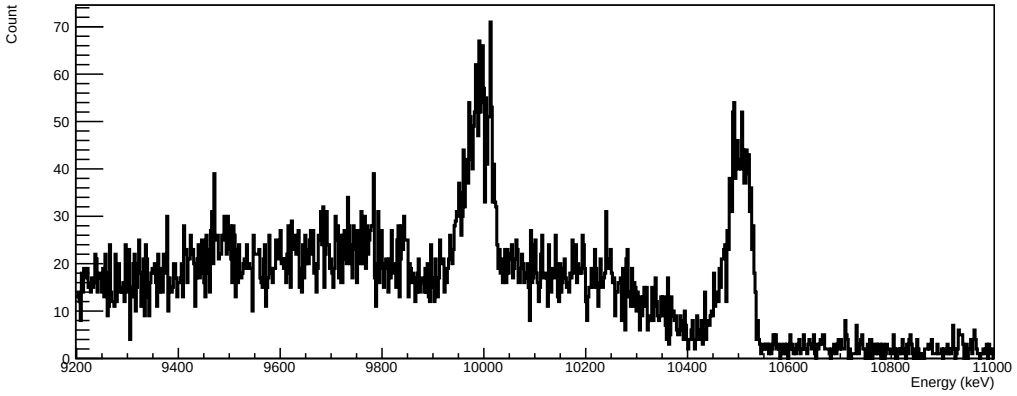

FIGURE A.5: Spectrum of run at $E_{beam} = 2.75$ MeV between $E = 9.2$ MeV and $E = 11$ MeV.

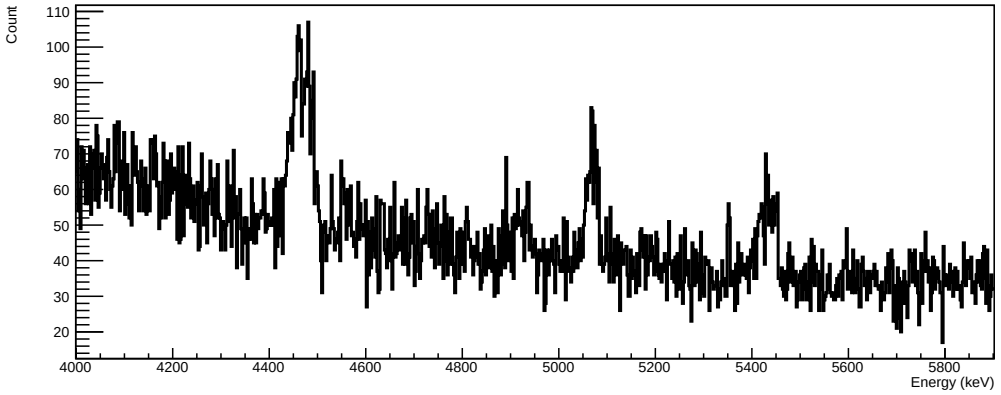

FIGURE A.6: Spectrum of run at $E_{beam} = 2.75$ MeV between $E = 4$ MeV and $E = 6$ MeV.

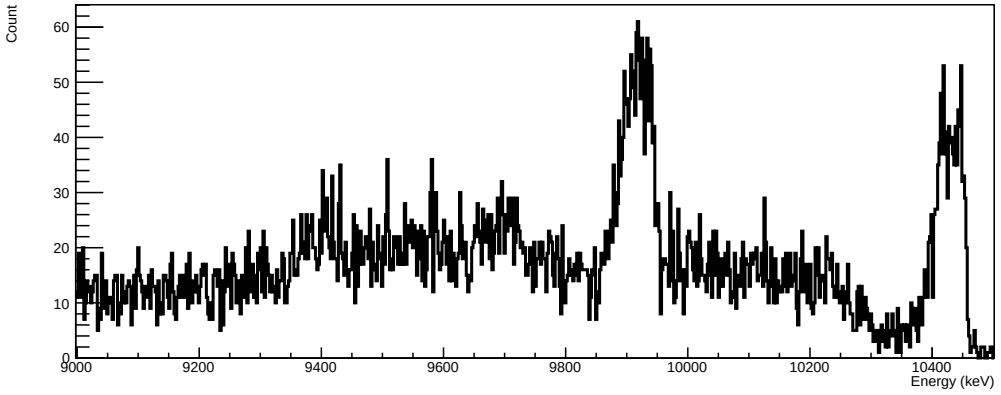

FIGURE A.7: Spectrum of run at $E_{beam} = 2.64$ MeV between $E = 9$ MeV and $E = 10.5$ MeV.

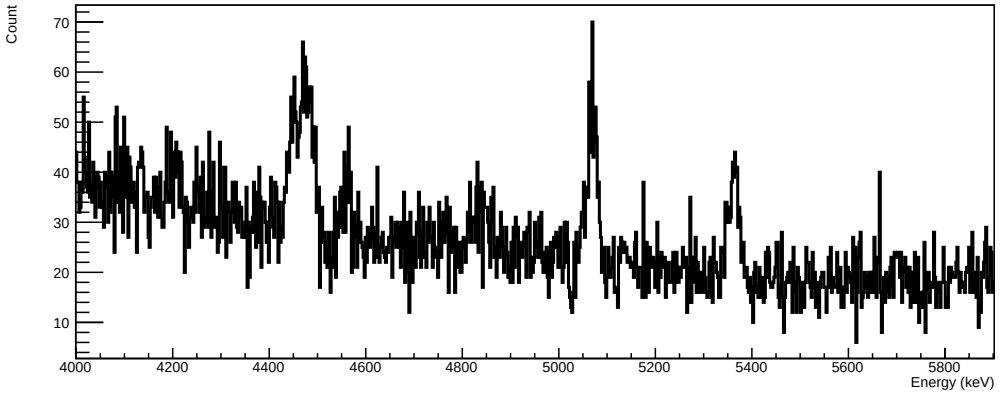

FIGURE A.8: Spectrum of run at $E_{beam} = 2.64$ MeV between $E = 4$ MeV and $E = 6$ MeV.

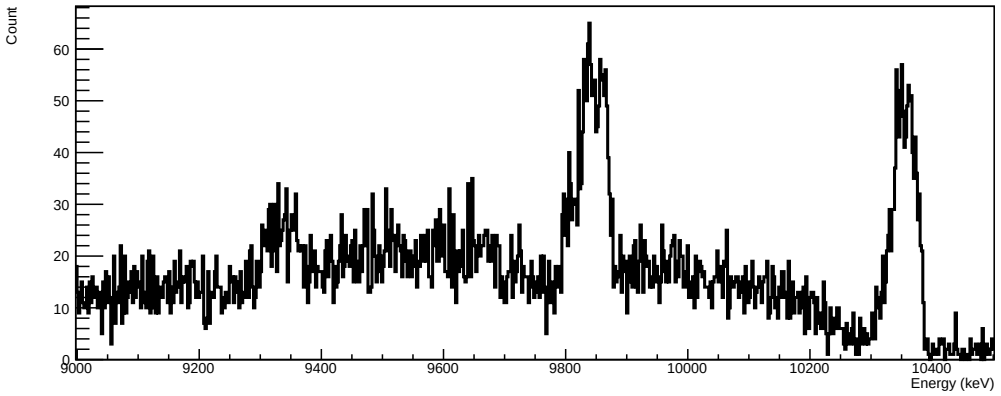

FIGURE A.9: Spectrum of run at $E_{beam} = 2.52$ MeV between $E = 9$ MeV and $E = 10.5$ MeV.

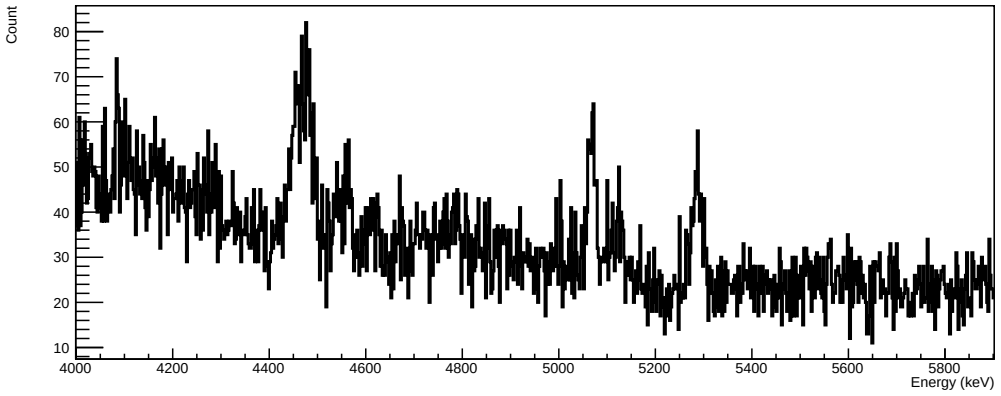

FIGURE A.10: Spectrum of run at $E_{beam} = 2.52$ MeV between $E = 4$ MeV and $E = 6$ MeV.

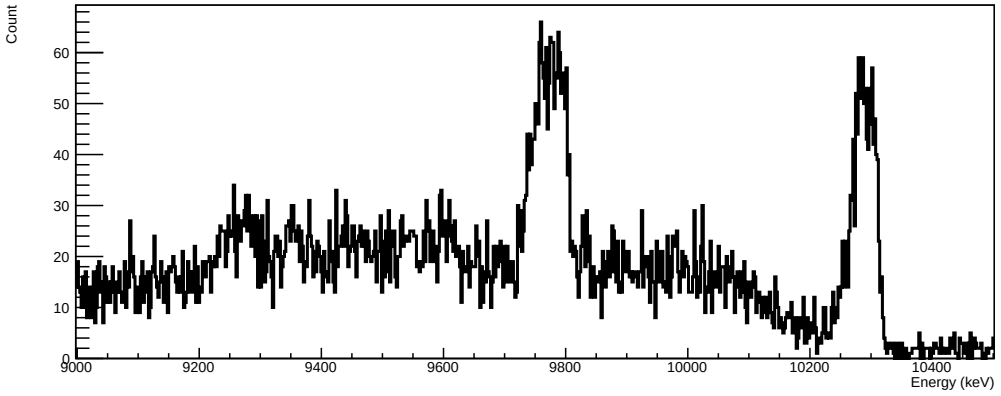

FIGURE A.11: Spectrum of run at $E_{beam} = 2.43$ MeV between $E = 9$ MeV and $E = 10.5$ MeV.

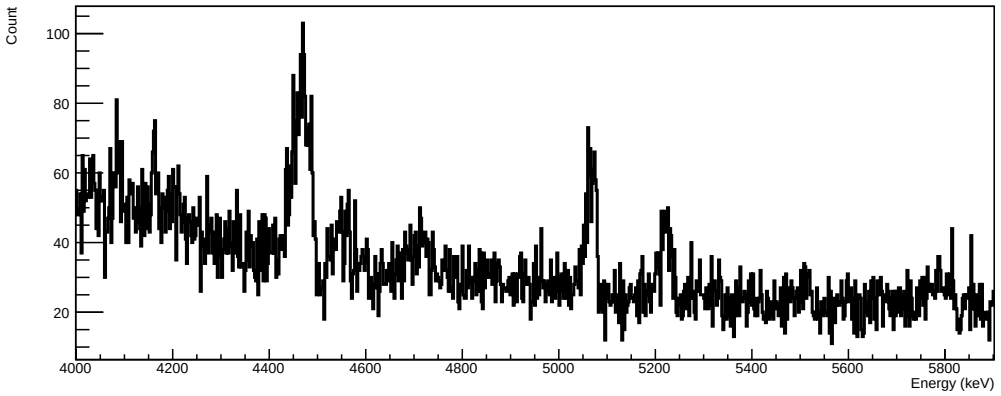

FIGURE A.12: Spectrum of run at $E_{beam} = 2.43$ MeV between $E = 4$ MeV and $E = 6$ MeV.

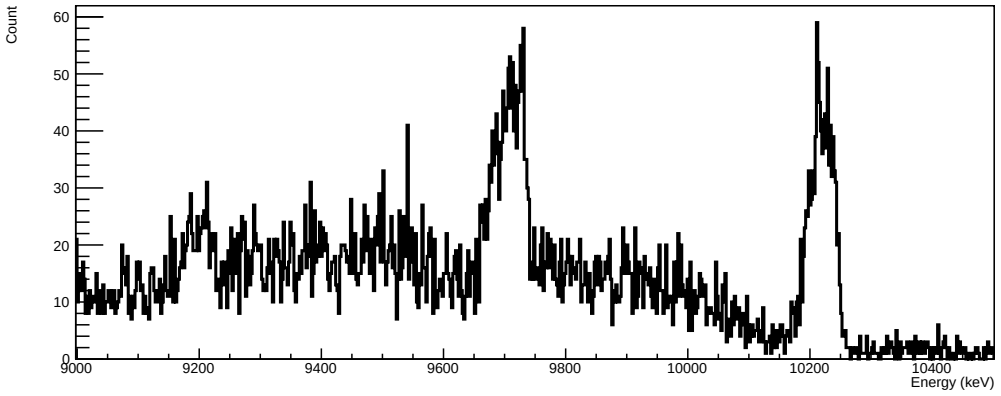

FIGURE A.13: Spectrum of run at $E_{beam} = 2.32$ MeV between $E = 9$ MeV and $E = 10.5$ MeV.

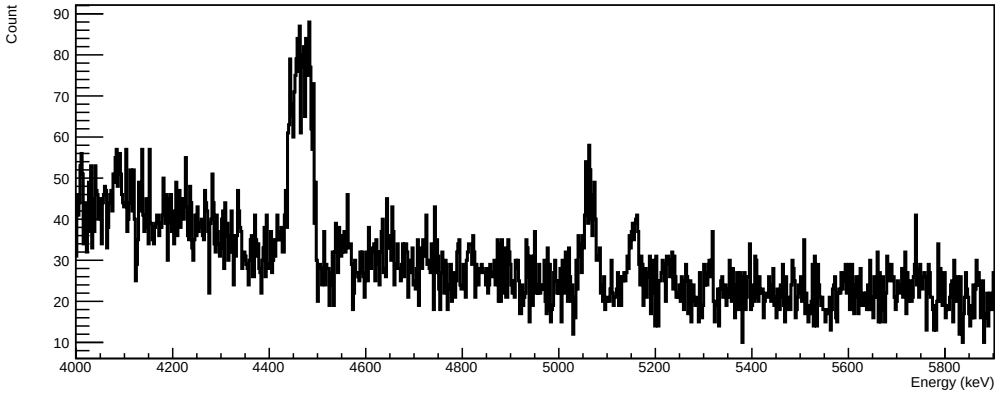

FIGURE A.14: Spectrum of run at $E_{beam} = 2.32$ MeV between $E = 4$ MeV and $E = 6$ MeV.

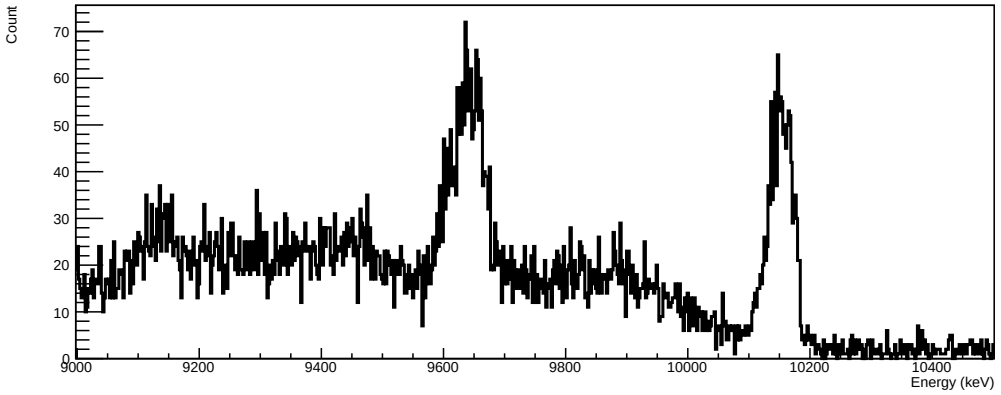

FIGURE A.15: Spectrum of run at $E_{beam} = 2.22$ MeV between $E = 9$ MeV and $E = 10.5$ MeV.

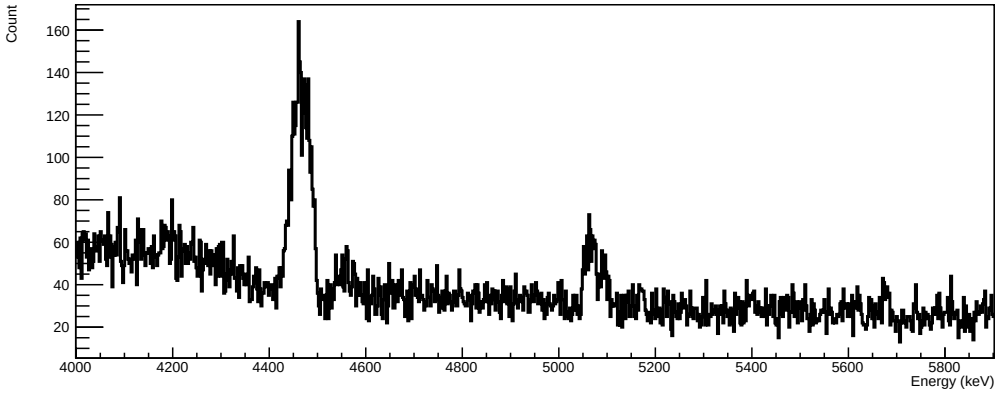

FIGURE A.16: Spectrum of run at $E_{beam} = 2.22$ MeV between $E = 4$ MeV and $E = 6$ MeV.

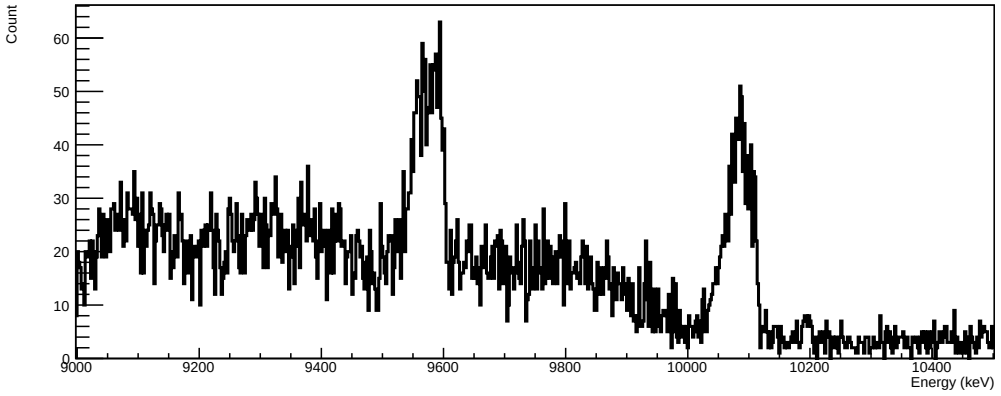

FIGURE A.17: Spectrum of run at $E_{beam} = 2.12$ MeV between $E = 9$ MeV and $E = 10.5$ MeV.

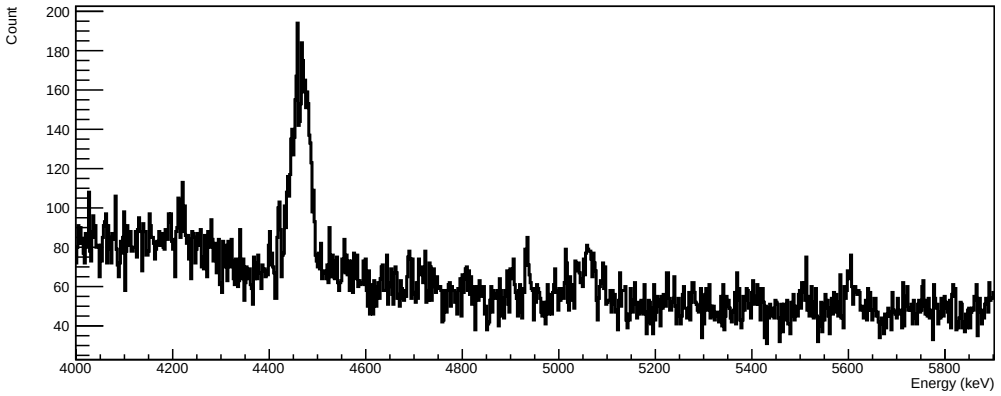

FIGURE A.18: Spectrum of run at $E_{beam} = 2.12$ MeV between $E = 4$ MeV and $E = 6$ MeV.

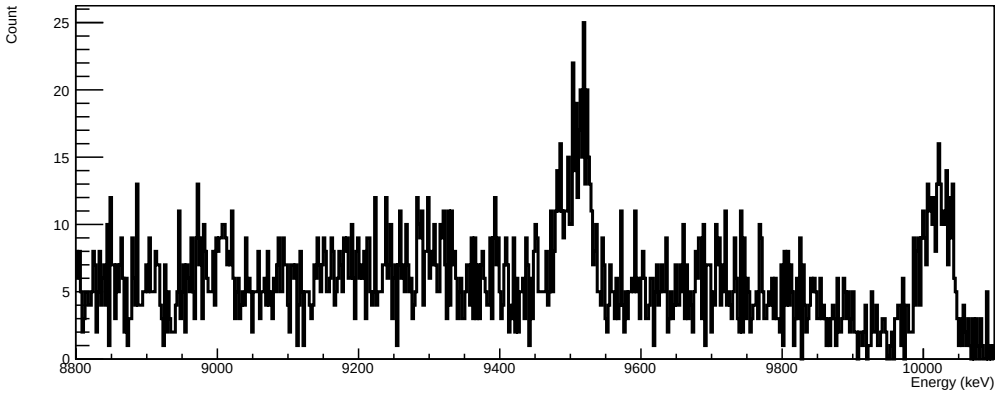

FIGURE A.19: Spectrum of run at $E_{beam} = 2.02$ MeV between $E = 8.8$ MeV and $E = 10.1$ MeV.

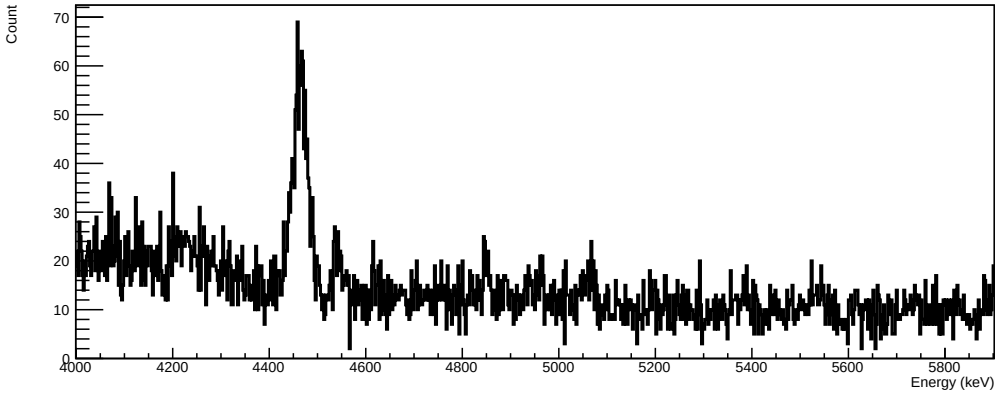

FIGURE A.20: Spectrum of run at $E_{beam} = 2.02$ MeV between $E = 4$ MeV and $E = 6$ MeV.

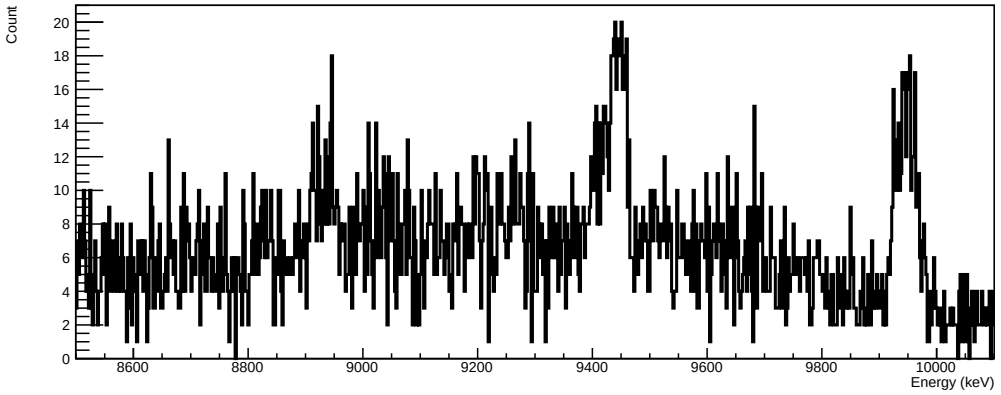

FIGURE A.21: Spectrum of run at $E_{beam} = 1.92$ MeV between $E = 8.8$ MeV and $E = 10.1$ MeV.

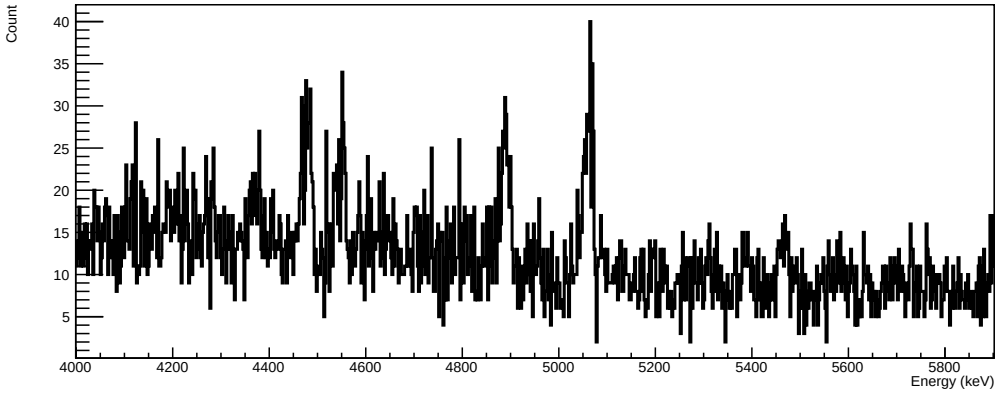

FIGURE A.22: Spectrum of run at $E_{beam} = 1.92$ MeV between $E = 4$ MeV and $E = 6$ MeV.

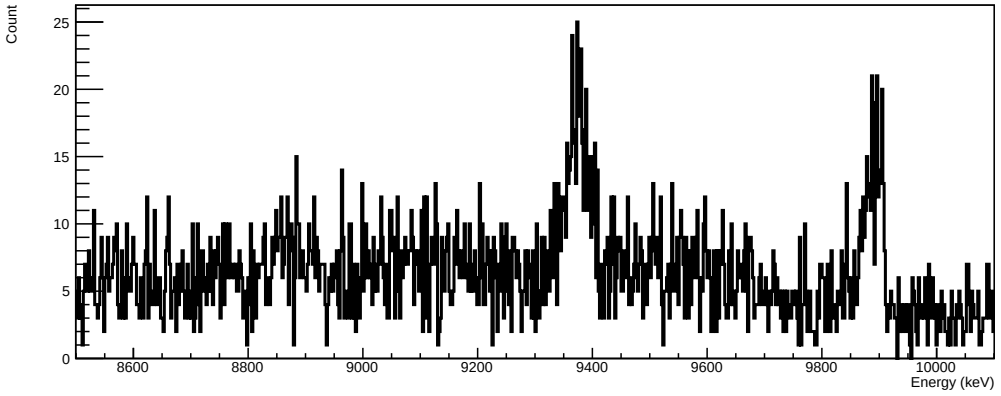

FIGURE A.23: Spectrum of run at $E_{beam} = 1.82$ MeV between $E = 8.5$ MeV and $E = 10.1$ MeV.

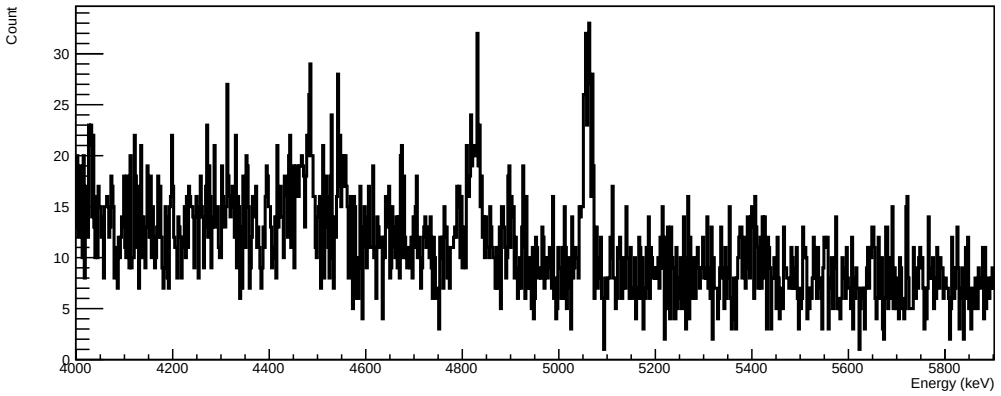

FIGURE A.24: Spectrum of run at $E_{beam} = 1.82$ MeV between $E = 4$ MeV and $E = 6$ MeV.

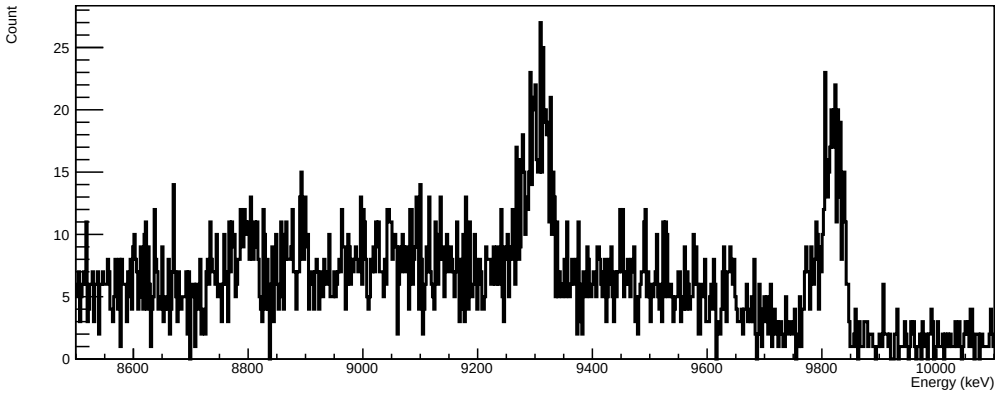

FIGURE A.25: Spectrum of run at $E_{beam} = 1.72$ MeV between $E = 8.5$ MeV and $E = 10.1$ MeV.

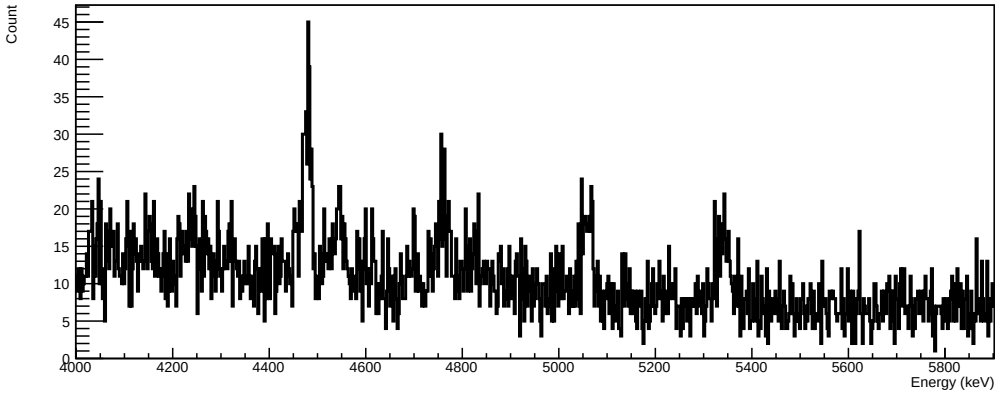

FIGURE A.26: Spectrum of run at $E_{beam} = 1.72$ MeV between $E = 4$ MeV and $E = 6$ MeV.

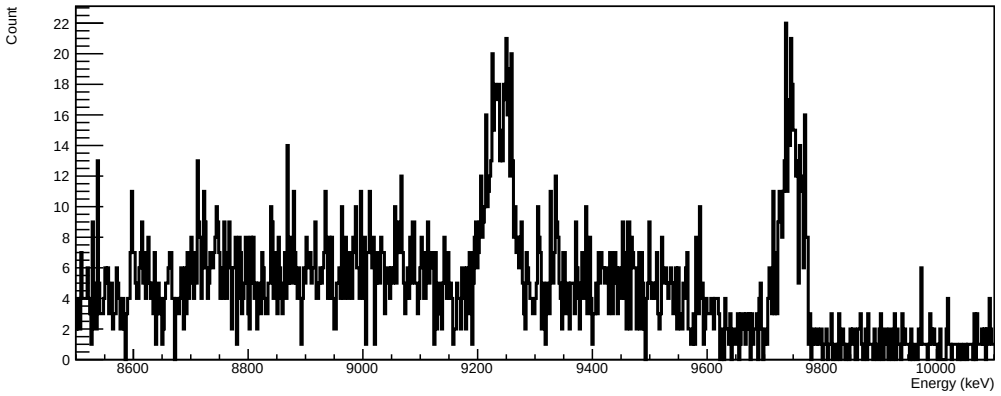

FIGURE A.27: Spectrum of run at $E_{beam} = 1.62$ MeV between $E = 8.5$ MeV and $E = 10.1$ MeV.

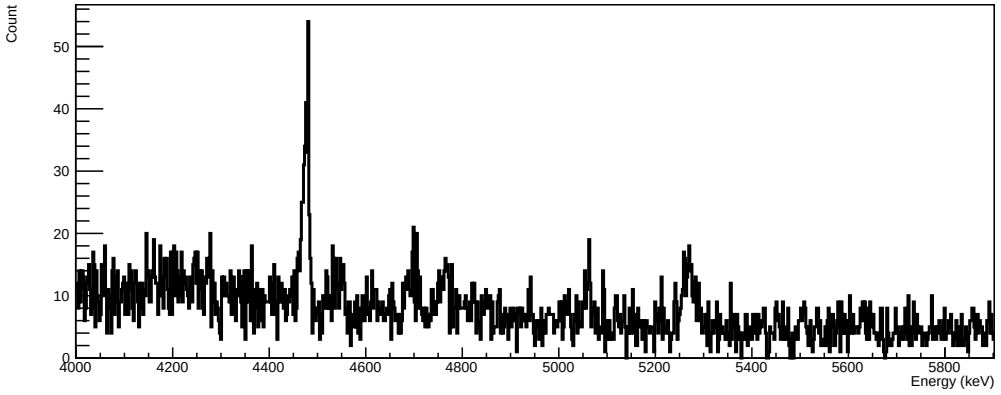

FIGURE A.28: Spectrum of run at $E_{beam} = 1.62$ MeV between $E = 4$ MeV and $E = 6$ MeV.

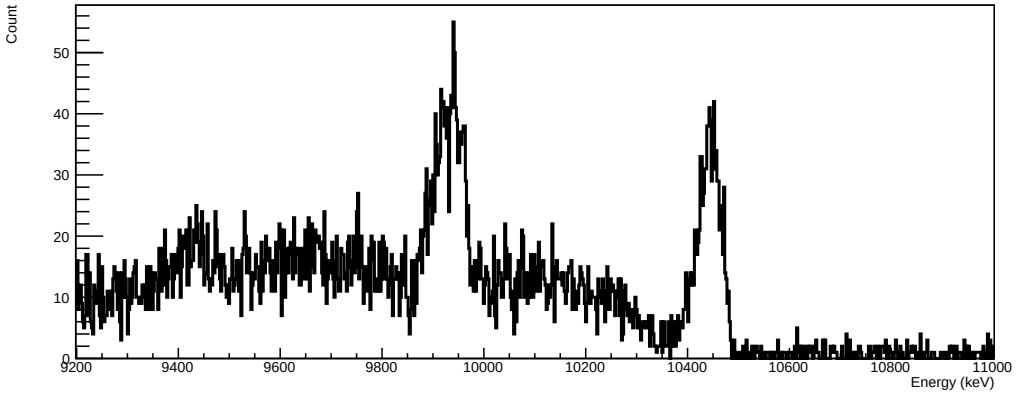

FIGURE A.29: Spectrum of run at $E_{beam} = 2.67$ MeV between $E = 9.2$ MeV and $E = 11$ MeV.

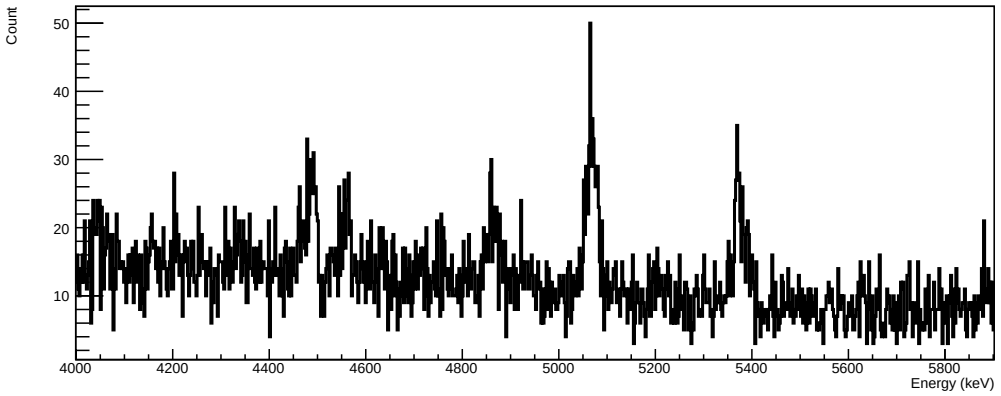

FIGURE A.30: Spectrum of run at $E_{beam} = 2.67$ MeV between $E = 4$ MeV and $E = 6$ MeV.

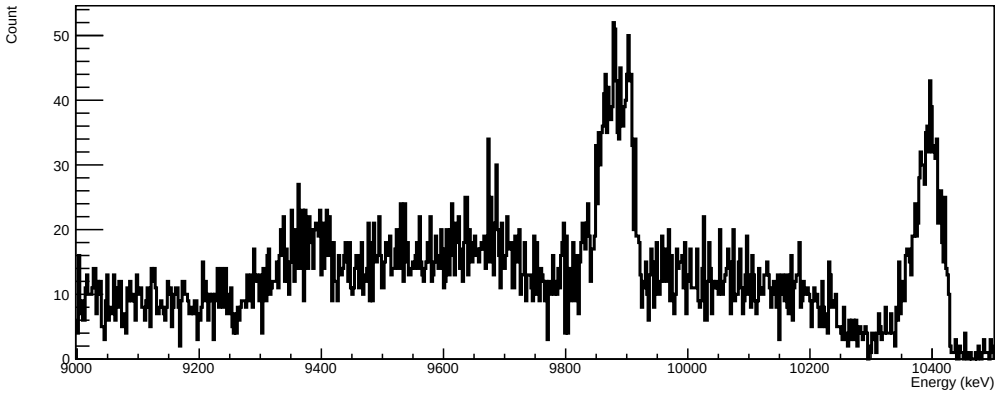

FIGURE A.31: Spectrum of run at $E_{beam} = 2.59$ MeV between $E = 9$ MeV and $E = 10.5$ MeV.

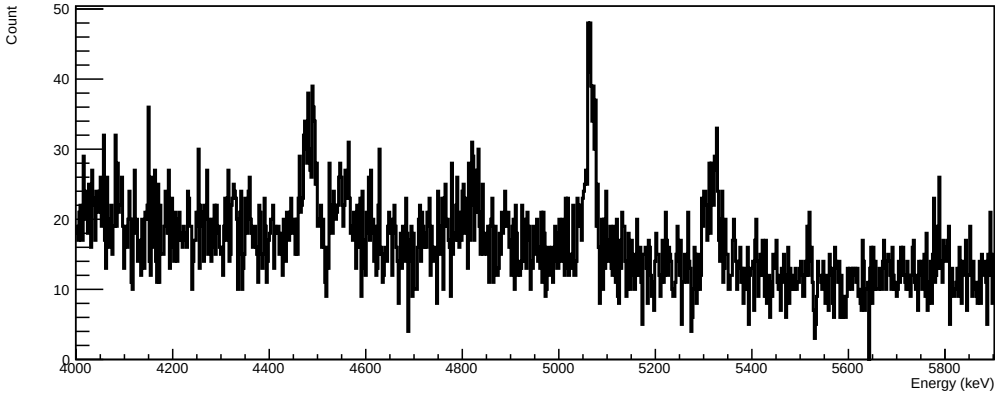

FIGURE A.32: Spectrum of run at $E_{beam} = 2.59$ MeV between $E = 4$ MeV and $E = 6$ MeV.

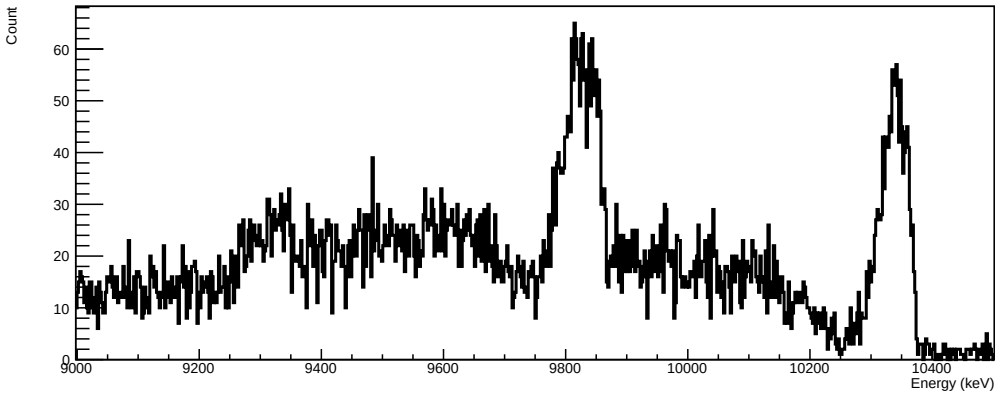

FIGURE A.33: Spectrum of run at $E_{beam} = 2.51$ MeV between $E = 9$ MeV and $E = 10.5$ MeV.

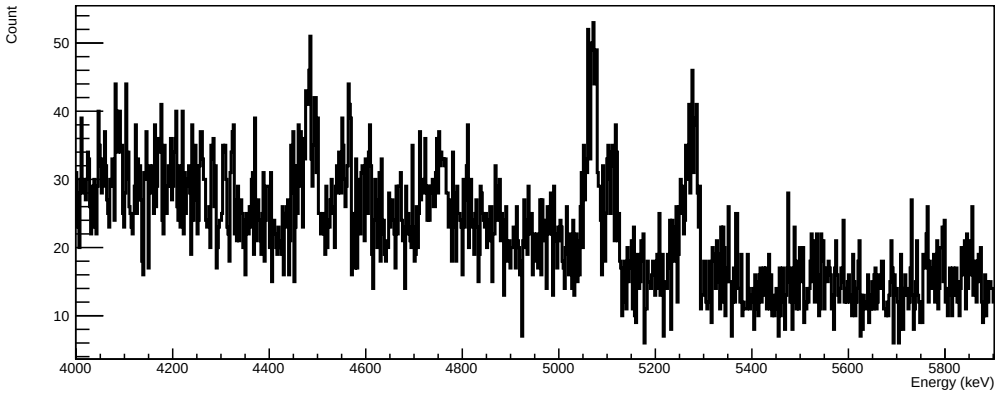

FIGURE A.34: Spectrum of run at $E_{beam} = 2.51$ MeV between $E = 4$ MeV and $E = 6$ MeV.

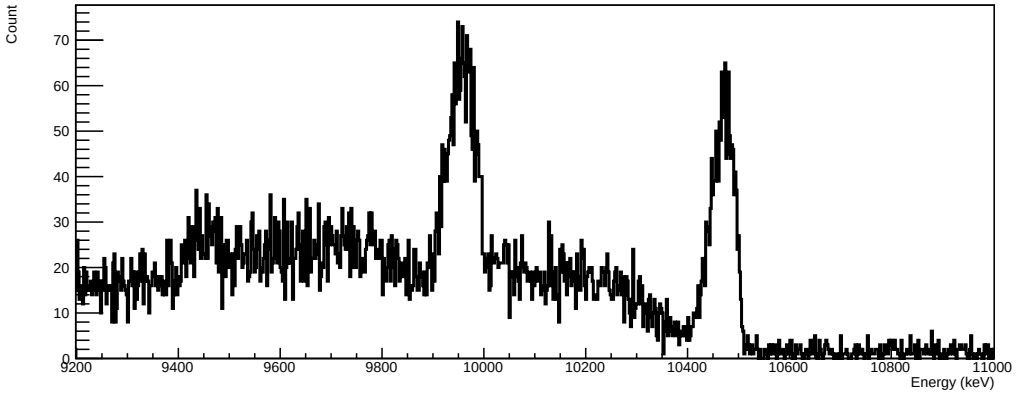

FIGURE A.35: Spectrum of run at $E_{beam} = 2.71$ MeV between $E = 9.2$ MeV and $E = 11$ MeV.

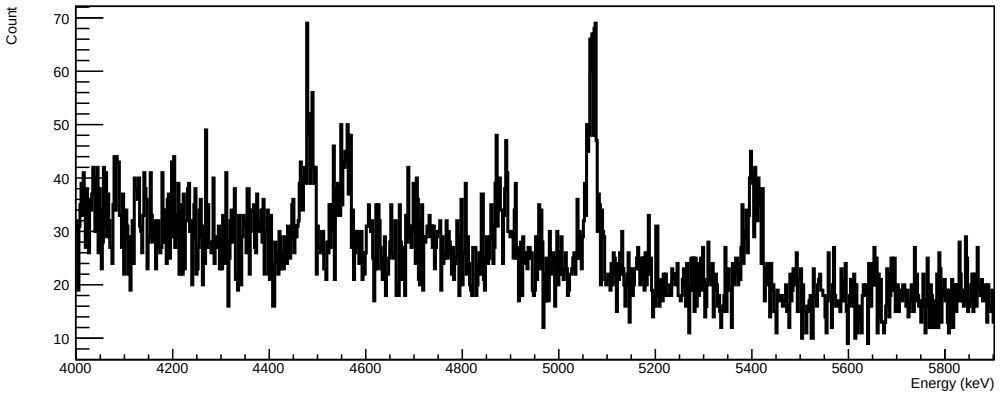

FIGURE A.36: Spectrum of run at $E_{beam} = 2.71$ MeV between $E = 4$ MeV and $E = 6$ MeV.

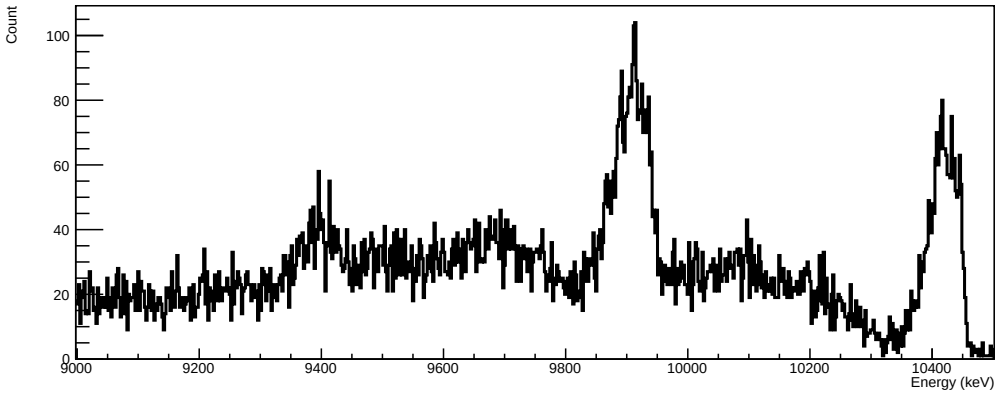

FIGURE A.37: Spectrum of run at $E_{beam} = 2.63$ MeV between $E = 9$ MeV and $E = 10.5$ MeV.

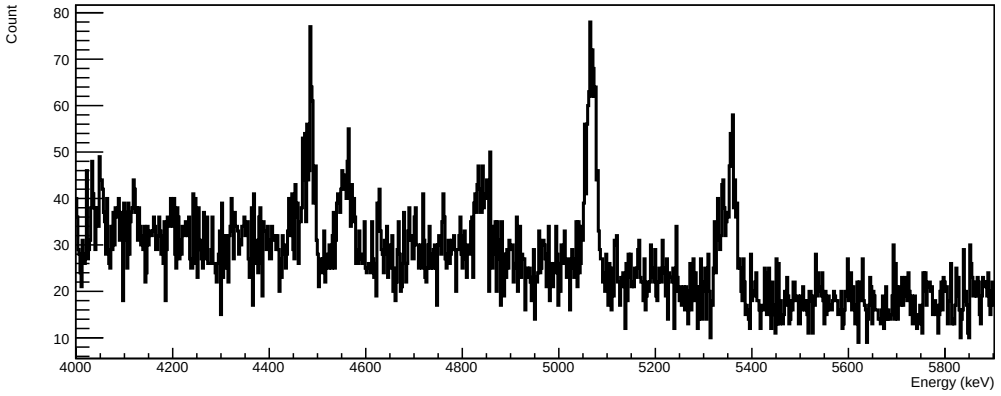

FIGURE A.38: Spectrum of run at $E_{beam} = 2.63$ MeV between $E = 4$ MeV and $E = 6$ MeV.

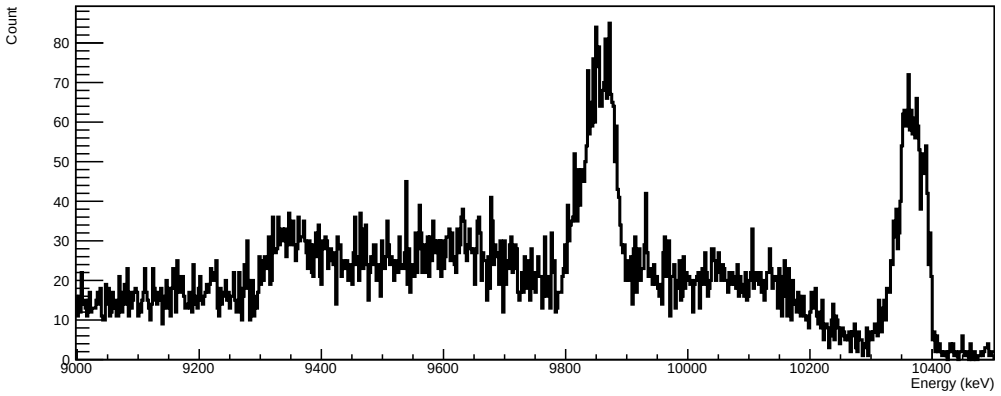

FIGURE A.39: Spectrum of run at $E_{beam} = 2.55$ MeV between $E = 9$ MeV and $E = 10.5$ MeV.

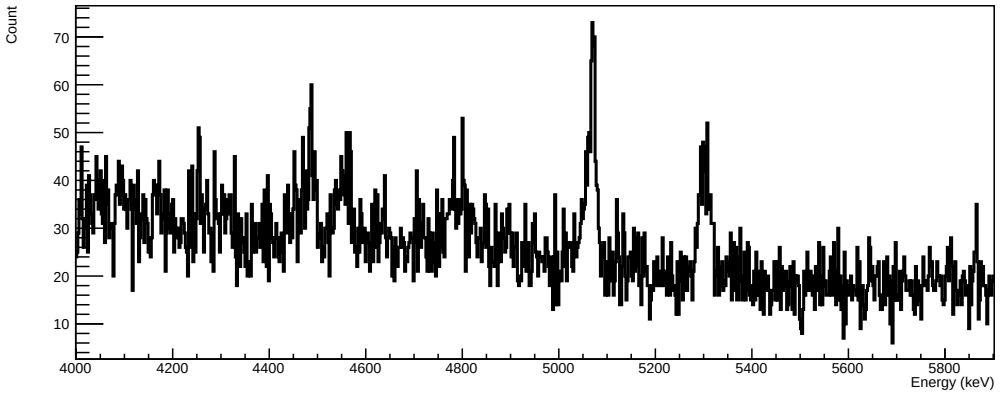

FIGURE A.40: Spectrum of run at $E_{beam} = 2.55$ MeV between $E = 4$ MeV and $E = 6$ MeV.

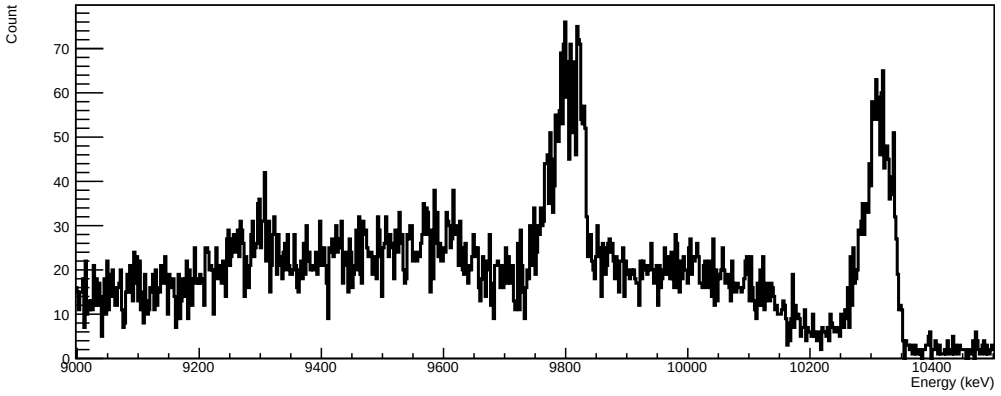

FIGURE A.41: Spectrum of run at $E_{beam} = 2.47$ MeV between $E = 9$ MeV and $E = 10.5$ MeV.

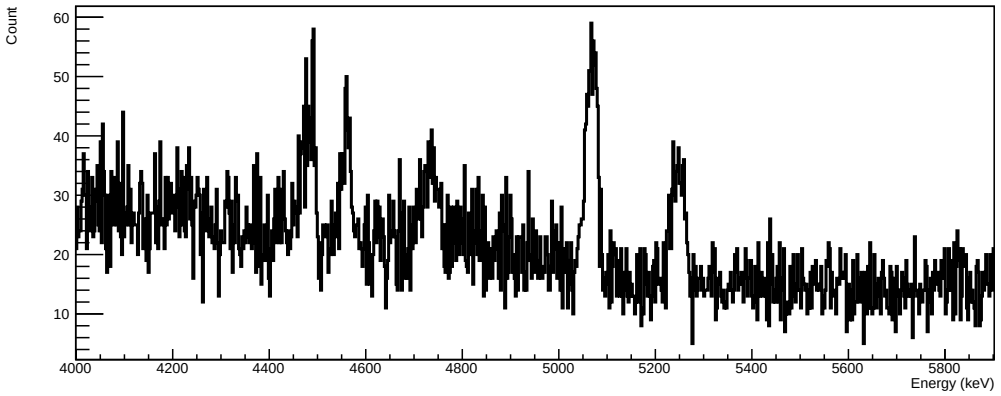

FIGURE A.42: Spectrum of run at $E_{beam} = 2.47$ MeV between $E = 4$ MeV and $E = 6$ MeV.

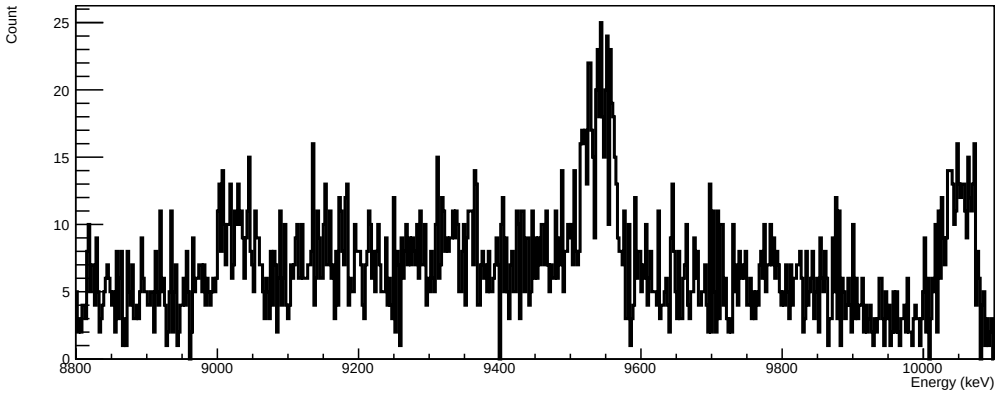

FIGURE A.43: Spectrum of run at $E_{beam} = 2.07$ MeV between $E = 8.8$ MeV and $E = 10.1$ MeV.

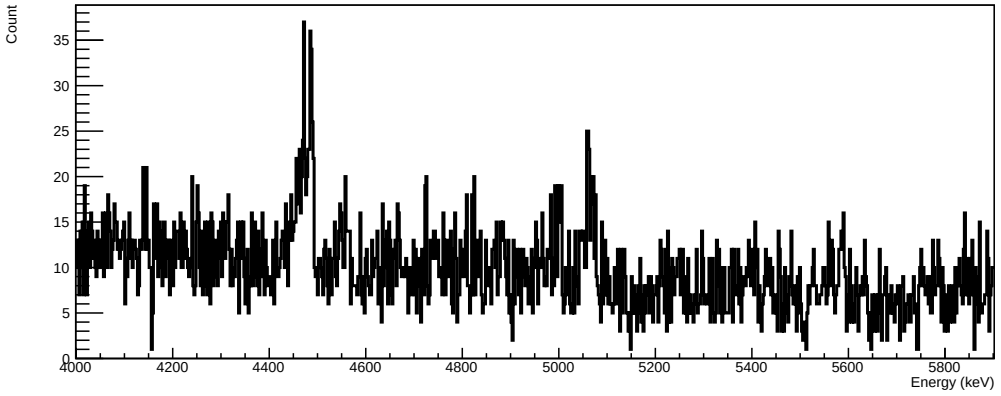

FIGURE A.44: Spectrum of run at $E_{beam} = 2.07$ MeV between $E = 4$ MeV and $E = 6$ MeV.

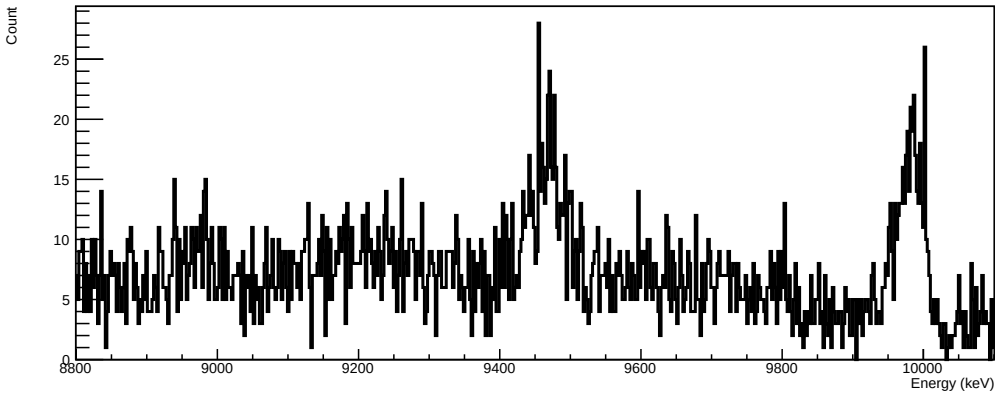

FIGURE A.45: Spectrum of run at $E_{beam} = 1.97$ MeV between $E = 8.8$ MeV and $E = 10.1$ MeV.

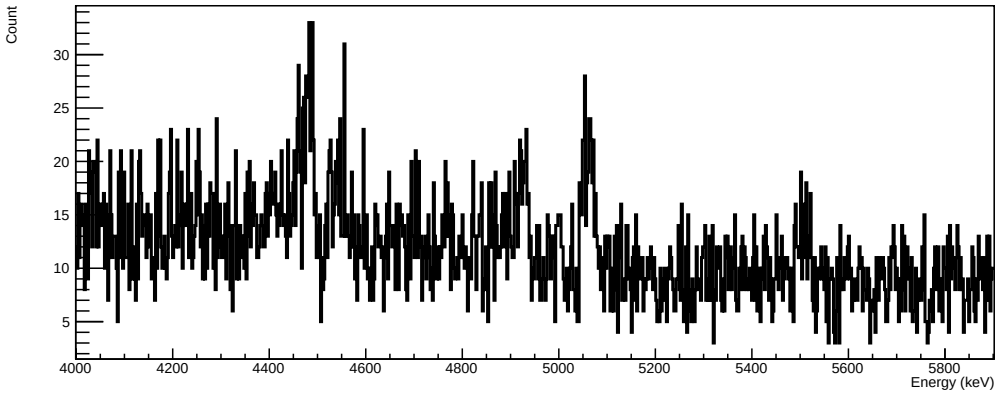

FIGURE A.46: Spectrum of run at $E_{beam} = 1.97$ MeV between $E = 4$ MeV and $E = 6$ MeV.

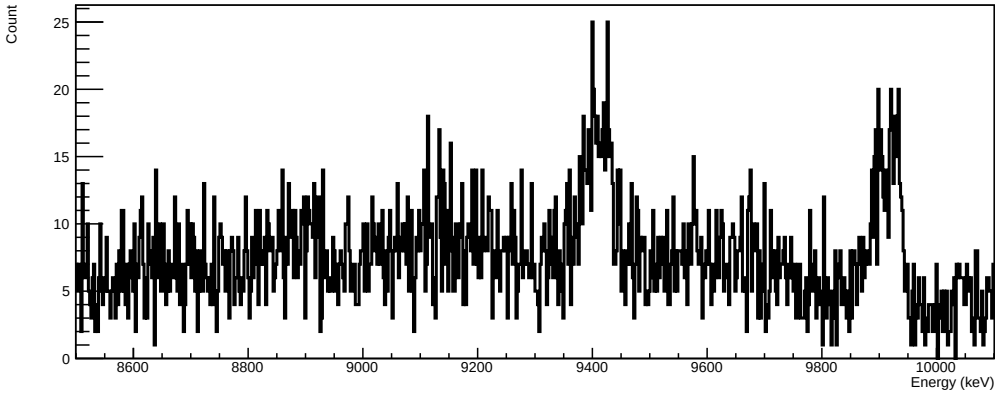

FIGURE A.47: Spectrum of run at $E_{beam} = 1.87$ MeV between $E = 8.5$ MeV and $E = 10.1$ MeV.

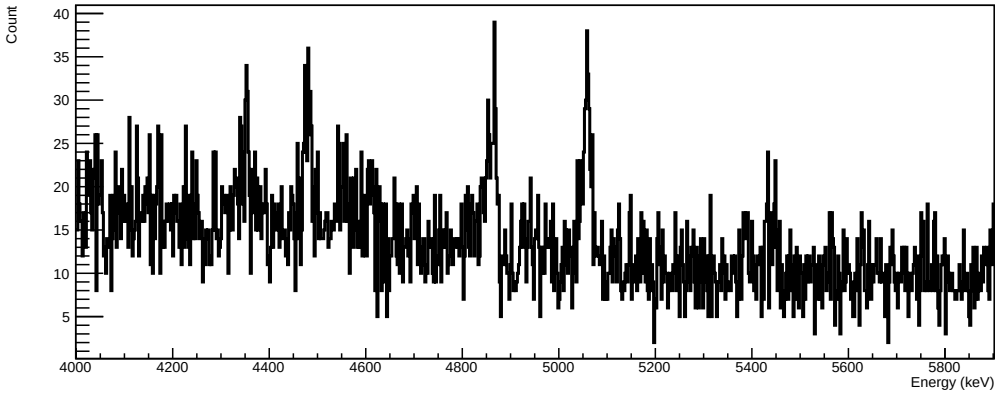

FIGURE A.48: Spectrum of run at $E_{beam} = 1.87$ MeV between $E = 4$ MeV and $E = 6$ MeV.

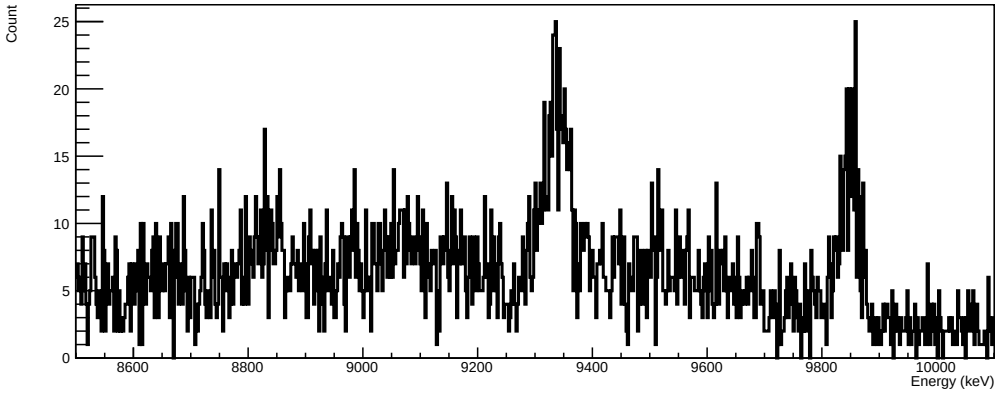

FIGURE A.49: Spectrum of run at $E_{beam} = 1.77$ MeV between $E = 8.5$ MeV and $E = 10.1$ MeV.

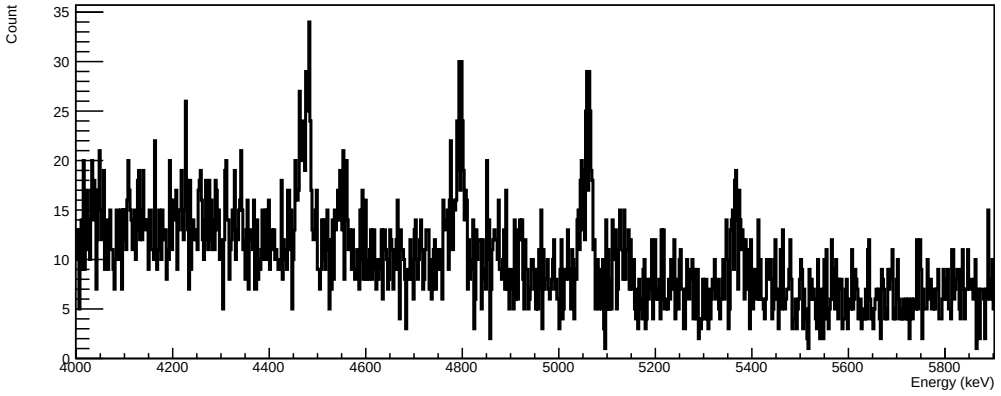

FIGURE A.50: Spectrum of run at $E_{beam} = 1.77$ MeV between $E = 4$ MeV and $E = 6$ MeV

Bibliography

[1] P. Paul, N. G. Puttaswamy, and D. Kohler. Excited states in B^{11} observed in the $Li^7(\alpha\gamma)$ reaction. *Phys. Rev.*, 164:1332–1342, Dec 1967. doi: 10.1103/PhysRev.164.1332. URL https://link.aps.org/doi/10.1103/PhysRev.164.1332.

[2] C. Angulo, M. Arnould, M. Rayet, P. Descouvemont, D. Baye, C. Leclercq-Willain, A. Coc, S. Barhoumi, P. Aguer, C. Rolfs, R. Kunz, J.W. Hammer, A. Mayer, T. Paradellis, S. Kossionides, C. Chronidou, K. Spyrou, S. Degl'Innocenti, G. Fiorentini, B. Ricci, S. Zavatarelli, C. Providencia, H. Wolters, J. Soares, C. Grama, J. Rahighi, A. Shotter, and M. Lamehi Rachti. A compilation of charged-particle induced thermonuclear reaction rates. *Nuclear Physics A*, 656(1):3 – 183, 1999. ISSN 0375-9474. doi: https://doi.org/10.1016/S0375-9474(99)00030-5. URL http://www.sciencedirect.com/science/article/pii/S0375947499000305.

[3] Y. Xu, K. Takahashi, S. Goriely, M. Arnould, M. Ohta, and H. Utsunomiya. Nacre II: an update of the NACRE compilation of charged-particle-induced thermonuclear reaction rates for nuclei with mass number A<16. *Nuclear Physics A*, 918:61 – 169, 2013. ISSN 0375-9474. doi: https://doi.org/10.1016/j.nuclphysa.2013.09.007. URL http://www.sciencedirect.com/science/article/pii/S0375947413007409.

[4] N. P. Heydenburg and G. M. Temmer. Gamma Rays from Li^7, F^{19}, Ne^{22}, and Na^{22} Produced by Alpha-Particle Bombardment of Lithium and Fluorine. *Phys. Rev.*, 94:1252–1257, Jun 1954. doi: 10.1103/PhysRev.94.1252. URL https://link.aps.org/doi/10.1103/PhysRev.94.1252.

[5] G. Hardie, B. W. Filippone, A. J. Elwyn, M. Wiescher, and R. E. Segel. Resonant alpha capture by ^{7}Be and ^{7}Li. *Phys. Rev. C*, 29:1199–1206, Apr 1984. doi: 10.1103/PhysRevC.29.1199. URL https://link.aps.org/doi/10.1103/PhysRevC.29.1199.

[6] S. Woosley and H-T. Janka. The physics of core-collapse supernovae. *Nature Physics*, 1 (172):147–154, December 2005. URL https://www.nature.com/articles/nphys172.

[7] Sean M. Couch. The mechanism(s) of core-collapse supernovae. *Phylosophical Transaction of the Royal Society A*, 375(2015):1–20, September 2017. URL http://rsta.royalsocietypublishing.org/content/375/2105/20160271.

[8] K.G. Balasi, K. Langanke, and G. Martnez-Pinedo. Neutrino - nucleus reactions and their role for supernova dynamics and nucleosynthesis. *Progress in Particle and Nuclear Physics*, 85:33 – 81, 2015. ISSN 0146-6410. doi: https://doi.org/10.1016/j.ppnp.2015.08.001. URL http://www.sciencedirect.com/science/article/pii/S0146641015000654.

[9] Hans-Thomas Janka. *Neutrino Emission from Supernovae*, pages 1575–1604. Springer International Publishing, Cham, 2017. ISBN 978-3-319-21846-5. doi: 10.1007/978-3-319-21846-5_4. URL https://doi.org/10.1007/978-3-319-21846-5_4.

[10] David Vartanyan, Adam Burrows, David Radice, M Aaron Skinner, and Joshua Dolence. A successful 3d core-collapse supernova explosion model. *Monthly Notices of the Royal Astronomical Society*, 482(1):351–369, 2019. doi: 10.1093/mnras/sty2585. URL http://dx.doi.org/10.1093/mnras/sty2585.

[11] Hans A. Bethe and James R. Wilson. Revival of a stalled supernova shock by neutrino heating. *The Astrophysical Journal*, 295:14–23, August 1985. URL http://adsabs.harvard.edu/doi/10.1086/163343.

[12] K. Hirata, T. Kajita, M. Koshiba, M. Nakahata, Y. Oyama, N. Sato, A. Suzuki, M. Takita, Y. Totsuka, T. Kifune, T. Suda, K. Takahashi, T. Tanimori, K. Miyano, M. Yamada, E. W. Beier, L. R. Feldscher, S. B. Kim, A. K. Mann, F. M. Newcomer, R. Van, W. Zhang, and B. G. Cortez. Observation of a neutrino burst from the supernova SN1987A. *Phys. Rev. Lett.*, 58:1490–1493, Apr 1987. doi: 10.1103/PhysRevLett.58.1490. URL https://link.aps.org/doi/10.1103/PhysRevLett.58.1490.

[13] Todd Haines, C.B. Bratton, D. Casper, A. Ciocio, R. Claus, M. Crouch, S.T. Dye, S. Errede, W. Gajewski, M. Goldhaber, T.J. Haines, T.W. Jones, D. Kielczewska, W.R. Kropp, J.G. Learned, J.M. Losecco, J. Matthews, R. Miller, M.S. Mudan, L.R. Price, F. Reines, J. Schultz, S. Seidel, E. Shumard, D. Sinclair, H.W. Sobel, L.R. Sulak, R. Svoboda, G. Thornton, and J.C. Van Der Velde. Neutrinos from SN1987a in the IMB detector. *Nuclear Instruments and Methods in Physics Research Section A: Accelerators, Spectrometers, Detectors and Associated Equipment*, 264(1):28 – 31, 1988. ISSN 0168-9002. doi: https://doi.org/10.1016/0168-9002(88)91097-2. URL http://www.sciencedirect.com/science/article/pii/0168900288910972.

[14] M Th. Keil G. G. Raffelt R. Buras, H-T. Janka and Markus Rampp. Electron neutrino pair annihilation: A new source for muon and tau neutrinos in supernovae. *The Astrophysical Journal*, 587(1):320, 2003. URL http://stacks.iop.org/0004-637X/587/i=1/a=320.

[15] Takashi Yoshida, Toshio Suzuki, Satoshi Chiba, Toshitaka Kajino, Hidekazu Yokomakura, Keiichi Kimura, Akira Takamura, and Dieter H. Hartmann. Neutrino-nucleus reaction cross sections for light element synthesis in supernova explosions. *The Astrophysical Journal*, 686(1):448, 2008. URL http://stacks.iop.org/0004-637X/686/i=1/a=448.

[16] W.C. Haxton K. Langanke G. Martnez-Pinedo Heger, E. Kolbe and S.E. Woosley. Neutrino nucleosynthesis. *Physics Letters B*, 606(3):258 – 264, 2005. ISSN 0370-2693. doi: https://doi.org/10.1016/j.physletb.2004.12.017. URL http://www.sciencedirect.com/science/article/pii/S0370269304016739.

[17] S.E. Woosley D.H. Hartmann, R.D. Hoffman and W.C. Haxton. The ν-process. *The Astrophysical Journal*, 356(1):272–301, June 1990. URL http://adsabs.harvard.edu/abs/1990ApJ...356..272W.

[18] J. J. He, B. L. Jia, S. W. Xu, S. Z. Chen, S. B. Ma, S. Q. Hou, J. Hu, L. Y. Zhang, and X. Q. Yu. Direct measurement of $^{11}\mathrm{B}(p,\gamma)^{12}\mathrm{C}$ astrophysical s factors at low energies. *Phys. Rev. C*, 93:055804, May 2016. doi: 10.1103/PhysRevC.93.055804. URL https://link.aps.org/doi/10.1103/PhysRevC.93.055804.

[19] A. Couture, M. Beard, M. Couder, J. Görres, L. Lamm, P. J. LeBlanc, H. Y. Lee, S. O'Brien, A. Palumbo, E. Stech, E. Strandberg, W. Tan, E. Uberseder, C. Ugalde, M. Wiescher, and R. Azuma. Measurement of the $^{19}\mathrm{F}(p,\gamma)^{20}\mathrm{Ne}$ reaction and interference terms from $E_{\mathrm{c.m.}} = 200-760$ kev. *Phys. Rev. C*, 77:015802, Jan 2008. doi: 10.1103/PhysRevC.77.015802. URL https://link.aps.org/doi/10.1103/PhysRevC.77.015802.

[20] J W Truran. Nucleosynthesis. *Annual Review of Nuclear and Particle Science*, 34(1):53–97, 1984. doi: 10.1146/annurev.ns.34.120184.000413. URL https://doi.org/10.1146/annurev.ns.34.120184.000413.

[21] Martin Lemoine, Elisabeth Vangioni-Flam, and Michel Cass. Galactic cosmic rays and the evolution of light elements. *The Astrophysical Journal*, 499(2):735, 1998. URL http://stacks.iop.org/0004-637X/499/i=2/a=735.

[22] Wataru Fujiya, Peter Hoppe, and Ulrich Ott. Hints for Neutrino-process Boron in Presolar Silicon Carbide Grains from Supernovae. *The Astrophysical Journal Letters*, 730(1):L7, 2011. URL http://stacks.iop.org/2041-8205/730/i=1/a=L7.

[23] Elisabeth Vangioni-Flam and Michel Cassé. Cosmic Lithium-Beryllium-Boron Story. *Astrophysics and Space Science*, 265(1):77–86, Jul 1999. ISSN 1572-946X. doi: 10.1023/A:1002197712862. URL https://doi.org/10.1023/A:1002197712862.

[24] G. Martnez-Pinedo K. Langanke-A. Heger A. Sieverding, L. Huther. Neutrino nucleosynthesis in core-collapse Supernova explosions. *EPJ Web of Conferences*, 109: 06004, 2016. doi: 10.1051/epjconf/201610906004. URL https://doi.org/10.1051/epjconf/201610906004.

[25] Takashi Yoshida, Toshitaka Kajino, Hidekazu Yokomakura, Keiichi Kimura, Akira Takamura, and Dieter H. Hartmann. Supernova Neutrino Nucleosynthesis of Light Elements with Neutrino Oscillations. *Phys. Rev. Lett.*, 96:091101, Mar 2006. doi: 10.1103/PhysRevLett.96.091101. URL https://link.aps.org/doi/10.1103/PhysRevLett.96.091101.

[26] Takashi Yoshida, Mariko Terasawa, Toshitaka Kajino, and Kohsuke Sumiyoshi. Nucleosynthesis of Light Elements and Heavy r-Process Elements through the ν-process in Supernova Explosions. *The Astrophysical Journal*, 600(1):204, 2004. URL http://stacks.iop.org/0004-637X/600/i=1/a=204.

[27] G. J. Mathews, T. Kajino, W. Aoki, W. Fujiya, and J. B. Pitts. Exploring the neutrino mass hierarchy probability with meteoritic supernova material, ν-process nucleosynthesis, and θ_{13} mixing. *Phys. Rev. D*, 85:105023, May 2012. doi: 10.1103/PhysRevD.85.105023. URL https://link.aps.org/doi/10.1103/PhysRevD.85.105023.

[28] Ko Nakamura, Takashi Yoshida, Toshikazu Shigeyama, and Toshitaka Kajino. Boron Synthesis in Type IC Supernovae. *The Astrophysical Journal Letters*, 718(2):L137, 2010. URL http://stacks.iop.org/2041-8205/718/i=2/a=L137.

[29] A. Sieverding, G. Martnez-Pinedo, L. Huther, K. Langanke, and A. Heger. The ν -Process in the Light of an Improved Understanding of Supernova Neutrino Spectra. *The Astrophysical Journal*, 865(2):143, 2018. URL http://stacks.iop.org/0004-637X/865/i=2/a=143.

[30] Sam M. Austin, Alexander Heger, and Clarisse Tur. ^{11}B and constraints on neutrino oscillations and spectra from neutrino nucleosynthesis. *Phys. Rev. Lett.*, 106:152501,

Apr 2011. doi: 10.1103/PhysRevLett.106.152501. URL https://link.aps.org/doi/10.1103/PhysRevLett.106.152501.

[31] X. Qian and P. Vogel. Neutrino mass hierarchy. *Progress in Particle and Nuclear Physics*, 83:1 – 30, 2015. ISSN 0146-6410. doi: https://doi.org/10.1016/j.ppnp.2015.05.002. URL http://www.sciencedirect.com/science/article/pii/S0146641015000307.

[32] A. Caciolli for the LUNA collaboration. Nuclear Astrophysics in underground laboratories: the LUNA experiment. *EPJ Web of Conferences*, 163, 2017. doi: https://doi.org/10.1051/epjconf/201716300009. URL https://www.epj-conferences.org/articles/epjconf/abs/2017/32/epjconf_fusion2017_00009/epjconf_fusion2017_00009.html.

[33] D. Robertson, M. Couder, U. Greife, F. Strieder, and M. Wiescher. Underground nuclear astrophysics studies with CASPAR. *EPJ Web of Conferences*, 109, 2016. doi: https://doi.org/10.1051/epjconf/201610909002. URL https://www.epj-conferences.org/articles/epjconf/abs/2016/04/epjconf_omeg2016_09002/epjconf_omeg2016_09002.html.

[34] Carlo Broggini, Daniel Bemmerer, Alessandra Guglielmetti, and Roberto Menegazzo. LUNA: Nuclear Astrophysics Deep Underground. *Annual Review of Nuclear and Particle Science*, 60(1):53–73, 2010. doi: 10.1146/annurev.nucl.012809.104526. URL https://doi.org/10.1146/annurev.nucl.012809.104526.

[35] Shinya Wanajo, Hans-Thomas Janka, and Shigeru Kubono. Uncertainties in the νp-process: Supernova dynamics versus nuclear physics. *The Astrophysical Journal*, 729 (1):46, 2011. URL http://stacks.iop.org/0004-637X/729/i=1/a=46.

[36] M. A. Zhusupov, E. T. Ibraeva, R. S. Kabatayeva, and P. M. Krassovitskiy. Interaction of α Particles with ^6Li and ^7Li Nuclei at Low Energies. *Bulletin of the Russian Academy of Sciences: Physics*, 74(6):885–889, Jun 2010. ISSN 1934-9432. doi: 10.3103/S1062873810060328. URL https://doi.org/10.3103/S1062873810060328.

[37] F.E. Cecil, S.J. Zweben, and S.S. Medley. A method for determining fast alpha particle confinement in tokamak plasmas using resonant nuclear reactions. *Nuclear Instruments and Methods in Physics Research Section A: Accelerators, Spectrometers, Detectors and Associated Equipment*, 245(2):547 – 552, 1986. ISSN 0168-9002. doi:

https://doi.org/10.1016/0168-9002(86)91296-9. URL http://www.sciencedirect.com/science/article/pii/0168900286912969.

[38] F. Spite and M. Spite. Abundance of lithium in unevolved halo stars and old disk star : Interpretation and consequences. *Astron. Astrophys.*, 115:357–366, 1982. URL http://adsabs.harvard.edu/abs/1982A&A...115..357S.

[39] Brian D. Fields and Keith A. Olive. Big bang nucleosynthesis. *Nuclear Physics A*, 777:208 – 225, 2006. ISSN 0375-9474. doi: https://doi.org/10.1016/j.nuclphysa.2004.10.033. URL http://www.sciencedirect.com/science/article/pii/S0375947404011479. Special Isseu on Nuclear Astrophysics.

[40] A Coc. Primordial Nucleosynthesis. *Journal of Physics: Conference Series*, 665(1): 012001, 2016. URL http://stacks.iop.org/1742-6596/665/i=1/a=012001.

[41] Richard H. Cyburt, Brian D. Fields, Keith A. Olive, and Tsung-Han Yeh. Big bang nucleosynthesis: Present status. *Rev. Mod. Phys.*, 88:015004, Feb 2016. doi: 10.1103/RevModPhys.88.015004. URL https://link.aps.org/doi/10.1103/RevModPhys.88.015004.

[42] J.H. Kelley, E. Kwan, J.E. Purcell, C.G. Sheu, and H.R. Weller. Energy levels of light nuclei A=11. *Nuclear Physics A*, 880:88 – 195, 2012. ISSN 0375-9474. doi: https://doi.org/10.1016/j.nuclphysa.2012.01.010. URL http://www.sciencedirect.com/science/article/pii/S0375947412000413.

[43] F. L. H. Wolfs, C. A. White, D. C. Bryan, C. G. Freeman, D. M. Herrick, K. L. Kurz, D. H. Mathews, P. A. A. Perera, and M. T. Zanni. Breakup of 87 MeV ^{11}B. *Phys. Rev. C*, 49:2538–2548, May 1994. doi: 10.1103/PhysRevC.49.2538. URL https://link.aps.org/doi/10.1103/PhysRevC.49.2538.

[44] D. M. Van Patter, W. W. Buechner, and A. Sperduto. Energy levels of b^{11} from the $B^{10}(d,p)B^{11*}$ reaction. *Phys. Rev.*, 82:248–257, Apr 1951. doi: 10.1103/PhysRev.82.248. URL https://link.aps.org/doi/10.1103/PhysRev.82.248.

[45] Mortimer M. Elkind. Excited states of B^{11} and B^{12} from the reactions $B^{10}(d,p)B^{11}$ and $B^{11}(d,p)B^{12}$. *Phys. Rev.*, 92:127–133, Oct 1953. doi: 10.1103/PhysRev.92.127. URL https://link.aps.org/doi/10.1103/PhysRev.92.127.

[46] C. P. Browne and F. H. O'Donnell. Accurate Excitation Energies of B^{11} States Below 7 MeV. *Phys. Rev.*, 149:767–771, Sep 1966. doi: 10.1103/PhysRev.149.767. URL https://link.aps.org/doi/10.1103/PhysRev.149.767.

[47] C. P. Browne and H. Stocker. Additional Accurate Excitation Energies of ^{11}B. *Phys. Rev. C*, 4:1481–1482, Oct 1971. doi: 10.1103/PhysRevC.4.1481. URL https://link.aps.org/doi/10.1103/PhysRevC.4.1481.

[48] G. Van Der Steenhoven, H.P. Blok, E. Jans, L. Lapiks, E.N.M. Quint, and P.K.A. De Witt Huberts. Weak transitions in the quasi-elastic reaction $^{12}C(e, ep)^{11}B$. *Nuclear Physics A*, 484(3):445 – 475, 1988. ISSN 0375-9474. doi: https://doi.org/10.1016/0375-9474(88)90304-1. URL http://www.sciencedirect.com/science/article/pii/0375947488903041.

[49] B. Zwiegliński, W. Benenson, G.M. Crawley, S. Gals, and D. Weber. Study of ^{11}B at high excitations with the $^{9}Be(^{3}He, p)^{11}B$ and $^{9}Be(\alpha, d)^{11}B$ reactions. *Nuclear Physics A*, 389(2):301 – 323, 1982. ISSN 0375-9474. doi: https://doi.org/10.1016/0375-9474(82)90521-8. URL http://www.sciencedirect.com/science/article/pii/0375947482905218.

[50] S. Hinds and R. Middleton. An investigation of the protons, deuterons and tritons from the bombardment of ^{9}Be with 5.7 MeV ^{3}He. *Proceedings of the Physical Society*, 74(2):196, 1959. URL http://stacks.iop.org/0370-1328/74/i=2/a=307.

[51] E. Kashy, W. Benenson, and J. A. Nolen. $A = 9$ isospin quartet. *Phys. Rev. C*, 9:2102–2105, Jun 1974. doi: 10.1103/PhysRevC.9.2102. URL https://link.aps.org/doi/10.1103/PhysRevC.9.2102.

[52] D. J. Millener, D. E. Alburger, E. K. Warburton, and D. H. Wilkinson. Decay scheme of ^{11}Be. *Phys. Rev. C*, 26:1167–1185, Sep 1982. doi: 10.1103/PhysRevC.26.1167. URL https://link.aps.org/doi/10.1103/PhysRevC.26.1167.

[53] Meng Wang, G. Audi, F.G. Kondev, W.J. Huang, S. Naimi, and Xing Xu. The AME2016 atomic mass evaluation (II). Tables, graphs and references. *Chinese Physics C*, 41(3):030003, 2017. URL http://stacks.iop.org/1674-1137/41/i=3/a=030003.

[54] L. L. Green, G. A. Stephens, and J. C. Willmott. The ^{7}Li$(\alpha, \gamma)^{11}$B reaction. *Proceedings of the Physical Society*, 79(5):1017, 1962. URL http://stacks.iop.org/0370-1328/79/i=5/a=314.

[55] R.Y. Cusson. Levels in 11b from ^{7}Li$(\alpha, \alpha)^{7}$Li and ^{7}Li$(\alpha, \alpha')^{7}$Li$^{*}(0.48)$. *Nuclear Physics*, 86(3):481 – 508, 1966. ISSN 0029-5582. doi: https://doi.org/10.1016/0029-5582(66)90492-5. URL http://www.sciencedirect.com/science/article/pii/0029558266904925.

[56] G.A. Jones, C.M.P. Johnson, and D. H. Wilkinson. The reaction ^{7}Li$(\alpha,\gamma)^{11}$B. *Philosophical magazine*, 4:796–814, Jan 1959. doi: doi.org/10.1080/14786435908238236. URL http://www.tandfonline.com/doi/abs/10.1080/14786435908238236.

[57] W. E. Bennett, Paul A. Roys, and B. J. Toppel. Simple Capture of Alpha-Particles. *Phys. Rev.*, 82:20–22, Apr 1951. doi: 10.1103/PhysRev.82.20. URL https://link.aps.org/doi/10.1103/PhysRev.82.20.

[58] Gy. Gyürky, Zs. Fülöp, E. Somorjai, G. Kiss, and C. Rolfs. Absolute resonance strengths in the $^{6,7}Li(\alpha,\gamma)^{10,11}B$ reactions. *The European Physical Journal A - Hadrons and Nuclei*, 21(2):355–358, Aug 2004. ISSN 1434-601X. doi: 10.1140/epja/i2003-10212-2. URL https://doi.org/10.1140/epja/i2003-10212-2.

[59] H. Yamaguchi, T. Hashimoto, S. Hayakawa, D. N. Binh, D. Kahl, S. Kubono, Y. Wakabayashi, T. Kawabata, and T. Teranishi. α resonance structure in ^{11}B studied via resonant scattering of $^{7}Li + \alpha$. *Phys. Rev. C*, 83:034306, Mar 2011. doi: 10.1103/PhysRevC.83.034306. URL https://link.aps.org/doi/10.1103/PhysRevC.83.034306.

[60] Hans Bichsel and T. W. Bonner. Reactions $Li^{7}(\alpha,n)B^{10}, Li^{7}(\alpha,\alpha')Li^{7*}$, and $B^{10}(n,\alpha)Li^{7}$. *Phys. Rev.*, 108:1025–1027, Nov 1957. doi: 10.1103/PhysRev.108.1025. URL https://link.aps.org/doi/10.1103/PhysRev.108.1025.

[61] C. W. Li and R. Sherr. Inelastic Scattering of Alpha Particles by Lithium. *Phys. Rev.*, 96:389–393, Oct 1954. doi: 10.1103/PhysRev.96.389. URL https://link.aps.org/doi/10.1103/PhysRev.96.389.

[62] P. Descouvemont. The $^{7}Be(\alpha,\gamma)^{11}C$ and$^{7}Li(\alpha,\gamma)^{11}B$ reactions in a microscopic three-cluster model. *Nuclear Physics A*, 584(3):532 – 546, 1995. ISSN 0375-9474. doi: https://doi.org/10.1016/0375-9474(94)00784-K. URL http://www.sciencedirect.com/science/article/pii/037594749400784K.

[63] A. A. Valverde, M. Brodeur, T. Ahn, J. Allen, D. W. Bardayan, F. D. Becchetti, D. Blankstein, G. Brown, D. P. Burdette, B. Frentz, G. Gilardy, M. R. Hall, S. King, J. J. Kolata, J. Long, K. T. Macon, A. Nelson, P. D. O'Malley, M. Skulski, S. Y. Strauss, and B. Vande Kolk. Precision half-life measurement of ^{11}C: The most precise mirror transition $\mathcal{F}t$ value. *Phys. Rev. C*, 97:035503, Mar

2018. doi: 10.1103/PhysRevC.97.035503. URL https://link.aps.org/doi/10.1103/PhysRevC.97.035503.

[64] Thomas Griegel, Heinz W. Drotleff, J. Wolfgang Hammer, Heinrich Knee, and Knut Petkau. Physical properties of a heavy ion beam excited supersonic jet gas target. *Journal of Applied Physics*, 69(1):19–22, 1991. doi: 10.1063/1.347743. URL https://doi.org/10.1063/1.347743.

[65] S. Lyons, J. Görres, R. J. deBoer, E. Stech, Y. Chen, G. Gilardy, Q. Liu, A. M. Long, M. Moran, D. Robertson, C. Seymour, B. Vande Kolk, M. Wiescher, and A. Best. Determination of ^{20}Ne$(p,\gamma)^{21}$Na cross sections from $E_p = 500 - 2000$ keV. *Phys. Rev. C*, 97:065802, Jun 2018. doi: 10.1103/PhysRevC.97.065802. URL https://link.aps.org/doi/10.1103/PhysRevC.97.065802.

[66] Z. Meisel, M.T. Moran, G. Gilardy, J. Schmitt, C. Seymour, and M. Couder. Energy acceptance of the St. George recoil separator. *Nuclear Instruments and Methods in Physics Research Section A: Accelerators, Spectrometers, Detectors and Associated Equipment*, 850:48 – 53, 2017. ISSN 0168-9002. doi: https://doi.org/10.1016/j.nima.2017.01.035. URL http://www.sciencedirect.com/science/article/pii/S0168900217300359.

[67] A. Pochelon. Electron Cyclotron Resonance Ion Sources and ECR Plasmas. *Plasma Physics and Controlled Fusion*, 39(6), 1997. URL http://stacks.iop.org/0741-3335/39/i=6/a=008.

[68] National Electronics Corps. *Pelletron charging system*, 2018. URL http://www.pelletron.com/products/pelletron-charging-chains/. Last accessed October 2016.

[69] J. H. Hubbell and S. M. Seltzer. X-ray mass attenuation coefficient, 2004. URL https://physics.nist.gov/PhysRefData/XrayMassCoef/tab3.html.

[70] Fast comp tech. *MPA-NT Multiparameter System Software*, 2018. https://www.fastcomtec.com/fwww/datashee/mpa/mpant.pdf.

[71] J.H. Evans. Formation of blisters in molybdenum bombarded with helium. *Nature*, 256:299–300, July 1975. URL https://www.nature.com/articles/256299a0.

[72] Joachim Gorres, 2017. Private communication.

[73] James Ziegler. *SRIM - The Stopping and Range of Ions in Matter*, 2010. http://www.srim.org/.

[74] P.M. Endt, C. Alderliesten, F. Zijderhand, A.A. Wolters, and A.G.M. Van Hees. Spectroscopic information on ^{24}Mg and ^{28}Si from proton capture. *Nuclear Physics A*, 510(2):209 – 243, 1990. ISSN 0375-9474. doi: https://doi.org/10.1016/0375-9474(90)90237-G. URL http://www.sciencedirect.com/science/article/pii/037594749090237G.

[75] I. Radulescu, A.M. Blebea-Apostu, R.M. Margineanu, and N. Mocanu. Background radiation reduction for a high-resolution gamma-ray spectrometer used for environmental radioactivity measurements. *Nuclear Instruments and Methods in Physics Research Section A: Accelerators, Spectrometers, Detectors and Associated Equipment*, 715:112 – 118, 2013. ISSN 0168-9002. doi: https://doi.org/10.1016/j.nima.2013.03.024. URL http://www.sciencedirect.com/science/article/pii/S0168900213003112.

[76] D. B. Gin, V. G. Kiptily, A. A. Pasternak, I. N. Chugunov, A. E. Shevelev, G. Gorini, M. Tardocchi, and M. Nocente. Doppler shapes of the γ line in the $^{9}Be(\alpha, n\gamma)^{12}C$ reaction in plasma at temperatures $T_\alpha < 0.6$ mev. *Bulletin of the Russian Academy of Sciences: Physics*, 75(7):931, Aug 2011. ISSN 1934-9432. doi: 10.3103/S1062873811070161. URL https://doi.org/10.3103/S1062873811070161.

[77] D. B. Gin, A. A. Pasternak, I. N. Chugunov, and A. E. Shevelev. Investigation of the n-γ angular correlation in the $^{9}Be(\alpha, n\gamma)^{12}C$ reaction by analysis of the 4.44-mev γ-line shape. *Bulletin of the Russian Academy of Sciences: Physics*, 73(6):727–730, Jun 2009. ISSN 1934-9432. doi: 10.3103/S1062873809060070. URL https://doi.org/10.3103/S1062873809060070.

[78] R. E. Azuma, E. Uberseder, E. C. Simpson, C. R. Brune, H. Costantini, R. J. de Boer, J. Görres, M. Heil, P. J. LeBlanc, C. Ugalde, and M. Wiescher. Azure: An r-matrix code for nuclear astrophysics. *Phys. Rev. C*, 81:045805, Apr 2010. doi: 10.1103/PhysRevC.81.045805. URL https://link.aps.org/doi/10.1103/PhysRevC.81.045805.

[79] A. M. Lane and R. G. Thomas. R-matrix Theory of Nuclear Reactions. *Rev. Mod. Phys.*, 30:257–353, Apr 1958. doi: 10.1103/RevModPhys.30.257. URL https://link.aps.org/doi/10.1103/RevModPhys.30.257.

[80] F. James. MINUIT: Function Minimization and Error Analysis Reference Manual. 1998. URL http://cds.cern.ch/record/2296388. CERN Program Library Long Writeups.

[81] E. P. Wigner and L. Eisenbud. Higher angular momenta and long range interaction in resonance reactions. *Phys. Rev.*, 72:29–41, Jul 1947. doi: 10.1103/PhysRev.72.29. URL https://link.aps.org/doi/10.1103/PhysRev.72.29.

[82] Carl B. Dover, C. Mahaux, and Hans A. Weidenmller. The single-particle limit for partial widths. *Nuclear Physics A*, 139(3):593 – 604, 1969. ISSN 0375-9474. doi: https://doi.org/10.1016/0375-9474(69)90281-4. URL http://www.sciencedirect.com/science/article/pii/0375947469902814.

[83] L.Brito J.C.Soares C.Providência, H.Wolters, 2018. Internal report of the NACRE collaboration, Private communication from Alain Coc.